Doctoral Dissertation
Doctoral Program in Electronic, Electric and Communication Engineering (34.th cycle)

Power scaling of high power laser systems

Development of multiplexing schemes of high power laser sources

Alessandro Mirigaldi

* * * * * *

Supervisor
Prof. Guido Perrone

Doctoral Examination Committee:
Prof. Annamaria Cucinotta, Referee, Università di Parma
Prof. Alessia Allevi, Referee, Università degli studi dell'Insubria
Prof. E.F., University of . . .
Prof. G.H., University of . . .
Prof. I.J., University of . . .

Politecnico di Torino
November, 2021

I hereby declare that the contents and organisation of this dissertation constitute my own original work and does not compromise in any way the rights of third parties, including those relating to the security of personal data.

. . . .
Alessandro Mirigaldi
Turin, November, 2021

Summary

The increasing consciousness on the ongoing climate change is pushing the demand for more efficient, energy saving, and CO_2 emission cutting technologies. Photonics is known to be one of the key technologies that can help not only to make whole productive sector cleaner and more efficient, but also to enable its entry into the circular economy. In particular, the high power laser technology has the potential to revolutionize, among the others, the materials processing and the entire manufacturing industry. However, in doing so, an increasing request for a combination of higher efficiency, beam quality, and brightness will have to be satisfied.

In this monograph several techniques and approaches to scale up the output power of laser systems are analyzed.

In more detail, in Ch. 2 the coherent multiplexing approach is numerically analyzed exploiting a new "ad hoc" introduced wave optic framework.

In Ch. 4, the spectral multiplexing approach is discussed. This represents an alternative, less complicated, thus less expensive, multiplexing technique, suitable for applications in which the spectral purity of the beam is not crucial. Spectral multiplexing is particularly interesting for the power scaling of high-power laser modules made by the combination of a number of single chips in a common package – the so-called "multiemitters". In this chapter, first, the spectral multiplexing is theoretically evaluated through a stochastic model. Then, using the developed framework, the design and experimental characterization of a family of multiemitters is reported.

Since the spectral multiplexing requires starting from beams with a narrow and stable spectrum, which is not the case of high-power semiconductor laser chips, prior to its use it has been necessary to investigate the spectral stabilization of laser diodes with external cavities. This is discussed in Ch. 3, where, to the extend of the author's knowledge, a novel spectral stabilization approach, based on the use of fiber Bragg gratings manufactured by direct point-by-point inscription through femtosecond laser pulse in highly multimode optical fiber, is experimentally presented for the first time.

Finally, Ch. 5 presents the conclusions and provides an outlook on future perspectives of the activities carried out during the three year work.

Acknowledgements

When looked from the outside, the scientific research looks like a very linear journey, where from a starting point A the researcher, with passion and hard work, reaches an already well defined result B. However, this is rarely the case. The scientific research is instead like an exploration, which may or may not lead you where you intended to go, but that always leads you somewhere new. This PhD thesis follows the same rule. It seems that all is linear and well organized, but, until the very end, I did not know exactly where it was leading me.

During this journey, I have been able to count on friends, mentors, and professionals without whom this journey could have not been what it is today.

First of all, I want to thank my supervisor and mentor, prof. Guido Perrone, for guiding and supporting me through this PhD and for believing in me.

I thank also prof. Alberto Vallan from Politecnico di Torino, for lending me his knowledge and for the use of its laboratory.

I would like to acknowledge the support of the PhotoNext lab hosted by the Links Foundation and I want to specially thank Dr. Massimo Olivero for the time he spent helping and supporting me, even when my question where trivial.

I would like to acknowledge the support, both material and conceptual, of Convergent Photonics, a division of Prima Electro S.p.A. In particular, I would like to thank Dr. Roberto Paoletti, Paola Gotta, Claudio Coriasso, Alberto Maina, and Giulia Pippione, and the rest of Convergent Photonics Diode Fab team for their support, collaboration and patience. Many of the experiments I have done would have been impossible without them.

I would like to thank Alessio Califano from nLight Europe for its patience while supporting me with circuits and electronics, two things I actually did not even know how to work with when I started tree years ago.

A sincere thank to Maurizio Carbone, who has helped me with during a period of numerical madness.

Finally, I would like to thank Martina Riva, Valentina Serafini, Aurora Bellone, Antonietta Saggese, Irene Velotti, and Alice Franco for sharing, or having shared, both joy and sadness of the research activity during the last tree years.

Dedico questa tesi alla mia famiglia, senza la quale non sarei arrivato alla fine di questo percorso, ed a Marta, Vittoria, Giacomo, Federico, Davide, Massimiliano e Tullio, che mi hanno supportato ma sopratutto sopportato durante questa esperienza. Sono state parte di questo percorso anche persone le cui strade hanno finito per divergere dalla mia. Tra tutte queste persone, ci tengo a menzionare Daniele.

Contents

List of Tables

List of Figures

List of Acronyms

Acronym	**Description**
A-CBC	Active Coherent Beam Combining
ANN	Artificial Neural Network
ASPW	Angular Spectrum of Plane Waves
BFCL	Beam to Fiber Coupling Loss
BLAS	Band Limited Angular Spectrum
BPP	Beam Parameter Product
CBC	Coherent Beam Combining
CMT	Coupled Mode Theory
CW	Continuous Wave
CZT	Chirp-Z Transform
DBR	Distributed Bragg Reflector
DCF	Double-Clad Fiber
DoP	Degree of Polarization
EOM	Electro-Optical Modulator
FA	Fast Axis
FBG	Fiber Bragg Grating
FCNN	Fully Connected Artificial Neural Network
FL	Fiber Laser
FP	Fabry-Perot
FWHM	Full-Width at Half Maximum
GOF	Geometrical Optics Framework
HPLD	High-Power Laser Diode
LDSS	Laser Diode Spectral Stabilization
LMA	Large Mode Area
LP	Linearly Polarized
MMF	Multi-Mode Fiber
MOPA	Master Oscillator Power Amplifier
NA	Numerical Aperture
NUADAS	Non Uniform ADaptive Angular Spectrum
NUFFT	Non Uniform Fast Fourier Transform
OPD	Optical Path Difference

Acronym	Description
P-CBC	Passive Coherent Beam Combining
PBS	Polarization Beam Splitter
PES	Piezo-Electric Stage
PI	Power vs. current
S-MUX	Spectral Multiplexing
SA	Slow Axis
SMF	Single-Mode Fiber
SNR	Signal-to-Noise Ratio
SPGD	Stochastic Parallel Gradient Descend
SVEA	Slowly Varying Envelope Approximation
TE	Transverse Electric
TM	Transverse Magnetic
TPM	Temporal Phase Mismatch
VBG	Volume Bragg Grating
WDM	Wavelength Division Multiplexing
WOF	Wave Optics Framework

Chapter 1

Introduction

The idea of an ongoing climate change, with its associated dangers for humanity, is not new as the scientific community has been collecting evidences and studying the causes from the early 70s of the XX century [1]. Already at that time, the most likely hypothesis was that the climate change is not due to natural events but to anthropic activities. Today, it is well known that such hypothesis is correct and, having done little, if any, to counteract impact of anthropic activities, the devastating effects of the climate change are becoming more and more evident every day: from increasingly frequent heat and cold waves, to the reduction of biodiversity, from hydrogeological changes, to the melting glaciers, and so on. Although some effects are considered to be already irreversible, the good news is that the climate change can still be reversed; however, this objective requires the development – and the massive adoption – of new technologies. Indeed, unless a worldwide economic degrowth is accepted, new technologies are required to ensure a high level of well-being to everybody, while at the same time reducing the impact on the environment [2]. For example, new manufacturing approaches are necessary to balance high levels of production with a reduction of the CO_2 emissions and of the wastes.

Photonics – in particular, laser based technologies – can significantly help to reach these goals because it can make a large number of applications much more efficient [3, 4]. For instance, laser-based materials processing allows reducing the environmental impact of the manufacturing industry, while photonic sensors allow reducing the resources required in agriculture (the so-called precision farming). In a more general perspective, Photonics is one of the enablers of the transition towards the circular economy [5].

This role of Photonics is not only recognized by the scientific community, but by the market too. For example, as shown in Fig. 1.1, the laser market is growing steadily and it will continue to grow given the role of lasers in the ecological transition [6, 7, 8, 9].

Considering in particular the industrial sector, the high power laser market is currently largely dominated by Fiber Lasers (FLs), which in the last decade have

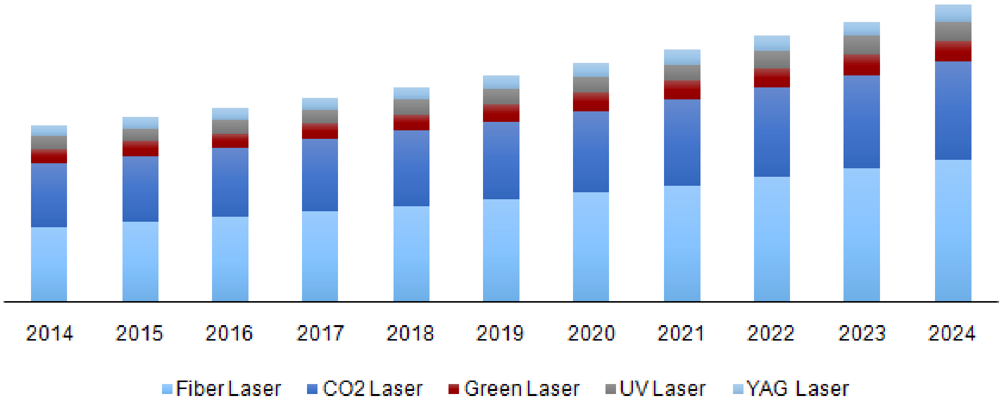

Figure 1.1: A forecast of the laser market trend based on the economic growth observed in the last decade.

overtaken all the other competitors – especially the CO_2 lasers, the standard high power source in early applications –, mainly in the materials processing and military segments [10], thanks to the combination of high beam quality, efficiency, power scalability, simplified thermal management, and lower ownership costs [11, 12].

To better understand the reasons for this success, it is worthy briefly recalling that a fiber laser is a laser in which the active gain medium is an optical fiber doped with rare-earth elements, ytterbium in particular for industrial high-power sources. As schematically shown in Fig. 1.2, the pump is provided by a number of semiconductor laser diodes, usually in the form of multi-emitter modules, which, as the name implies, are devices that combine in single package a plurality of semiconductor laser chips (the single emitters). Then, some multi-emitter modules (or simply “multi-emitters” or “multiemitters”) are coupled to the active fiber though a “pump coupler”, which a device made with the fused-fiber technology that combines a certain number of inputs in a single, larger, output fiber. The choice of using multi-emitters allows minimizing the number of devices that must be individually coupled to the active fiber to obtain the required pump power level; thus it reduces the number of ports of the pump coupler. High-power FLs typically make use of Double-Clad Fibers (DCFs), in which the core is surrounded by two layers of cladding. The lasing mode is generated and propagates in a relatively small core (dimensions can vary from 10 µm to 25 µm), while the pump propagates in a much larger inner cladding layer (dimensions can vary from 125 µm to 400 µm), being confined by the outer cladding. This configuration that makes use of DCFs

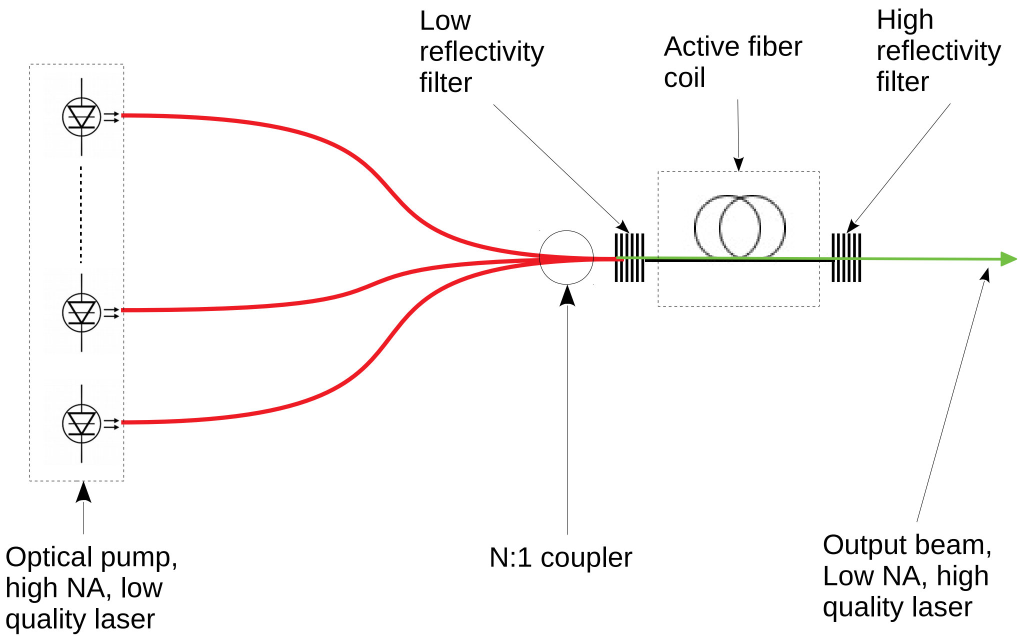

Figure 1.2: Schematic representation of the sub-systems composing a high power fiber laser: a number of laser diodes provide a high power but low beam quality optical pump that is coupled to the active fiber through fused fiber combiners; then the active cavity is formed by a rare-earth doped fiber bounded by two in-fiber mirrors made with fiber Bragg gratings.

is essential to exploit the high-power but low beam quality pump generated by the multi-emitters.

Most of the advantages of FLs are intrinsic to the use of an all-fiber geometry, which simplifies the beam delivery and reduces the mechanical constraints, besides for having a very favorable surface to volume ratio that eases the heat dissipation and for providing a long but compact (it can be coiled) gain medium [13, 14]. However, a great contribution to the success of FLs comes also from the exceptional increase in the performances of the laser diodes used for pumping [15, 16]. All this led to a huge growth in the FL power over the years, fueled by the requests of ever higher production yield [17].

Today, a single semiconductor laser chip can emit in Continuous Wave (CW) up to almost 20 W; then by exploiting a suitable sequence of spatial, spectral, and polarization multiplexing, many of these chips can be combined in a single package using free-space optics to obtain the already mentioned multi-emitter pump modules, which are capable of delivering few hundreds of watts in a large mode area fiber compatible with the inner cladding of DCFs [18, 19]. In turn, these pump modules allow manufacturing fiber laser modules (also known as “laser engines”) that can emit up to more than 2 kW. The higher power levels currently used in industrial sheet metal cutting and welding machines are then achieved by combining some of these laser engines through other types of fused fiber devices known as (high-power) “signal combiners” [14]. This way, it is possible to achieve multi-kilowatt fiber-coupled lasers, with CW output power in the order of 10 kW to 15 kW, although at the expenses of quite a severe degradation in the beam quality due to the necessity of increasing the output fiber diameter when combining several laser engines.

This represents the current state-of-the-art for non special purpose CW high-power FLs; but, considering the trend of the past years, it is not difficult to predict that even higher power levels, especially if associated with higher beam quality, will be required soon. However, the output power of a fiber laser module cannot be arbitrarily scaled up by increasing the pump power due to thermal limitations and the onset of non-linear effects [20, 21, 22]. Moreover, the pump power itself is bounded by the size and the numerical aperture of the pump module delivery fiber [23]. Similarly, for the combination of fiber laser modules, which is limited by the thermal dissipation in the output combiner and by the maximum acceptable Beam Parameter Product (BPP) [14].

Today, power scaling of lasers is obtained mainly through incoherent combination, specifically spatial multiplexing (also known as ”beam stacking”) and polarization multiplexing. Therefore, novel approaches are needed to satisfy the new market requests, which are certainly due to the continuous demand of higher productivity, but are also at least in part driven by the ecological transition.

Two main methods can be used to build new multiplexing schemes, namely Coherent Beam Combining (CBC) and Spectral Multiplexing (S-MUX). As suggested by its name, CBC allows combining an arbitrary number N (at least from the theoretical point of view) of high quality laser beams by exploiting the wave-like nature of light, resulting in a beam whose power is the cumulative power of the constituent beams and whose brightness is N times the cumulative brightness of the constituent beams. The main drawback of this technique is that, being the constituent beams combined both in phase and magnitude, their relative phase difference must be kept as close as possible to zero, a not trivial task to accomplish, especially in operative contexts, explaining why the use of this technique has been mainly limited to laboratories. Nevertheless, the recent progress of electronics opens the way to the implementation of some CBC schemes, making this approach a worthy to explore solution to further scale up power and brilliance of current laser systems.

S-MUX, instead, is an incoherent beam combining technique, as the already mentioned spatial and polarization multiplexing. It allows obtaining a beam whose power and brightness are, theoretically, the cumulative power and brightness of the constituent beams. In other words, using S-MUX it is possible to maintain the beam quality, although this is achieved at the cost of worsening the spectral purity. This may pose strong limitations when the spectral purity is a key aspect, such as in optical pumping of fiber lasers, unless a very dense wavelength combination is implemented. In turn, the latter implies using stabilized beams and specially designed (and selected) dichroic mirrors, which are the devices used to combine beams having different wavelengths. However, given the easier and lower cost of the implementation with respect to CBC, spectral multiplexing can be a promising power scaling technique, at least for all the applications non so sensible to the laser spectral purity, such as in many materials processing applications.

This thesis aims at the identification, theoretical analysis and, when possible, experimental validation of these two "alternative" laser multiplexing schemes. It is organized in three main chapters, each one concerning a method or technology playing a key-role in the development of such novel systems. Each chapter includes both theoretical-simulative studies and experimental results.

In particular, Ch. 2 deals with the coherent multiplexing, a technique that, if it were possible to deploy at an industrial level, would allow an enormous improvement in many manufacturing approaches thanks to the possibility to obtain extremely high power levels without compromising the beam quality. In order to properly study this approach, a novel analytical model, based on the theory of antenna arrays, and a computationally efficient and highly accurate numerical model have been developed. Leveraging on these tools and on the use of neural networks to implement part of the control feed-back system, a new coherent multiplexing scheme has been designed and numerically validated.

Ch. 3 deals with the spectral stabilization of high power laser diodes, which is a practically mandatory preliminary step for spectral multiplexing. More in detail, a rigorous model of the spectral stabilization of broad area, high power laser diodes through Volume Bragg Gratings (VBGs) and Fiber Bragg Gratings (FBGs) is described, together with the realization and experimental validation of prototypes of spectrally stabilized multiemitters. To the author's best knowledge, this is the first time that the spectral stabilization of a high power, large area laser diode is achieved through a Fiber Bragg Grating inscribed by femtosecond laser pulses into a strongly multi-modal optical fiber.

Then, Ch. 4 analyzes the spectral multiplexing, introducing a new stochastic model of spectral multiplexing, which is capable of taking into account the uncertainties of actual high power laser diodes. Also in this case a prototype of a multiemitter based on the spectral stabilization of high power laser diodes, designed according to the aforementioned stochastic method, has been realized and experimentally validated.

Finally, Ch. 5 draws the conclusions and presents an outlook on the future evolution of the discussed technologies.

The activity has led to the publication of 1 journal paper and 5 international conference papers; another journal paper is in preparation.

1. A. Mirigaldi, et al., "Enhanced brightness 180 W compact blue diode laser modules", *Proc. SPIE*, vol. 11983, 2022.

2. G. Pippione, A. Mirigaldi, et al., "100 W high-brightness highly-manufacturable low-SWaP multi-emitter blue laser diode source," *Proc. SPIE*, vol. 11983, 2022.

3. A. Mirigaldi, M. Carbone, and G. Perrone, "Non-uniform adaptive angular spectrum method and its application to neural network assisted coherent beam combining," *Optics Express*, vol. 29, pp. 13269–13287, 2021.

4. G. Pippione, S. Codato, A. Maina, A. Mirigaldi, et al., "Optimized packaging solutions for multi-emitter laser modules," *23rd European Microelectronics and Packaging Conference & Exhibition (EMPC)*, pp. 1-5, 2021.

5. V. Serafini, M. Riva, G. Pippione, A. Mirigaldi, et al., "Compact high-brightness and highly manufacturable blue laser modules," *Proc. SPIE*, vol. 11668, 116680J, 2021.

6. A. Mirigaldi et al., "Power scaling of laser diode modules using high-power DBR chips," *Proc. SPIE*, vol. 11262, 112620W, 2020.

Besides, other research activities carried out during the doctorate, but not part of the core of activities described in this thesis, have led to the publication of the additional journal and conference papers listed in the following.

1. M. Olivero, A. Mirigaldi, et al., "Distributed X-Ray Dosimetry With Optical Fibers by Optical Frequency Domain Interferometry, " *IEEE Transactions on Instrumentation and Measurement*, vol. 70, pp. 1–9, 2021.

2. A. Beccaria, A. Bellone, A. Mirigaldi, et al., "Temperature monitoring of tumor hyperthermal treatments with optical fibers: comparison of distributed and quasi-distributed techniques,"*Optical Fiber Technology*, vol. 60, 102340, 2020.

3. M. Olivero, A. Mirigaldi, et al., "Preliminary investigation of radiation dose sensors based on aluminum-doped silicate optical fibers," *IEEE International Symposium on Medical Measurements and Applications (MeMeA)*, 19856572, 2020.

Chapter 2

Coherent Multiplexing

As mentioned in Ch. 1 there is a constant trend toward the development of higher and higher power and brightness CW laser sources due to the request of a higher production yield. A solution to overcome the beam quality limitations induced by the currently most commonly used incoherent power scaling approaches can be the use of the Coherent Beam Combining (CBC) technique. Indeed, CBC allows combining together a virtually arbitrary number of high power laser beams without any degradation of the beam quality by leveraging on the wave nature of light [24, 25]. Calling N the number of beams to be combined, the CBC exploits the constructive interference among the beams and its most appealing feature is that, provided that the phase difference among the combined lasers is very close to zero, the resulting beam brightness (or brilliance [26]) will scale as N^2, while for any other incoherent multiplexing technique such as spatial or polarization multiplexing, the peak intensity scales as N [27]. The main drawback of CBC is its extreme sensitivity to any kind of noise in the phase difference between the combined beams, which can be intrinsic to the source or be a consequence of thermal and mechanical perturbations [28]. For instance, a phase difference of few tens of mrad would cause a decrease in the brilliance as large as 20%. It is mandatory, therefore, to accurately control the phase of each coherently combined beam. To do so, two main methods are used: the Active Coherent Beam Combining (A-CBC) and the Passive Coherent Beam Combining (P-CBC).

P-CBC is in reality a definition that groups together a multitude of different techniques having in common the absence of an active control of the coherently combined beam phases. Indeed, the P-CBC definition includes methods based on the use of bulk passive optical elements such as Volume Bragg Gratings (VBGs) [29], partially reflecting mirrors in a seed laser configuration scheme [30], and all-fiber couplers in interferometric schemes [31, 32]. The A-CBC method, instead, relies on the active control of the phase and alignment of each beam using PiezoElectric Stages (PES) [33] and Electro-Optical Modulators [34] (EOM) within a closed-control loop. As it can be seen from Fig. 2.1, the collimated laser beams, which are spatially arranged into a 1D or 2D array, are combined into a single beam by a combining element.

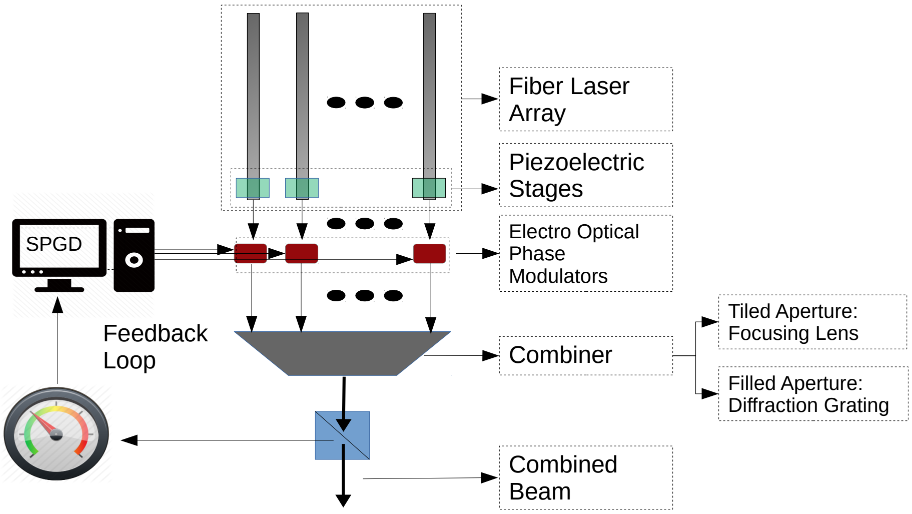

Figure 2.1: Schematic representation of the active coherent beam combining architecture.

In the A-CBC architecture the combing element can either be a focusing lens, or a diffractive optical element, such as a diffraction grating. The resulting architecture is referred to as "tiled aperture" in the first case and "filled aperture" in the second case. If the phase difference between each pair of beam is small enough, in the lens focal plane the beams interfere constructively. Traditionally, each beam phase and alignment are corrected in closed-loop by means of the Stochastic Parallel Gradient Descend (SPGD) algorithm [35], which converts a small amount of the output power in a signal driving the EOMs and PESs.

The combining efficiency η_{cc} is defined as

$$\eta_{\text{cc}} = \frac{I_{\text{cc}}^{\text{max}}}{N^2 \, I_{\text{FL}}^{\text{max}}} \tag{2.1}$$

where I_{cc}^{max} is the maximum power density per unit surface reached by the coherently combined beam and I_{FL}^{max} is the maximum power density per unit surface reached by a single combined fiber laser

Even if it has been demonstrated that P-CBC can reach $\eta_{\text{cc}} \simeq 95\%$ in laboratory conditions and it is implemented in a cheaper and easier way, especially considering an all-fiber configuration, it is less interesting because the reported maximum number of beams that can be combined is about ten. On the other hand, the A-CBC, in particular exploiting the tiled aperture architecture, despite being more expensive due to the use a EOMs and PESs and generally exhibiting a lower combining efficiency, is reported to allow a coherent multiplexing of tens to hundreds of fiber lasers [36, 37, 38], demonstrating of being a very promising technique for extremely high power scaling. For these reasons, only the A-CBC in the tiled aperture architecture has been further analyzed during the PhD, with particular attention to an innovative A-CBC scheme.

The remaining of this chapter is organized as follows. In Sect. 2.1 a simple analytical model of the A-CBC is presented, while in Sect. 2.2 the Wave Optics Framework (WOF), a numerical model based on the Non Uniform ADaptive Angular Spectrum (NUADAS) method, and the scalar diffraction theory to overcome of the limitation of the analytical model in the study of the A-CBC are detailed, together with the presentation of the experimental and numerical validations. Finally in Sect. 2.3 an innovative A-CBC scheme exploiting a Fully Connected Artificial Neural Network (FCNN) is presented and its performance are numerically investigated.

2.1 Simplified analytical model of A-CBC

The tiled aperture A-CBC scheme consists essentially of an array of collimated and synchronized FLs all at the same wavelength. From a purely electromagnetic theory viewpoint, this architecture is analogous to the antenna array architecture nowadays used in emitters for radio telecommunication, as in 4G or 5G repeaters [39]. Therefore, first a brief review of antenna arrays is presented, following the notation used in Ref. [40].

Taking as the reference the position of the first antenna, the other antennas forming an array of N equally oriented identical antennas are set in the locations $\vec{r}_{\mathrm{m}}$ with $m \in \{0, N-1\}$. Altogether the current distribution of the array can be expressed as

$$\vec{J}(\vec{r}) = \sum_{\mathrm{i}=0}^{N-1} \alpha_{\mathrm{i}} \vec{j}_0(\vec{r})(\vec{r} - \vec{r}_{\mathrm{i}}) \tag{2.2}$$

where $\vec{j}_0(\vec{r})$ is the current distribution shared by the antennas in the array and α_{i} is the i-th antenna excitation coefficient. The far field emitted by the antenna array can be computed by the evaluation of the generalized dipole moment in the direction $\hat{r}$. The generalized dipole moment is computed as

$$\vec{P}_{\mathrm{ff}}(\hat{r}) = \vec{I}_{\mathrm{tr}} \cdot \int \vec{J}(\vec{r}\,')\mathrm{e}^{j\,k_0\,\vec{r}\,'\cdot\hat{r}}\mathrm{d}\,\vec{r}\,' \tag{2.3}$$

with $k_0 = 2\pi/\lambda$, being λ the wavelength. Using the change of variable $\vec{v} = \vec{r}\,' - \vec{r}_i$, Eq. 2.3 is reduced to:

$$\vec{P}_{\mathrm{ff}}(\hat{r}) = \left(\vec{I}_{\mathrm{tr}} \cdot \int \vec{j}_0 \mathrm{e}^{j\,k_0\,\vec{v}\cdot\hat{r}} \mathrm{d}\,\vec{v}\right) \left(\sum_{\mathrm{i}=0}^{N-1} \alpha_{\mathrm{i}} \mathrm{e}^{j\,k_0\,\vec{r}_{\mathrm{i}}\cdot\hat{r}}\right) = \vec{p}_{\mathrm{ff},0}(\hat{r})\,\mathcal{F}(\hat{r}) \tag{2.4}$$

where $\vec{p}_{\mathrm{ff},0}$ is the generalized dipole moment of a single source and $\mathcal{F}(\hat{r})$ is a scalar function known as the "array factor". If the antennas are equispaced along the x direction, then $\vec{r}_{\mathrm{m}} = m\,d\,\hat{x}$ so $\hat{r}\cdot\vec{r}_{\mathrm{i}} = m\,d\,\cos(\theta)$, the excitation coefficient α_{m} can be written as $\mathrm{e}^{j\,m\phi_0}$ and the array factor, being in this case a truncated geometrical series, simply reduces to:

$$\mathcal{F}(\psi) = \mathrm{e}^{j\psi(N-1)/2}\frac{\sin(N\psi/2)}{\sin(\psi/2)} \tag{2.5}$$

where $\psi = k_0\,d\,\cos(\theta) + \phi$.

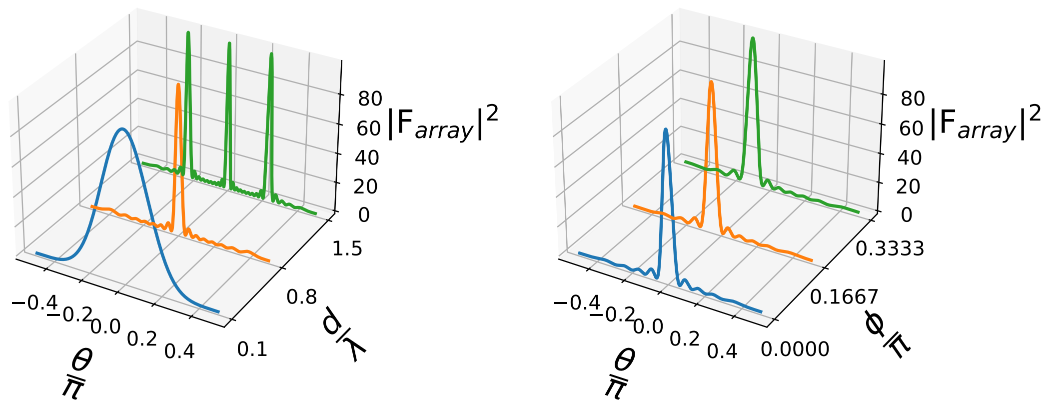

Figure 2.2: Squared magnitude of the antenna array function for different values of the antenna spacing d and phase difference ϕ. Left: fixed $\phi = 0$; right: fixed $d = 0.5\lambda$.

As it can be seen from Fig. 2.2, the main properties of the array function are that

$$\lim_{\psi\to 2\pi m} |\mathcal{F}(\psi)| = N,$$

it is a periodic periodic function with period 2π, it shows a main lobe when $\psi = 0$, corresponding to $\theta_{\mathrm{M}} = \frac{\phi}{k_0 d}$, and has side lobes in the intervals $[\psi_{\mathrm{s}}, \psi_{\mathrm{s+1}}]$, where $0 < \psi_{\mathrm{s}} = \frac{s2\pi}{N} < \pi$. As N increases, the main lobe becomes narrower and narrower, with the consequence that the power per unit of surface that is radiated in the direction identified by θ_{M} from the antenna array at a given distance is $S_0 N^2$, where S_0 is the power per unit of surface that would be radiated by a single antenna at the same distance and in the same direction. In conclusion, the advantage of using an array of synchronized antennas relies in the increase of radiated power density per unit of surface, which is solely related to the phase difference among the antennas.

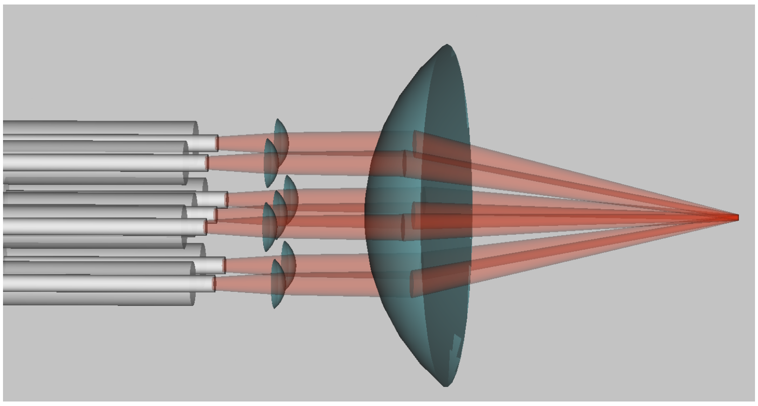

Figure 2.3: Tiled aperture, A-CBC architecture representation. The output of each fiber laser is first collimated and then the whole array field is focused by a focusing system.

As shown in Fig. 2.3, in the A-CBC, tiled aperture architecture, instead, N collimated and synchronized lasers (for example, FLs) at the same emission wavelength are arranged in a 1D or 2D array in front of the combining element. For the sake of simplicity, the lasers are supposed to be arranged on a 1D equispaced array along the x direction of a Cartesian reference system whose z axis is the propagation direction. The overall electromagnetic field in $z = 0$ is:

$$\vec{\mathcal{E}}(\vec{r},0,t) = \mathcal{R}\{\sum_{\mathrm{m}} A_{\mathrm{m}} \vec{e}(\vec{r} - \vec{r_{\mathrm{m}}},0) \mathrm{e}^{-j\,2\pi f t}\} = \mathcal{R}\{\vec{E}(\vec{r},0) \mathrm{e}^{-j\,2\pi f t}\} \tag{2.6}$$

where $\mathcal{R}\{\cdot\}$ stands for the real part of a complex number, $\vec{e}(\vec{r},0)$ is the normalized electric field distribution shared by all the sources, f is the shared laser frequency, and $A_{\mathrm{m}} \in \mathcal{C}$ takes into account the m-th laser total power and initial phase. Being the combined laser monochromatic, in a stationary regime it is enough to study the spatial evolution of the source to completely characterize the electromagnetic field evolution both in time and space. Considering laser beams delivered from fibers having radius of the core R and assuming that the lens input plane distance from the sources z_{lip} is larger than $k_0 R^2/2$, the Fraunhofer approximation holds for each laser and the electric field on the lens input plane is computed as [41]:

$$\begin{aligned}\vec{E}(\vec{r}, z_{\mathrm{lip}}) &= \sum_{\mathrm{m}} A_{\mathrm{m}} \frac{\mathrm{e}^{j\,k\,[z_{\mathrm{lip}} + \frac{||r||^2}{2\,z_{\mathrm{lip}}}]}}{j\,\lambda\,z_{\mathrm{lip}}} \int \mathrm{d}\vec{u}\;\vec{e}(\vec{u} - \vec{r}_{\mathrm{m}},0)\,\mathrm{e}^{-\frac{j\,k\,\vec{r}\cdot\vec{u}}{z}} = \\ &= \sum_{\mathrm{m}} A_{\mathrm{m}} \vec{e}(\vec{r} - \vec{r}_{\mathrm{m}}, z_{\mathrm{lip}}), \\ \vec{e}(\vec{r} - \vec{r}_{\mathrm{m}}, z_{\mathrm{lip}}) &= \frac{\mathrm{e}^{j\,k\,[z_{\mathrm{lip}} + \frac{||r||^2}{2\,z_{\mathrm{lip}}}]}}{j\,\lambda\,z_{\mathrm{lip}}} \int \mathrm{d}\vec{u}\;\vec{e}(\vec{u} - \vec{r}_{\mathrm{m}},0)\,\mathrm{e}^{-\frac{j\,k\,\vec{r}\cdot\vec{u}}{z}}\end{aligned} \tag{2.7}$$

It is worth to analyze the validity of the Fraunhofer approximation. Considering for instance a commercial high power and high brightness fiber laser, the active fiber diameter is typically equal to 20 µm, with an emission wavelength around 1 µm. Therefore, for the Fraunhofer approximation to be valid, z_{lip} must be greater than 6.18 cm. Assuming a collimated output, the distance between the sources and the focusing lens is not fixed and can ideally be as large as needed. This justifies the use of the Fraunhofer approximation even if considering realistic commercial devices, despite it generally requires a small footprint. The total field on the output of the focusing lens is instead computed using the thin lens approximation [41]. Within this approximation, the field on the lens output plane is just the field on the lens input plane times a phase function. In general this phase function could be quite complicated and cumbersome but, assuming that the intensity of the field incident on the lens is negligible outside a radius much smaller than the lens radius, the field on the lens output plane becomes:

$$\vec{E}(\vec{r}, z_{\mathrm{lop}}) = \vec{E}(\vec{r}, z_{\mathrm{lip}})\,\mathrm{e}^{-j\frac{k||r||^2}{2f}} \tag{2.8}$$

where, with reference to Fig. 2.3, z_{lop} is the z coordinate of the plane just after the lens. Once again, here the laser beams are assumed to propagate in homogeneous space, which may be air or any other isotropic and homogeneous medium. Being of interest the overall beam in the focal plane of the lens, the Fresnel approximation is now well suited for the analytical computation of the electric field [41]. Indeed, in the Fresnel regime, the field at a distance z_{f} is computed as:

$$\vec{E}(\vec{r}, z_{\mathrm{f}}) = \sum_{\mathrm{m}} A_{\mathrm{m}} \frac{\mathrm{e}^{j\,k\,[z_{\mathrm{f}} + \frac{||r||^2}{2\,z_{\mathrm{f}}}]}}{j\,\lambda\,z_{\mathrm{f}}} \int \vec{e}(\vec{v} - \vec{r}_{\mathrm{m}}, z_{\mathrm{lip}})\,\mathrm{e}^{-j\frac{k}{2}(\frac{||v||^2}{f} - \frac{||v||^2}{z_{\mathrm{f}}} + \frac{2\vec{v}\cdot\vec{r}}{z\vec{f}})}\,\mathrm{d}\vec{v} \tag{2.9}$$

Setting $z_{\mathrm{f}} = f$ and using the change of variable $\vec{u} = \vec{v} - \vec{r_{\mathrm{m}}}$, Eq. 2.9 simplifies to

$$\begin{gathered}\vec{e}(\vec{r}, z_{\mathrm{f}}) \sum_{\mathrm{m}} A_{\mathrm{m}}\,\mathrm{e}^{-j\frac{k}{z_{\mathrm{f}}}\vec{r}\cdot\vec{r_{\mathrm{m}}}} \\ \vec{e}(\vec{r}, z_{\mathrm{f}}) = \int \vec{e}(\vec{u}, z_{\mathrm{lip}})\,\mathrm{e}^{-j\frac{k}{2}\vec{u}\cdot\vec{r}}\,\mathrm{d}\vec{u}\end{gathered} \tag{2.10}$$

It is important to note that $\vec{e}(\vec{r}, z_{\mathrm{f}})$ is exactly the field of a single source in the origin of the reference system and propagated through the same optical path as the whole laser array. Therefore, analogously to the case of the antenna array, the array factor for an array of laser sources can be defined as:

$$F_{\mathrm{laser}}(\vec{r}; z_{\mathrm{f}}) = \sum_{\mathrm{m}} A_{\mathrm{m}} \exp\left[-j\frac{k}{z_{\mathrm{f}}}\vec{r}\cdot\vec{r}_{\mathrm{m}}\right] = \sum_{\mathrm{m}} \exp\left[m\left(j\phi - \frac{k}{z_{\mathrm{f}}}\delta_{\mathrm{x}}x\right)\right] \tag{2.11}$$

with $A_{\mathrm{m}} = \mathrm{e}^{j\,m\,\phi}$ and $\vec{r}\cdot\vec{r}_{\mathrm{m}} = \dfrac{k\delta_{\mathrm{x}}x}{z_{\mathrm{f}}}$. The Fresnel approximation holds for not too large (as in the Fraunhofer approximation) but not too small propagation distances. Considering more than two sources, the combining lens has typically a focal distance from tens to hundreds of millimeters, which are values that make the Fresnel approximation valid. For comparison, a case in which the Fresnel approximation doesn't hold in is that of the propagation through microlenses, whose focal distance typically does not exceed 1 mm. However, this is not a practically relevant case for high power laser beam combining.

As in the case of antenna arrays, the array factor can be elegantly expressed as:

$$F_{\mathrm{laser}}(\vec{r}, z_{\mathrm{f}}) = \exp\left\{-j\frac{(N-1)}{2}\left[\frac{k}{z_{\mathrm{f}}}\delta_{\mathrm{x}}x - \phi\right]\right\}\frac{\sin\left(\frac{N}{2}\left(\frac{k}{z_{\mathrm{f}}}\delta_{\mathrm{x}}x - \phi\right)\right)}{\sin\left(\frac{1}{2}\left(\frac{k}{z_{\mathrm{f}}}\delta_{\mathrm{x}}x - \phi\right)\right)} \tag{2.12}$$

It is worth noting that, in the case of lasers, the array factor is not a function of the propagation direction but of the coordinate x in the focal plane. In the most general case, more than two lasers may be disposed in a 2D array, leading to an array factor dependent, in general, on both x and y coordinates. Nevertheless, the properties of this array factor would be exactly the same as in the case of a 1D source array; therefore, for the sake of simplicity, the properties of the array factor for the uniform, 1D source array only are discussed. Setting $\psi = \dfrac{k}{z_{\mathrm{f}}}\delta_{\mathrm{x}}x - \phi = \psi$, when ψ tends to $m\,2\pi$, the array factor tends to N and the intensity of the field resulting from the coherent combination scales as N^2, as observed experimentally. The coordinate of the main lobe of the array function is simply given by $x_{\mathrm{max}} = \phi\,\dfrac{z_{\mathrm{f}}}{k\delta_{\mathrm{x}}}$. Clearly, a controlled variation of the phase difference between the sources allows changing x_{max} and for $\phi = 0$ the main lobe is exactly in $x = 0$. As for the antenna array, also for the laser array it can be defined a visible range corresponding to the range $[-x_{0.95}, x_{0.95}]$, $x_{0.95}$ such that $|e(x_{0.95}, y, z_{\mathrm{f}})|^2 = 0.9\max_{\mathrm{x}}\{e(x, y, z_{\mathrm{f}})\}$. The reason for this definition of the visible range for laser arrays is that outside of this range the overall intensity of the combined laser is negligible. Therefore, the total number of visible lobes corresponds to the number of zeros of the laser array function within the interval minus one, so that the number of visible side lobes is simply the number of lobes minus two. For instance, Fig. 2.4 shows the intensity profile of the beam resulting from the A-CBC of two fiber lasers in the

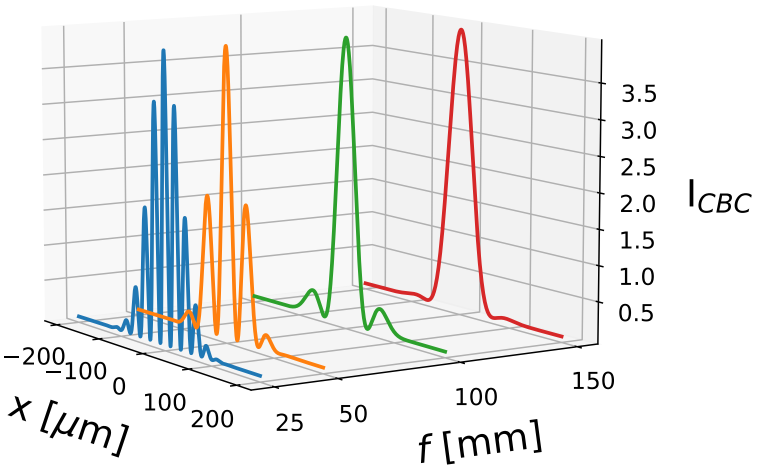

Figure 2.4: Intensity distribution of a beam resulting from CBC of two fiber lasers in the tiled aperture architecture for several values of the lens focal length along the laser array direction.

tiled aperture architecture. The considered fiber lasers are two lasers emitting a purely TEM_{00} Gaussian beam, at a wavelength of 1064 nm, with a peak intensity of 1 W, a core diameter of 50 µm, and a center to center distance of 1 mm. As discussed, the combined beam shows a peak intensity equal to 4 W, scaling in ideal condition as N^2 with respect to the single beam peak intensity. In addition, it is clear that, not only the number of side lobes decreases as the focal length increases, but also the full width half maximum of the main lobe increases as the focal length increases. Therefore, on the one hand, the use of a smaller focal length results in a greater density of power per unit of surface, but a smaller delivered power due to the relatively high intensity of the secondary lobes in the visible range; on the other hand, the use of a longer focal length results in an increase of the total power within the main lobe, but in a smaller density of power per unit of surface.

2.2 Wave optics framework for A-CBC

The analytical model illustrated in Sect. 2.1 is quite useful to evaluate the performance of the tiled aperture A-CBC. Indeed, it allows studying the efficiency of the tiled aperture A-CBC, the impact of secondary lobes and the strategies to avoid them; however, it lacks of flexibility. The closed expression for the laser array factor is only valid under well defined optical regimes, namely the Fraunhofer approximation regarding the distance between the source array and the focusing lens and the Fresnel approximation concerning the lens focal plane where, effectively, the sources are coherently combined. Needless to say, it is convenient to rely on a more sophisticated model to study the A-CBC not only when the above-mentioned approximations are not valid, but also in regions different from the combining element focal plane.

Traditionally, the most used framework to study the propagation of laser beams through an optical path is the geometrical optics. With this method, any laser beam is approximated as an envelope of rays whose trajectories are determined by the eikonal equation [42]. This approach allows converting any light propagation problem through homogeneous space and common optical elements (e.g., prisms, lenses, and mirrors) in a matrix multiplication problem, making it also cheap from the computational point of view. However, the wave nature of light is completely neglected; hence, any phenomenon due to the wave-like nature of light cannot be modeled. Therefore, since the CBC is a direct consequence of the wave-like nature of light, the geometrical optics is not well suited to simulate it.

The geometrical optics limits can be partially overcome by the five rays model [43, 44]. According to this model, any beam is approximated by an equivalent Gaussian beam whose beam size and divergence along a given axis are determined by the propagation of five rays, whose trajectory can be determined using the methods of geometrical optics, reducing again the propagation problem to a matrix multiplication problem. Even if within this framework the information relative to the beam phase can be easily retrieved, the five ray model is valid only under the paraxial approximation, limiting the range of possible optical architectures that can be studied with a reasonable accuracy.

In order to fully take into account the wave-like nature of light propagation without relying on limiting approximations, the wave optics framework is the best suited. Indeed, it is the most accurate framework because it is based on the numerical solution of the scalar Helmholtz equation, which can be directly derived from Maxwell equations [45]. In addition to this, a wave optic model is the only usable model when it comes to filled aperture geometries. In filled aperture geometries, the combining element is generally a diffraction grating, which is poorly modeled in the geometrical optics framework and cannot be modeled at all within the five ray model.

In the following subsection 2.2.1 an innovative numerical simulation method based on the wave optics framework is presented; then its validation against experimental data and numerical benchmark is discussed in subsection 2.2.2.

2.2.1 Wave Optics Framework Formulation

In the Wave Optics Framework (WOF) the problem of the propagation of an arbitrary laser beam through a given optical path may be split in two main sub-problems: the propagation through a homogeneous medium and the propagation through common optical elements, such as lenses and mirrors.

Non Uniform ADaptive Angular Spectrum method

The first sub-problems can be effectively addressed as the propagation of a laser beam from a source plane to a destination plane, which can be efficiently solved by means of the Angular Spectrum of Plane Waves (ASPW) [46]. However, if the source plane is also tilted with respect to the destination plane, the ASPW becomes cumbersome due to the limitations imposed by the Fast Fourier Transform (FFT) algorithm [47]. Moreover, it is well known that a brute force application of the ASPW generates large numerical errors, especially when the propagation distance is large, leading to an increase of the spatial resolution with a correspondent increase of computational cost. Therefore, to overcome these limitations, a new algorithm named Non Uniform ADaptive Angular Spectrum (NUADAS), which is based on the Non Uniform Fast Fourier Transform (NUFFT) [48], the Band Limited Angular Spectrum (BLAS) [49], and the Chirp-Z Transform (CZT) [50] has been developed.

Part of the work described in this section has been published by the author in Ref. [51]. The propagation of a laser beam in an arbitrary direction with respect to a target plane with an arbitrary polarization in an homogeneous isotropic dielectric medium is solved in terms of the scalar Helmoltz equations, one for each polarization, with assigned beam complex amplitude in the origin of the system [45]:

$$\nabla^2 g(\vec{r}) + \epsilon\mu\omega^2\, g(\vec{r}) = 0 \tag{2.13}$$

where $g(\vec{r})$ stands for the amplitude of the modes composing the beam, μ is the magnetic permittivity and ϵ the dielectric constant of the medium assumed to be isotropic and homogeneous. As well known, the solution of Eq. 2.13, given its boundary value $g(\vec{r}_\mathrm{i})$, $r_\mathrm{i} \in \{\vec{r} \in \mathcal{R}^3 | z = z_0\}$, with $z_0 = 0$ for simplicity, is:

$$\begin{gathered} g(\vec{r}_\mathrm{f}) = \int_{\mathcal{R}^2} \mathrm{d}f_\mathrm{x}\, \mathrm{d}f_\mathrm{y}\, \hat{g}(f_\mathrm{x},\, f_\mathrm{y};\, 0)\, \mathrm{e}^{-j\,2\pi\,\vec{f}\cdot\vec{r}_\mathrm{f}} \\ \hat{g}(\vec{f};0) = \int_{\mathcal{R}^2} \mathrm{d}x\, \mathrm{d}y\, g(\vec{r}_\mathrm{i})\mathrm{e}^{j2\pi\vec{f}\cdot\vec{r}_\mathrm{i}} \\ \vec{f} = \left(f_\mathrm{x},\, f_\mathrm{y},\, f_\mathrm{z} = \sqrt{\lambda^{-2} - f_\mathrm{x}^2 - f_\mathrm{y}^2}\right)^T \end{gathered} \tag{2.14}$$

being f_i the i-th spatial frequency, $\vec{r}_\mathrm{i}$ and $\vec{r}_\mathrm{f} = \mathbf{R}(\vec{r}_\mathrm{i} + \vec{d})$ the points belonging to the source and target planes, respectively, and $\vec{d}$ the distance, as sketched in Fig. 2.5. It is immediate to recognize that Eq. 2.14 requires computing a Fourier transform integral, which relates space and spatial frequency coordinates. In general, the propagation equation can be solved only with numerical approaches because either the boundary conditions are only numerically known or the Fourier transform cannot be analytically computed.

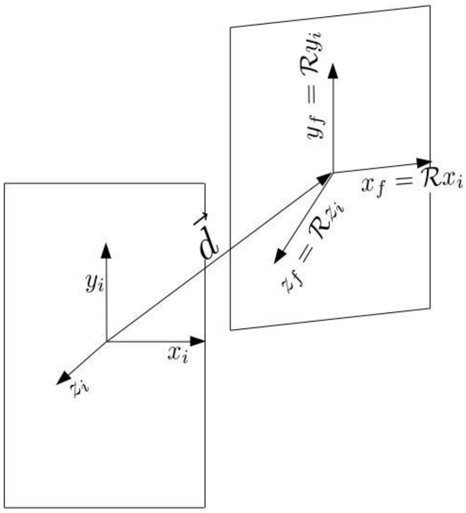

Figure 2.5: A practical scenario in which the propagation of a beam emitted by a laser has to be computed for a target plane that is tilted and shifted with respect to the source plane.

The commonly used method to numerically solve this problem is the cited ASPW, whose key point is to approximate the continuous Fourier transform in Eq. 2.14 with a discrete Fourier transform, which can then be computed using the FFT algorithm. Indeed, considering a finite input plane of size $(S_\mathrm{x},\ S_\mathrm{y})$ such that $g(\vec{r_\mathrm{i}}) \simeq 0$ at its edges, discretized into $N_\mathrm{x} \times N_\mathrm{y}$ points (respectively, along x and y), it is possible to introduce the discrete Fourier transform (indicating the transformed quantity with the caret accent) as:

$$\hat{g}_\mathrm{i}[s,t] = \Delta_\mathrm{x}\, \Delta_\mathrm{y}\, \mathrm{FFT}\left(g_\mathrm{i}[l,m]\right)[s,t] \tag{2.15}$$

with:

$$\begin{gathered} \hat{g}_\mathrm{i}[s,t] = \hat{g}\left(s\Delta f_\mathrm{x},\ t\Delta f_\mathrm{y};\ 0\right), \quad g_\mathrm{i}[l,m] = g\left(l\Delta_\mathrm{x},\ m\Delta_\mathrm{y},\ ,0\right) \\ \Delta f_\mathrm{i} = 1/L_\mathrm{i}, \quad \Delta_\mathrm{i} = L_\mathrm{i}/N_\mathrm{i}, \quad \mathrm{i} = x, y \\ I_\mathrm{K} = \left\{-\frac{K}{2}, ..., \frac{K}{2} - 1\right\}, \quad s, l \in I_{\mathrm{N_x}}, \quad t, m \in I_{\mathrm{N_y}} \end{gathered} \tag{2.16}$$

The field on the target plane is then computed as:

$$\begin{gathered} g_\mathrm{f}[s,t] = \Delta f_\mathrm{x}\, \Delta f_\mathrm{y}\, \mathrm{IFFT}\left(\hat{g}_\mathrm{f}[l,m]\right) \\ f_\mathrm{z}^2[l,m] = \lambda^{-2} - (l\, \Delta f_\mathrm{x})^2 - (m\, \Delta f_\mathrm{y})^2 \\ \hat{g}_\mathrm{f}[l,m] = \hat{g}_\mathrm{i}[l,m]\, \mathrm{e}^{-j\, 2\pi\, f_\mathrm{z}[l,m]\, z} \end{gathered} \tag{2.17}$$

where FFT( ) and IFFT( ) denote the computation of, respectively, the direct and inverse discrete Fourier transform by means of the Fast Fourier Transform algorithm. If $f_\mathrm{z}^2[l,s] < 0$, the corresponding wave is evanescent and does not give any contribution to the propagation for reasonably long distances; therefore $\hat{g}_\mathrm{f}[l,m]$ can be set to zero for these frequencies.

The ASPW method is simple and straightforward to implement but presents some drawbacks. The first drawback is the constraint on the dimensions, discretization step, and number of points on the target plane, which are all automatically fixed by the corresponding values chosen for the input plane description, principally due to the use of the plain FFT algorithm. The second drawback is that the ASPW method, as formulated above, gives good results for near field propagation only. The third and more important drawback is that it only allows propagating the source field to planes that are parallel to the source one. All these limitations can be overcome with the NUADAS method as proposed in this work.

As pointed out in Ref. [49], the small accuracy of the ASPW with increasing propagation distance is due to a non proper sampling of the transfer function in the frequency space, $H(f_\mathrm{x},\, f_\mathrm{y}) = \mathrm{e}^{j\,\phi(f_\mathrm{x},\, f_\mathrm{y})} = \mathrm{e}^{-j\,2\pi f_\mathrm{z}\, z}$. As a matter of fact, $H(f_\mathrm{x},\, f_\mathrm{y})$ is a chirp function and to avoid aliasing errors the Nyquist theorem requires that

$$\Delta f_\mathrm{x} > \left| \frac{1}{\pi} \frac{\partial \phi}{\partial f_\mathrm{x}} \right|, \quad \Delta f_\mathrm{y} > \left| \frac{1}{\pi} \frac{\partial \phi}{\partial f_\mathrm{y}} \right|$$

So, a first improvement is to use the Band Limited Angular Spectrum (BLAS) [49] for which

$$\begin{aligned} &\frac{f_\mathrm{x}^2}{f_{\mathrm{x,\,lim}}^2} + \frac{f_\mathrm{y}^2}{\lambda^{-2}} \leq 1, \quad f_{\mathrm{x,\,lim}} = \lambda^{-1}\left(\frac{2z}{S_\mathrm{x}} + 1\right)^{-1/2} \\ &\frac{f_\mathrm{y}^2}{f_{\mathrm{y,\,lim}}^2} + \frac{f_\mathrm{x}^2}{\lambda^{-2}} \leq 1 \quad f_{\mathrm{y,\,lim}} = \lambda^{-1}\left(\frac{2z}{S_\mathrm{y}} + 1\right)^{-1/2} \end{aligned} \tag{2.18}$$

where S_x, S_y define the computational window size. Again, since evanescent waves are not taken into account, the complex amplitude associated to any frequency not satisfying Eq. 2.18 is forced to zero. On the other hand, if Eq. 2.18 holds, the accuracy of the ASPW method increases considerably also for moderately large propagation distances z, although, when z becomes larger than about forty times the size of the computational window, the accuracy decreases again. In fact, when using the FFT algorithm, the fixed computational window size makes Δf_x and Δf_y to be fixed too, so the number of points satisfying Eq. 2.18 decreases as z increase. This implies that, when z becomes significantly large, the number of non-zero complex amplitude values becomes too small to guarantee good results. A straightforward solution is to use larger computational windows, but this leads to an increase of the computational time and of the machine requirements. A more convenient solution is to use the chirp-z transform [50, 52] to avoid the limitations of the FFT. The proper computational window size for a given propagation distance is [53]:

$$S_{\mathrm{i}} = max \left\{ \frac{2\sqrt{2}\, z\, M_{\mathrm{i}}\, \lambda}{\sqrt{-M_{\mathrm{i}}^2\, \lambda^2 + \sqrt{M_{\mathrm{i}}^4\, \lambda^4 + 64\, z^2\, M_{\mathrm{i}}^2\, \lambda^2}}},\ L_{\mathrm{i}} \right\} \tag{2.19}$$

so that $\Delta f_{\mathrm{i}} = S_{\mathrm{i}}^{-1}$ with M_{i} being the number of equispaced points needed in the frequency region defined by Eq. 2.18 and L_{i} being the minimum computational window size.

It is clear that, since $\Delta_{\mathrm{i}}\, \Delta f_{\mathrm{i}}$ is not necessarily equal to $1/M_{\mathrm{i}}$, a “plain” FFT method cannot be used anymore. The discrete Fourier transform can, anyway, be rewritten in term of a chirp z-transform as:

$$\begin{gathered} \hat{g}_{\mathrm{i}}[l,m] = \Delta_{\mathrm{x}}\, \Delta_{\mathrm{y}} \sum_{\mathrm{s,t}} g_{\mathrm{i}}[s,t] \mathrm{e}^{w\, j\, 2\pi\, (\alpha_{\mathrm{x}}\, l\, s + \alpha_{\mathrm{y}}\, m\, t)} = \\ = \sum_{\mathrm{s,t}} g_{\mathrm{i}}[s,t] \mathrm{e}^{w\, j\, \pi\, (\alpha_{\mathrm{x}}\, s^2 + \alpha_{\mathrm{y}}\, t^2)} \mathrm{e}^{-w\, j\, \pi (\alpha_{\mathrm{x}}\, (l-s)^2 + \alpha_{\mathrm{y}}\, (m-t)^2)} \times \\ \times \mathrm{e}^{w\, j\, \pi (\alpha_{\mathrm{x}}\, l^2 + \alpha_{\mathrm{y}}\, m^2)}\, \Delta_{\mathrm{x}}\, \Delta_{\mathrm{y}} \end{gathered} \tag{2.20}$$

At this point, thanks to the convolution theorem Eq. 2.20 can be computed using an FFT, actually an ADAptive Fast Fourier Transform that we therefore call ADAFFT, as:

$$\begin{gathered} \mathrm{e}^{w\, j \pi\, (\alpha_{\mathrm{x}} l^2 + \alpha_{\mathrm{y}}\, m^2)} \Delta_{\mathrm{x}}\, \Delta_{\mathrm{y}}\, \mathrm{IFFT}\, (a[s,t]\, b[s,t]) = \\ = \Delta_{\mathrm{x}}\, \Delta_{\mathrm{y}}\, \mathrm{ADAFFT}(g_{\mathrm{i}}[l,m]) \\ a[s,t] = \mathrm{FFT} \left(g_{\mathrm{i}}[s,t]\, \mathrm{e}^{w\, j\, \pi\, (\alpha_{\mathrm{x}}\, s^2 + \alpha_{\mathrm{y}}\, t^2)} \right) \\ b[s,t] = \mathrm{FFT} \left(\mathrm{e}^{-w\, j\, \pi\, (\alpha_{\mathrm{x}}\, s^2 + \alpha_{\mathrm{y}}\, t^2)} \right) = \\ = \frac{1}{-j\, w\, \sqrt{\alpha_{\mathrm{x}}\, \alpha_{\mathrm{y}}}}\, \mathrm{e}^{\dfrac{j\, \pi}{w} \left(\dfrac{s^2}{M_{\mathrm{x}}} + \dfrac{t^2}{M_{\mathrm{y}}^2\, \alpha_{\mathrm{y}}} \right)} \end{gathered} \tag{2.21}$$

with $\alpha_{\mathrm{i}} = \Delta_{\mathrm{i}}\, \Delta f_{\mathrm{i}}$ and $w \in \{-1, +1\}$ to take in consideration both the direct and inverse Fourier transforms and $s \in I_{\mathrm{M_x}}, t \in I_{\mathrm{M_y}},\ M_{\mathrm{i}} \neq N_{\mathrm{i}}$ in general.

It has to be pointed out that the ADAFFT allows overcoming another of the limitations in the ASPW highlighted earlier above and due to use of the “plain” FFT. Indeed, in the ADAFFT the number of points in the Fourier domain, as well as the sampling frequencies Δf_{i}, are only limited by the Nyquist theorem

$$M_{\mathrm{i}}\, \Delta f_{\mathrm{i}} \leq \frac{1}{\Delta_{\mathrm{i}}} \tag{2.22}$$

while the algorithm keeps the same computational complexity $O(N\, \log N)$ as the usual FFT.

Finally, it is possible to analyze the last constraint limiting the ASPW, namely the parallelism condition between the source and target plane. Considering the propagation of a laser beam that is tilted with respect to a target plane, the field on the source plane, $g_{\mathrm{f}}[l,m]$, can be computed as

$$\begin{aligned} g_{\mathrm{f}}[l,m] &= \Delta f_{\mathrm{x}}\,\Delta f_{\mathrm{y}} \sum_{\mathrm{s,t}} \hat{g}_{\mathrm{i}}[s,t]\,\mathrm{e}^{-j\,2\pi\,\vec{f}[s,t]\cdot\mathbf{R}(\vec{d}+\vec{r}_{\mathrm{i}}[l,m])} = \\ &= \mathrm{e}^{-j\,2\pi\,\vec{f}_0\cdot\vec{r}_{\mathrm{i}}[l,m]}\,\Delta f_{\mathrm{x}}\,\Delta f_{\mathrm{y}} \sum_{\mathrm{s,t}} \hat{g}_{\mathrm{d}}[s,t]\,\mathrm{e}^{-j\,2\pi\,\tilde{f}[s,t]\cdot\vec{r}_{\mathrm{i}}[l,m]} \end{aligned} \tag{2.23}$$

where

$$\begin{gathered} \hat{g}_{\mathrm{d}}[s,t] = \mathrm{e}^{-j\,2\pi\,\vec{f}\cdot\mathbf{R}\vec{r}_{\mathrm{i}}}, \quad \vec{f}[l,m] = (\,l\,\Delta f_{\mathrm{x}},\,\Delta f_{\mathrm{y}},\,f_{\mathrm{z}}[l,m])^T \\ \vec{f}_0 = (\min(\mathbf{R}\vec{f}[l,m])_{\mathrm{x}},\,\min(\mathbf{R}\vec{f}[l,m])_{\mathrm{y}})^T \\ F_{\mathrm{i}} = \left(\max(\mathbf{R}\vec{f}[l,m]) - \vec{f}_0\right)_{\mathrm{i}}\,\Delta_{\mathrm{i}} \\ \tilde{f}_{\mathrm{i}} = \left[(\mathbf{R}\vec{f})_{\mathrm{i}} - f_{0,\mathrm{i}}\right]/F_{\mathrm{i}}, \quad r_{\mathrm{i}}[l,m] = \left(\frac{l}{F_{\mathrm{x}}},\,\frac{m}{F_{\mathrm{y}}}\right) \end{gathered} \tag{2.24}$$

It is now clear that the complex amplitude $\hat{g}_{\mathrm{d}}[s,t]$ is associated to non equispaced frequency coordinates $\tilde{f}[l,m]$, normalized to the interval $[0,2\pi]$, due to a rotation of the coordinates in the Fourier space [54, 55, 56]. In this case it is necessary to resort to the Non Uniform Fast Fourier Transform (NUFFT) for the evaluation of $g_{\mathrm{f}}[l,m]$ because the NUFFT allows computing the Fourier transform of a field even in the case of a non uniform sampling, in any or both of the frequency and spatial domains. In order to apply the NUFFT to an unevenly sampled field, firstly a regularization step is required:

$$\begin{gathered} \eta(f_{\mathrm{x}},\,f_{\mathrm{y}}) = \sum_{\mathrm{l,m}} \hat{g}_{\mathrm{d}}[l,m]\,\delta(f_{\mathrm{x}} - \tilde{f}_{\mathrm{x}}[l,m])\,\delta(f_{\mathrm{y}} - \tilde{f}_{\mathrm{y}}[l,m]) \\ \tilde{\eta} = (\eta * \phi)(f_{\mathrm{x}},\,f_{\mathrm{y}}) = \\ \int_{\mathcal{R}^2} \mathrm{d}\,f'_{\mathrm{x}}\,\mathrm{d}f'_{\mathrm{y}}\,\eta(f'_{\mathrm{x}},\,f'_{\mathrm{y}})\,\phi_{\mathrm{x}}(f_{\mathrm{x}} - f'_{\mathrm{x}})\,\phi_{\mathrm{y}}(f_{\mathrm{y}} - f'_{\mathrm{y}}) = \\ = \sum_{\mathrm{l,m}} \hat{g}_{\mathrm{d}}[l,m]\,\phi_{\mathrm{x}}(f_{\mathrm{x}} - \tilde{f}_{\mathrm{x}}[l,m])\,\phi_{\mathrm{y}}(f_{\mathrm{y}} - \tilde{f}_{\mathrm{y}}[l,m]) \end{gathered} \tag{2.25}$$

with ϕ being a regularization function with a compact support in both the Fourier and real spaces; for instance it can be a Gaussian function or an N-order spline. Next, the convolution theorem is applied:

$$\begin{gathered} \mathcal{F}\{\tilde{\eta}\} = \mathcal{F}\{\eta(f_{\mathrm{x}}, f_{\mathrm{y}})\}\,\mathcal{F}\{\phi(f_{\mathrm{x}})\}\,\mathcal{F}\{\phi(f_{\mathrm{y}})\} \Longrightarrow \\ \mathcal{F}\{\eta\} = \frac{\mathcal{F}\{\tilde{\eta}\}}{\mathcal{F}\{\phi(f_{\mathrm{x}})\}\,\mathcal{F}\{\phi(f_{\mathrm{y}})\}} = \frac{\mathrm{ADAFFT}(\tilde{\eta})}{\mathcal{F}\{\phi(f_{\mathrm{x}})\}\,\mathcal{F}\{\phi(f_{\mathrm{y}})\}} \end{gathered} \tag{2.26}$$

The algorithm can be speeded up by noticing that only the discrete Fourier transform of $\tilde{\eta}$ needs to be computed numerically, while an analytically Fourier transformable regularization function can be chosen. Finally, the anti-Fourier transform of $\tilde{g}_\mathrm{d}$ can be recovered:

$$\begin{aligned} g_\mathrm{f}[l,m] = \Delta f_\mathrm{x}\,\Delta f_\mathrm{y}\,\mathrm{e}^{-j\,2\pi\,\vec{f}_0\cdot\vec{r}_\mathrm{i}[l,m]}\,\frac{\mathrm{ADAFFT}(\tilde{\eta})[l,m]}{\mathcal{F}\{\phi(f_\mathrm{x},f_\mathrm{y})\}} = \\ = \mathrm{NUADAS}\{g_\mathrm{i}[s,t]\}[l,m] \end{aligned} \tag{2.27}$$

where NUADAS is a new acronym introduced to indicate a Non-Uniform ADAFFT, so it is basically the combination of applying the NUFFT to the ADAFFT approach.

In conclusion, it is worth noticing that the use of the proposed approach allows controlling the sampling frequency and the number of samples in each domain, making it possible to analyze also complex systems with an acceptable computational complexity and an arbitrary precision.

Common optical elements within the wave optics framework

As discussed at the beginning of this subsection, a typical optical path consists of homogeneous space, which can be studied with the NUADAS approach, and of optical elements, such as lenses and mirrors. In geometrical optics the lens and mirrors are described by ray transfer matrices, which allow relating the coordinates and the direction of each ray at the optical element input to the coordinates and direction of the same ray at the optical element output [57]. In a WOF, the optical elements must be seen as complex transformations globally acting on the beam complex amplitude at the element input plane. The result of this transformation is the beam complex amplitude at the element output plane. While from a mathematical point of view the use of complex transformations is a little bit more cumbersome than the use of ray transfer matrices, it allows fully taking into account the wave-like nature of light, linking not only the amplitude, but also the phase of the beam at the output of the optical element to the amplitude and phase of the beam at its input. In the following, two main optical elements are discussed: lenses and mirrors.

A mirror simply rotates the propagation direction and polarization of a laser beam; hence, it is modeled as a rotation of coordinates though a rotation matrix $\mathbf{M}(\theta)$ times a clipping function $v_\mathrm{cl}(x,y)$:

$$v_\mathrm{cl}(x,y) = \left\{ \begin{array}{ll} 0 & (x,y) \notin \text{clear aperture} \\ \alpha_\mathrm{mir} & (x,y) \in \text{clear aperture} \end{array} \right\} \tag{2.28}$$

where $\alpha_\mathrm{mir} \leq 1$ models a possible loss due to the non ideal behavior of the mirror in addition to the clipping effect. In reality, on the edge of the mirror, the field should not be put equal to zero since some diffraction may occur. A more accurate clipping function can be written in terms of a super-Gaussian function as:

$$\tilde{v}_\mathrm{cl}(x,y) = \alpha_\mathrm{mir}\exp\left[\left(-\frac{x}{w_\mathrm{x}}\right)^{2n} - \left(\frac{y}{w_\mathrm{y}}\right)^{2m}\right] \tag{2.29}$$

The clipping function $\tilde{v}_{\text{cl}}(x, y)$ tends to $v_{\text{cl}}(x, y)$ as n and m become larger and larger, but does never completely cut the input field. However, in practical applications, the extension of the mirrors is such that the field modulus away from their centers is negligible; therefore, the two clipping functions have essentially the same effect and the choice of one instead of the other is dictated by the computational cost, which are smaller for v_{cl} than for $\tilde{v}_{\text{cl}}$. All in all, an arbitrary beam complex amplitude, after incidence on a mirror, is:

$$\vec{\mathcal{E}}\,'(x', y'; z_{\text{out}}) = \mathbf{M}(\theta)\,\vec{\mathcal{E}}(x, y; z_{\text{in}})v_{\text{cl}}(x, y) \tag{2.30}$$

where $(x', y', z_{\text{out}})^T = \mathbf{M}(\theta)(x, y, z_{\text{in}})^T$.

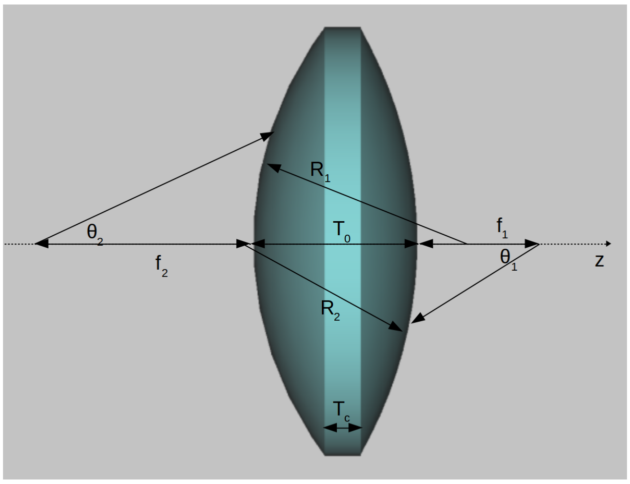

Figure 2.6: Schematic illustration an arbitrary lens: f_{i} indicates for the i-th focal length, which may be different for the back and front lens surface, if the back and front radius are different. In addition are also illustrated the front and back acceptance angle and radius of curvature. The z direction is customarily taken as the optical axis.

Lenses are quite complex elements compared to mirrors. Within the geometrical optics framework, a lens may be described by a cascade of matrices corresponding to the various simpler parts in which a lens can be subdivided, as shown in Fig. 2.6: the input and output curved surface regions with refractive index n_{lens} or n_{out} depending on the transverse position and a central part that corresponds to the propagation through a homogeneous space with refractive index n_{lens}. Within this framework, the properties of the lens are mostly given by the lens NA and the lens focal length. As pointed out in Ref. [58], the lens numerical aperture gives a measure of the acceptance angle of the lens. In general, the complex transformation describing the effect of an arbitrary lens on an input beam would require a vectorial description of the beam itself. However, if the lens NA is restricted to a value smaller than 0.5, a simplified, scalar description of the lens effect, known as the thin lens approximation, is possible [45, 59, 60]. The thin lens approximation in the WOF must not be confused with the homonym approximation in the geometrical optics framework. Indeed, in the latter the thin lens approximation allows expressing the lens ray transfer matrix as a function of the lens focal length solely if the lens radius of curvature is way larger than the lens central thickness; otherwise the ray transfer matrix associated with the lens can be constructed as the product of the lens transfer matrix of the input interface, the lens homogeneous part and the output interface. Instead, in the WOF, the thin lens approximation only relates to the lens numerical aperture: if the lens numerical aperture is small enough, then the i-th component of the electric field at the lens output interface is solely a function of the same component at the lens input interface, therefore any coupling among different components is considered negligible. However, for a scalar description to be sufficient, it is also needed that the lens optical axis is at most shifted with respect to the propagation direction of the incident beam; otherwise, even if the numerical aperture is small, the lens would couple the field components one with the other. If the said conditions are met, then the complex transformation of an incident beam due to the lens is given by:

$$\begin{aligned} \vec{\mathcal{E}}\,'(x',y';z_{\mathrm{out}}) &= \vec{\mathcal{E}}(x,y;z_{\mathrm{in}})v_{\mathrm{cl}}(x,y)\,\mathrm{e}^{j\phi(x,y)} \\ \phi(x,y) &= \frac{2\pi}{\lambda}\left(\Delta_{\mathrm{out}}(x,y)\,n_{\mathrm{out}} + \Delta_{\mathrm{in}}(x,y)n_{\mathrm{lens}}\right) \end{aligned} \tag{2.31}$$

where n_{out} is the refractive index of the medium outside the lens and $\Delta(x,y)_{\mathrm{out/in}}$ is the length traveled by the incident beam in the outer/inner medium along its propagation direction (Fig. 2.6). It is evident that the lens modifies the phase depending on its geometry and material, changing the shape of the beam. In general, the phase added by the lens cannot be described by a universal formula more explicit than the one in Eq. 2.31, but the procedure to compute it is quite general. For the sake of simplicity, the procedure is now shown for the simple case of a spherical lens. Considering the lens depicted in Fig. 2.6, the points belonging to the input and output curved surface must satisfy the condition $R_{\mathrm{i}}^2 = x^2+y^2+z^2$ with $i \in \{1,2\}$ and $x^2+y^2 \leq D^2/4$, being D the diameter of the lens clear aperture involved in the clipping function $v_{\mathrm{cl}}(x,y)$ in Eq. 2.31. The distance between the lens input/output plane, which is the plane tangent to the lens input/output surface in $(x,y) = (0,0)$ and perpendicular to the lens optical axis, is expressed as $R_{\mathrm{i}} - \xi_{\mathrm{i}}(x,y)$, where $\xi_{\mathrm{i}}(x,y) = \sqrt{R_{\mathrm{i}}^2 - x^2 - y^2}$. So It is clear that:

$$\begin{aligned} \Delta_{\mathrm{out}}(x,y) &= R_1 - \xi_1(x,y) + R_2 - \xi_2(x,y) \\ \Delta_{\mathrm{in}}(x,y) &= T_{\mathrm{c}} + T_0 - \xi_1(x,y) - \xi_2(x,y) \end{aligned} \tag{2.32}$$

From an operative point of view, the lens phase function poses two problems: a parameter problem and an aliasing problem. The parameter problem consists in the large number of parameters $(R_{\mathrm{i}}, T_0, T_{\mathrm{c}}, \ldots)$ needed to correctly express the lens phase function. While for simple lenses these parameters are usually provided by the constructor, for most specialized lenses, such as aspheric lenses, the only parameters actually known are the lens focal length and thickness. In this case, the lens phase function may be expressed in a simplified form as [45, 41]

$$\phi(x,y) = -\frac{2\pi}{\lambda}\frac{x^2+y^2}{2\,f} \tag{2.33}$$

where the focal length f encodes all the information related to the lens radii of curvature, refractive indexes and thickness. The aliasing problem, instead, is related to the fact that $\mathrm{e}^{j\phi(x,y)}$ is a chirped function. The sampling interval in real space must satisfy a condition analogous to the one expressed in Eq. 2.2.1, except that a portion of the incident field cannot be set to zero in this case. In fact, while in the BLAS approach the zeroed spatial frequencies cannot physically propagate to the target plane, in the lens case there is no physical reason for zeroing the electric field in the points where the lens transfer function is poorly sampled; so, the only solution is to decrease the spatial sampling intervals $\Delta_\mathrm{x}, \Delta_\mathrm{y}$. This may lead to an unavoidable increase of the required number of sampling points and thus of the computational burden.

2.2.2 WOF validation

In order to asses the accuracy of the NUADAS, detailed in subsection 2.2.1, the results have been compared against a set of numerical benchmark and experimental validations. In particular, the numerical accuracy of the NUADAS has been estimated by computing the Signal-to-Noise Ratio (SNR) with respect to the field evaluated by the direct (and inefficient) computation of the inverse Fourier transform of the propagated spectrum in Eq. 2.14 for different conditions of propagation distance and tilting angle. In formula, the SNR is defined as

$$SNR = -10log_{10}\frac{\int_\mathrm{A}|E_\mathrm{NUADAS}(x,y,z)-E_\mathrm{direct}(x,y,z)|^2}{\int_\mathrm{A}|E_\mathrm{direct}(x,y,z)|^2} \tag{2.34}$$

The result is reported in Fig. 2.7, Fig. 2.8, and Fig. 2.9; as it can be seen, the SNR is positive and very large, indicating that the NUADAS method is accurate and reliable, opening thus for its use in the simulation of optical systems.

As for the use of the thin lens approximation in the WOF, a further numerical validation has been conducted against a simulation done with the commercial software TracePro [61], which is based on the geometrical optics framework and is among the most used tools for the design and simulation of optical systems. The simulated setup consists of a collimated Gaussian beam having a beam waist of 150 µm focused by a commercial plano-convex lens from Thorlabs [62] (Thorlabs

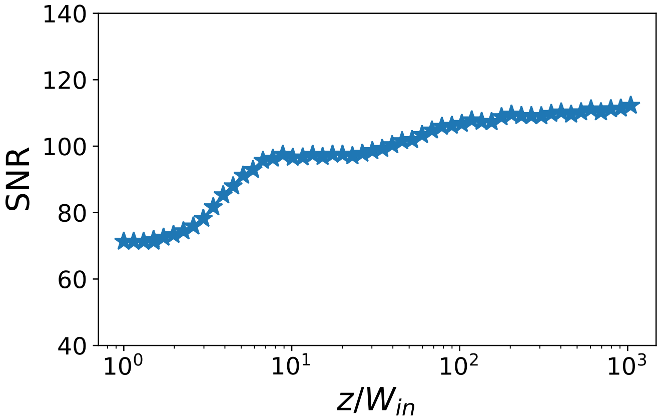

Figure 2.7: Signal to noise ratio as function of the propagation distance, normalized to the computational window size, with $\theta_\mathrm{x} = \theta_\mathrm{y} = \theta_\mathrm{z} = 0$, where θ_i is the rotation angle about the $i-th$ axis in the reference frame depicted in Fig. 2.5.

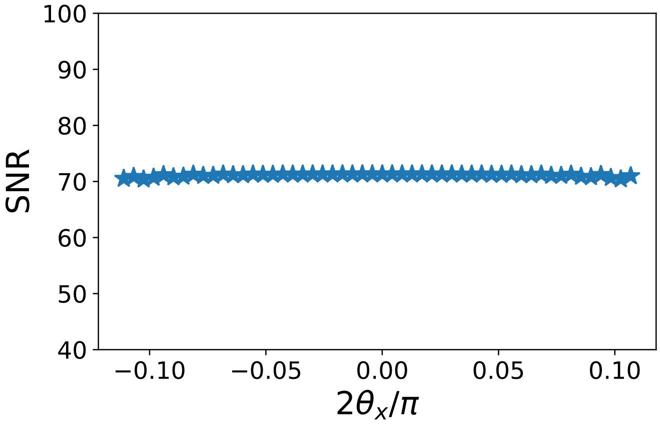

Figure 2.8: Signal to noise ratio as function of θ_x, normalized to $\frac{\pi}{2}$, with $\theta_\mathrm{y} = \theta_\mathrm{z} = 0$ and $d_\mathrm{z} = W$, where d_z is the propagation distance along the z axis, W is the initial computational windows size, and θ_i has the meaning defined in Fig. 2.7.

code: LA1540-AB) placed at a distance of 12.5 mm from the source. This lens has a diameter of 12.7 mm, a radius of curvature of 7.7 mm, and a nominal focal length of 15 mm. It has to be noted that the focal length is the distance between the principal plane, which lies somewhere within the lens, and the principal point [63]. In a practical case, the principal plane position is not known, making the focal length an almost useless information. For this reason manufacturers indicate also the back focal length, which is the distance of the principal point from the back end of the lens. In the considered case the back focal length is 11.6 mm measured from the lens flat surface. Using an iterative approach and the WOF, a measure

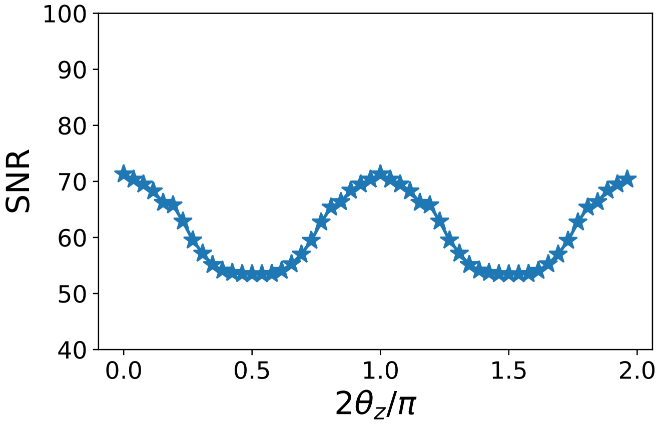

Figure 2.9: Signal to noise ratio as function of θ_z, normalized to $\frac{\pi}{2}$, with $\theta_\mathrm{x} = \theta_\mathrm{y} = 0$ and $d_\mathrm{z} = W$, where all the symbols have the meaning defined in Fig. 2.8.

of the focal length of the lens has been computed as the distance between the lens output plane and the plane where the beam size is smaller. The same procedure has been repeated using TracePro. The two estimated values are reported together with the nominal value provided by the manufacturer in Tab. 2.1, which shows the excellent agreement between the proposed WOF and the commercial software.

Table 2.1: Computed focal lengths for the considered validation example.

WOF	**TracePro**	**Thorlabs**
11.683 mm	11.6 mm	11.6 mm

Given the good indications provided by the numerical simulation tests, the NUADAS method has also been validated against experimental results to asses its applicability in practical cases and its accuracy in non ideal conditions. The setup consists of a camera and a laser beam that can be tilted and translated with respect to the camera normal. Tests with different laser sources available in the lab have been conducted: here, as an example, the results obtained with a 450 nm diode chip, emitting a collimated elliptical beam, mounted on a movement that allows translations in the x and z directions and rotations around the z axis, with the y direction being the propagation direction, are reported. The translation stages have a resolution of 10 µm, while that of the rotation stage is of 0.15°. The camera is based on a high resolution CMOS sensor with a sensitive area of 11.34 mm × 7.13 mm and with 1936 × 1216 pixels. Considering that a pixel to pixel comparison would be of little use due to the acquisition noise, the experimental validation has been done by comparing the measure of the centroid $(\bar{x}_\mathrm{c}, \bar{y}_\mathrm{c})^T = \vec{r}_\mathrm{c}$ of the image taken by the camera with the centroid computed from the simulations. The centroid of the camera is defined as:

$$\begin{aligned} Z &= \int_{\mathrm{CW}} \mathrm{d}x\,\mathrm{d}y\,||g(x,y)||^2, \\ \vec{r}_\mathrm{c} &= \frac{1}{Z}\int_{\mathrm{CW}} \mathrm{d}x\,\mathrm{d}y\,\vec{r}\,||g(x,y)||^2 \end{aligned} \tag{2.35}$$

where CW is the computational window that coincide with the size the camera active area. The differences found between the experimental data and the predictions are very small and easily explained as due to experimental and systematic errors, as it is clear from the results reported in Fig. 2.10 and in Fig. 2.11, where, as an example, the error in the x component of the image centroid is shown for translations of the source along the x axis and for rotations around the z axis, respectively.

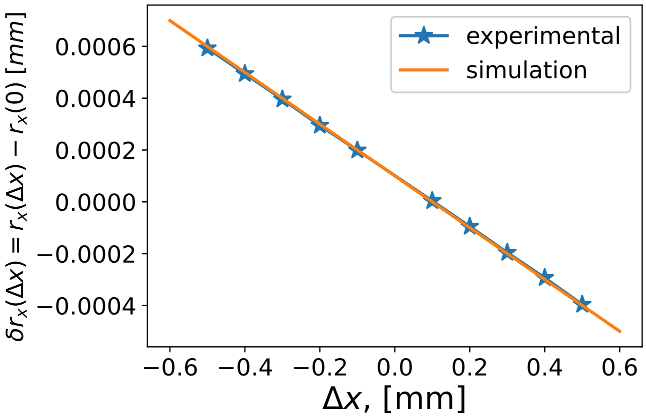

Figure 2.10: Error in the x component of the image centroid for source translations along the x axis. In this case the y axis is taken as the propagation direction.

2.2.3 Numerical analysis of tiled aperture A-CBC architecture

Given the excellent results of the validation in Sect. 2.2.2, the WOF has been used to numerically study the performance of the tiled aperture A-CBC technique. Referring to Fig. 2.3, the tiled aperture A-CBC involves focusing N laser beams incident on the focusing system, which in the simplest case reduces to a single focusing lens, resulting in a combined beam whose peak intensity scales as N^2; therefore, the brilliance of the system increases by a factor N with respect to incoherent beam combining techniques. The brilliance or brightness of a laser is

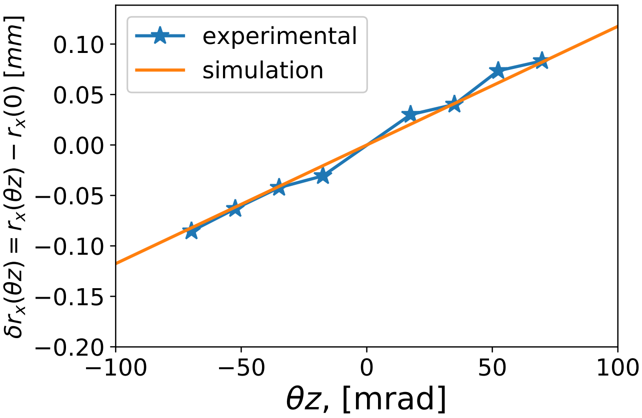

Figure 2.11: Error in the x component of the image centroid for source rotations around the z axis. In this case the y axis is taken as the propagation direction.

defined as

$$B = \frac{P}{\pi^2 w_0 \theta} \tag{2.36}$$

where P is the optical power carried by the laser, w_0 is the beam radius and θ is the beam divergence. As already seen in subsection 2.1, the actual CBC efficiency does not scale just as N^2 since the center to center spacing between the beams is a key parameter in determining the number and intensity of secondary peaks even in absence of phase noise. It is clear that the center to center spacing, and in general the fiber array geometry, has an important impact on the A-CBC architecture efficiency. Moreover, so far, it has strongly been underlined that the phase difference between the combined beam must be accurately controlled but the controlling mechanism has not been discussed yet nor its stability with respect to external and intrinsic perturbations evaluated.

The phase difference between the combined beams can have two origins: it can derive from intrinsic phase oscillations of the sources or from mechanical perturbations that affect the position and orientation of both the beams and the optical elements. There are, in fact, three source configurations commonly used in the A-CBC, as displayed in Fig. 2.12. The first configuration typically consists of N independent laser sources and is the most simple. Ideally, any kind of laser source can be used but fiber lasers are preferred since they have an extremely narrow spectrum and so a good phase stability in addition to a very high output power. High power laser diodes, on the contrary, have a much wider spectrum and, moreover, are limited to a maximum power of few tens of watts. This source configuration is characterized by an implementation simplicity, although at the cost of strong and unpredictable phase modulations. The second source configuration, instead, is

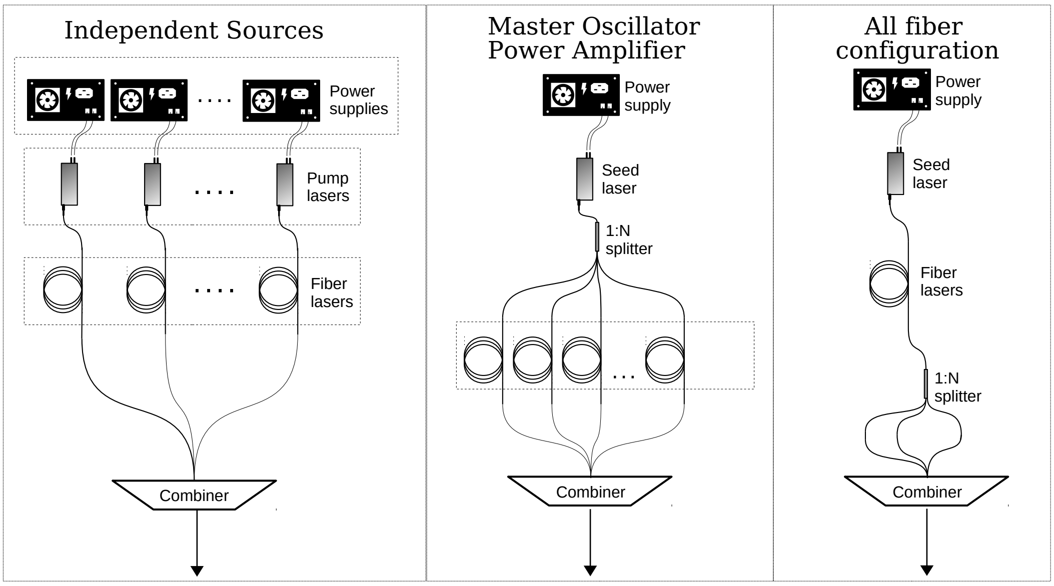

Figure 2.12: Configuration schemes most used in CBC.

based on the use of optical amplifiers and is called Master Oscillator Power Amplifier (MOPA) [64, 65, 66]. A laser seed, which is typically a high power laser diode, is split in N branches that are independently amplified by fiber amplifiers. The amplified beams are then arranged in an array and again coherently combined. The advantage of the MOPA configuration consists in the common laser seed that should guarantee an enhanced phase stability. Ideally, this would lead to zero intrinsic phase perturbations; however the unavoidable small differences in the amplifiers will introduce a non zero phase difference among the combined beams. Anyway, these intrinsic phase perturbations should be almost stationary, resulting in a reduction of the combining difficulty. The third source configuration is an all-fiber configuration in which a single high power source – the seed laser, typically a fiber laser – is first split in N branches using a 1 to N fiber optic splitter; then the N branches are coherently combined together [67]. With this configuration, the resulting beam shows an output power at most equal to the laser seed output power, but the brilliance increases as N^2. Ideally, in this configuration there should not be any intrinsic phase perturbation at all thanks to the passive nature of the splitting mechanism; however, in reality, any small differences between one branch and the others may induce small quasi-stationary intrinsic phase perturbations affecting the CBC efficiency, so the combining difficulty is comparable to the MOPA one. The actual differences between the all-fiber and the MOPA configuration consist in the complexity of the setup. In fact, in the all-fiber configuration the number of branches the seed laser can be split into is typically limited to few tens, resulting in a limited setup complexity and cost. In the MOPA configuration, on the contrary, the number of combined beam is typically of the order of several tens to hundreds, with a consequent increase of the setup complexity and cost, considering that each branch must be independently amplified with a possible increase of phase noise due to the amplifiers difference, as explained above. It is also true, however, that an all-fiber configuration involving hundred of branches has been reported, using an amplification stage shared by all branches [68]. From an implementation point of view the complexity of this setup is probably larger than an equivalent MOPA configuration due to the use of custom components. Independently from the source configuration, the mechanical perturbations of the system, namely mechanical vibrations and perturbations in the optical elements position, cause perturbations in the combined beam phases at the combining element input. These mechanical phase perturbations are principally responsible for the combined beam positioning and orientation errors with respect to the combining system optical axis.

Customarily, PiezoElectric Stages (PES) are used to correct positioning and tilting error and ElectroOptic Modulators (EOM) are used for the beams phase correction. Intuitively, the simplest way to drive the PESs and OEMs would consist in measuring the phase difference of one beam with respect to the others and according to it update the PESs and OEMs driving signal. However, this is not a simple task, especially when it comes to lasers, as it generally requires to have a reference beam and acquire N relative phases. A much simpler approach is based on the SPGD. In fact, by exploiting that the brightness of the beam resulting by the A-CBC increases as the phase difference among the lasers decreases, the PES and OEM driving signal can be updated without the explicit information about the beam phases. As shown in Fig. 2.1, a control station measures, by means of fast photodiode, the A-CBC resulting beam density of power per unit of surface, which is proportional to the brightness, and consequently updates the driving signal of the PESs and EOMs. The conversion of the measured intensity into the driving signal is made using the SPGD algorithm.

The SPGD belongs to a class of optimization algorithms known as gradient descend methods, which are model-free algorithms not requiring a-priori knowledge of the problem to be optimized, but only the possibility to evaluate a user specified target function. In general, a gradient descend algorithm follows an extremely simple principle: if a function $f(\vec{x}) \in \mathcal{R}$ of variable $\vec{x} \in \mathcal{R}^M$ is differentiable and smooth in the neighborhood of a point $\vec{x}\,'$, then starting from $\vec{x}\,'$, it will surely decrease moving along the direction $-\vec{\nabla} f(\vec{x}\,')$ [69]. It follows that

$$\vec{x}\,'' = \vec{x}\,' - \alpha \frac{\vec{\nabla} f(\vec{x}\,')}{|\vec{\nabla} f(\vec{x}\,')|} \Rightarrow f(\vec{x}\,'') < f(\vec{x}\,') \tag{2.37}$$

being α the distance between $\vec{x}\,'$ and $\vec{x}\,''$. The classical method of the steepest descend uses Eq. 2.37 to iteratively update the value of $\vec{x}$ until a convergence criterion is met. This criterion usually depends on the problem; however, the simplest one is satisfied if $|\vec{x}'' - \vec{x}'| < \epsilon$, where ϵ is a tolerance value chosen by the user. The steepest descend algorithm is guaranteed to converge to the global minimum if $f(\vec{x})$ is concave and smooth, otherwise it will surely converge, at least, to a local minimum of f. The rate of convergence strongly depends on the value of α, and may be quite small if α is badly chosen; however, there is not a general rule that allows choosing the optimal value of α. Nevertheless, the main advantage of this class of algorithms lies in their ability to minimize a function with respect to a set of variable even without being explicitly defined. Indeed, the gradient of the function can be numerically evaluated as

$$\vec{\nabla} f(\vec{x}) \simeq \frac{f(\vec{x} + \vec{\delta x}) - f(\vec{x} - \vec{\delta x})}{2} \vec{\delta x}^{-1} = \frac{\delta f}{2} \vec{\delta x}^{-1} \tag{2.38}$$

where $\delta x_{\mathrm{i}}^{-1} = \dfrac{1}{\delta x_{\mathrm{i}}}$. The gradient descend updating equation can finally be expressed as

$$\vec{x}^{\,k+1} = \vec{x}^{\,k} - \alpha \vec{\nabla} f(\vec{x}) = \vec{x}^{\,k} - \alpha \frac{\delta f_{\mathrm{k}}}{2} \vec{\delta x}^{-1} + \mathcal{O}(|\vec{\delta x}|^4) \tag{2.39}$$

with $\vec{x}^{\,0}$ an initial starting point that can be chosen arbitrarily and δf_{k} the estimation of the gradient in $\vec{x}^{\,k}$ as in Eq. 2.38. It is evident that the only constraint on the target function is that it has to be at least a black box such that, for a given set of input, it gives back a scalar value. For instance, the target function can even be a measured quantity in an experimental setup. However, if the measured target function is affected by some noise, which is unavoidable in an experimental setup, then this noise influences the determination of the steepest descend direction. The SPGD is formulated in order to overcome this problem by adding a bit of stochasticity to the classical gradient descend method. Indeed, letting each entry of the increment vector be a random number, distributed according to a probability density function having zero mean and an appropriate variance σ, and the increments be uncorrelated one with the others

$$\begin{gathered} \delta \tilde{x}_{\mathrm{i}} \sim p(x; \mu, \sigma) \\ \langle \delta \tilde{x}_{\mathrm{i}} \rangle = 0,\ \langle \delta \tilde{x}_{\mathrm{i}}\, \delta \tilde{x}_{\mathrm{j}} \rangle = \delta_{\mathrm{i,j}}\, \sigma^2 \\ \vec{\delta \tilde{x}} = \{\delta \tilde{x}_1, \delta \tilde{x}_2, ..., \delta \tilde{x}_{\mathrm{N}}\} \end{gathered}$$

it may be proven that substituting the updating rule in Eq. 2.39 with the following updating rule

$$\begin{gathered} \delta \tilde{f}_{\mathrm{k}} = \frac{f(\vec{x}_{\mathrm{k}} + \vec{\delta \tilde{x}}) - f(\vec{x}_{\mathrm{k}} - \vec{\delta \tilde{x}})}{f(\vec{x}_{\mathrm{k}} + \vec{\delta \tilde{x}}) + f(\vec{x}_{\mathrm{k}} - \vec{\delta \tilde{x}})} \\ \vec{x}^{\,k+1} = \vec{x}^{\,k} - \alpha \delta \tilde{f}_{\mathrm{k}}\, \vec{\delta \tilde{x}} \end{gathered} \tag{2.40}$$

which is the SPGD updating rule, leads to an average minimization of the target function, characterized by a convergence rate in the order of $\sqrt{N}$, especially if N

is large [70]. Finally, with reference to Fig. 2.1, to apply the SPGD to the A-CBC approach, it is enough to substitute the variable $\vec{x}$ with the OEM and PES driving signals

$$\vec{x} \rightarrow \vec{V} = \{V_1, V_2, ..., V_\mathrm{N}\}$$
$$\vec{\delta x} \rightarrow \vec{\delta V} = \{\delta V_1, \delta V_2, ..., \delta V_\mathrm{N}\}$$

and to define the target function as the average negative density of power of the resulting beam B_k, which is proportional to the current flowing in the monitor photodiode I_k^{pd} at k-th iteration

$$B_\mathrm{k}\left(\vec{V}^k\right) = -\frac{1}{A}\int_A I_\mathrm{k}^{CBC}\left(x, y; \vec{V}^k\right) \mathrm{d}x\,\mathrm{d}y = -\beta\, I_\mathrm{k}^{pd}\left(\vec{V}^k\right) \tag{2.41}$$

where A is the CBC resulting beam desired spotsize, I_k^{CBC} is the CBC resulting beam intensity at k-th iteration and β is a proportionality constant depending on the experimental setup. All in all, the SPGD updating rule applied to the A-CBC technique is

$$\vec{V}^{k+1} = \vec{V}^k - \alpha_\mathrm{k}\delta B_\mathrm{k}\,\vec{\delta V} \tag{2.42}$$

In the updating rule in Eq. 2.42, the updating step size has a subscript k since, in general, it can be dynamically updated too with the intent of increasing the convergence rate of the optimizer [71]. In the remaining of this section, the learning rate will be assumed to be stationary in order to analyze the performances of the SPGD using WOF-based numerical simulation due to the fact that usually the SPGD is not combined with adaptive updating of the step size (although it is true that in recent works the SPGD has been combined with adaptive step size strategies showing better performances than the SPGD alone [72]).

The analysis of the SPGD applied to the A-CBC stability with respect to various conditions of intrinsic and mechanical noise has been performed simulating the beam combination in the WOF detailed in Sect.2.2.1. The simulated setup consists of two gaussian beams, ideally generated by two fiber lasers, characterized by a collimated spot size w_0 of 250 µm, a wavelength of 900 nm and a total power of 1 W. The two beams are combined by a focusing lens having a focal length of 60 mm. The chosen laser wavelength here doesn't play much of a role in the following analysis; however is it worth noting that commercially available, off-the-shelves fiber lasers used in industrial processes emit at a wavelength around 1064 nm. A first set of simulations has been performed in static noiseless condition in order to understand the impact of both the array geometry and of the Optical Path Difference (OPD) – the difference in the length of the optical path experienced by the two sources – on the A-CBC performances.

First of all, it is worth noting the good agreement between the analytical model and the numerical simulation, as shown in Fig. 2.15. The CBC efficiency, defined in Eq. 2.1, is used as the metric to evaluate the performances of the A-CBC as shown in Fig. 2.13. Fig. 2.14 reports the variation of the maximum density of power per

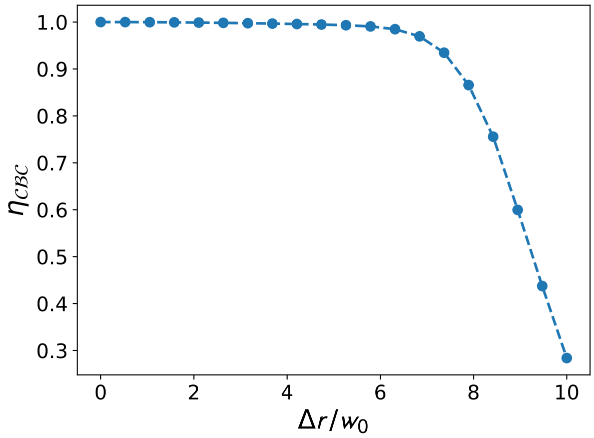

Figure 2.13: Coherent beam combining efficiency as function of center to center distance Δr normalized to the collimated beam spotsize w_0.

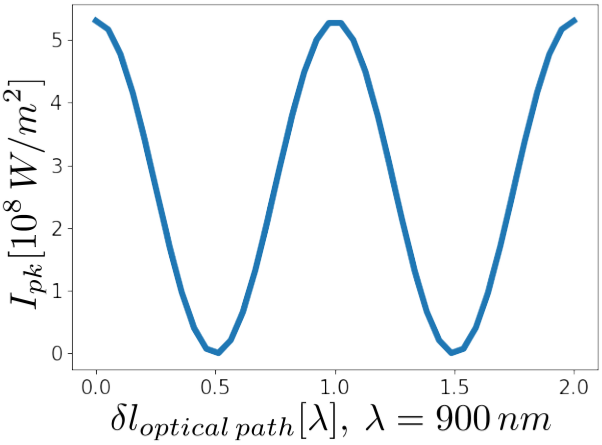

Figure 2.14: Peak intensity of the A-CBC resulting beam as function of optical path difference $\delta l_{\text{optical path}}$ normalized to the beam wavelength λ.

unit of surface. It is clear, from the data shown in Fig. 2.13, not only how strongly the A-CBC efficiency may change with respect to the array geometry, a behavior somehow already predicted by the analytical model detailed in Sect. 2.1, but also that a center to center distance (Δr) of more that five times the beam size may drastically decrease the A-CBC efficiency for a given lens focal length. Typically, for a fiber laser emitting at 1064 nm, the output fiber has a total diameter of the order of half a millimeter, allowing for a minimum Δr of about 0.5 mm. Assuming

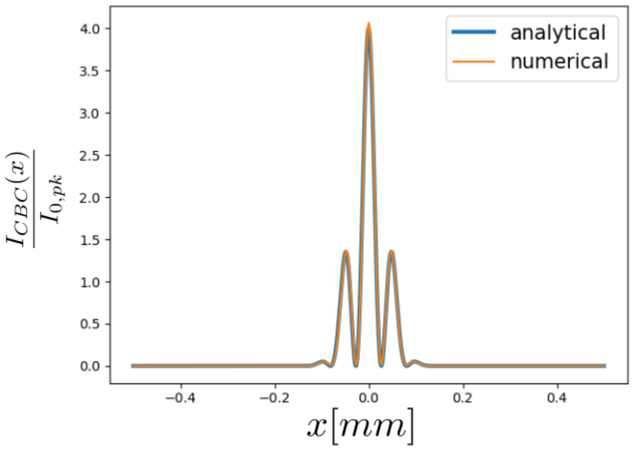

Figure 2.15: A-CBC intensity predicted by the analytical model compared to the A-CBC intensity computed numerically in the WOF. Both intensities are normalized with respect to the peak intensity of a single combined beam.

that the collimated beam spot size w_0 is about 250 µm and considering that the typical Δr cannot decrease compared to the previous one due to the use of optical and mechanical elements, the center to center distance is already between $3w_0$ and $4w_0$, resulting in a beam positioning displacement tolerance of at most 0.5 mm to keep an optimal A-CBC efficiency. Accordingly, any perturbation increasing Δr of more than 0.5 mm affects the CBC efficiency and needs to be corrected in real time. On the other hand, from Fig. 2.14 it is quite evident that the A-CBC efficiency is extremely sensible to optical path differences in the order of the wavelength itself, which requires a dynamic position correction at the sub-wavelength scale. It is well known that EOMs and PESs provide, respectively, phase and positioning correction with the desired precision; however, the timing of the correction is given by the SPGD algorithm. The SPGD algorithm effectiveness is indeed subject to two kind of limitations when driving the PESs and EOMs. The first one is hardware related and consists in the time needed by the algorithm itself to process the feedback signal and update the driving signals, hence to the hardware working frequency. If its working frequency is not large enough compared to the rate of change of the quantity to be compensated (a mechanical displacement of some elements or some sources phase noise), then the CBC efficiency would hardly reach a value close to one. The second one, instead, is related to the amount of time needed by the algorithm to reach the convergence, which is related to the number of devices that the algorithm controls. The convergence of the SPGD under different dynamical noise conditions can be studied exploiting once again the simulation tools detailed in Sect. 2.2. As in the previous case, the simulated setup consists of two collimated Gaussian laser beams characterized by a spot size of 250 µm and a wavelength equal to 900 nm combined by plano-convex lens having a focal length of 60 mm. Even if the mechanical perturbation on the beam positioning may severely affect the CBC efficiency, these perturbations, due to their mechanical nature, have a rate of change way slower than the intrinsic phase perturbations; therefore, the center to center distance between the two beams is considered here fixed and equal to w_0. The phase difference between the two beams is modeled as the sum of two contributions, the Optical Path Difference (OPD) and the Temporal Phase Mismatch (TPD). The OPD is the difference between the propagation distances travelled by each beam to reach the target plane. Even small vibrations in the setup inducing a displacement of the optical elements from their ideal positions of the order of λ can affect the combining efficiency. Therefore the OPD is modeled by δl_{OPD}, a random variable distributed according to a uniform distribution between 0 and the wavelength λ causing a phase difference between 0 and 2π

$$\delta l_{\mathrm{OPD}} \sim U_{[0,\lambda]} \tag{2.43}$$

The OPD is considered as an instantaneous perturbation that affects, at each cycle, the CBC efficiency. The second contribution is due to some TPM intrinsic to the sources. The TPM represents stochastic phase jumps occurring every now and then. The interval between one TPM and the next one is modeled as a sequence of independent random variable extracted according to an exponential probability density function

$$\Delta t \sim \frac{1}{\tau}\,\mathrm{e}^{-\frac{\Delta t}{\tau}} \tag{2.44}$$

customarily used to model stochastic waiting times [73]. The intensity of the phase jumps are instead modeled as a random variable uniformly distributed in the interval $[0, \nu 2\pi]$.

$$\delta\phi_{\mathrm{TPM}} \sim U_{[0,\nu 2\pi]} \tag{2.45}$$

$\nu \in [0,1]$. The behavior of the CBC efficiency in closed loop, namely under the correction operated by the SPGD operating at a given frequency f_{SPGD}, is shown in Fig. 2.16, in Fig. 2.17 and in Fig. 2.18. Since in the simulations the time is scaled by the SPGD working frequency f_{SPGD}, the TPM parameter τ, which determines how often the TPM occurs, is expressed in terms of f_{SPGD} too.

Fig. 2.16 shows the CBC efficiency under constant OPD condition ($\alpha = 0.1$) and two quite different and illustrative TPM conditions: the plot on the left reports the CBC efficiency subject to a quite strong TPM, which on average occurs with a frequency twice as large as the SPGD working frequency ($\tau = 2$) with an intensity randomly distributed between 0 and $0.2\,\pi$ ($\nu = 0.1$); the plot on the right reports the same system under a TPM characterized by phase jumps ten times smaller

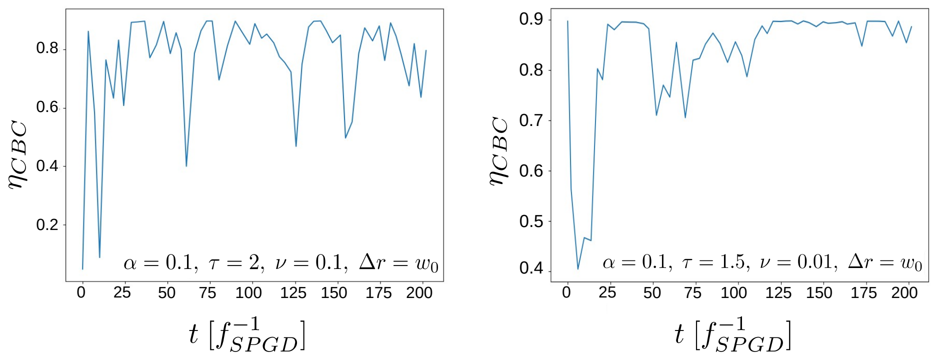

Figure 2.16: CBC efficiency as function of time in SPGD closed loop regime under two different TPM conditions.

($\nu = 0.01$), but a little more frequent ($\tau = 1.5$) than in the previous case. It is evident that, despite a quite frequently occurrence of TPMs, on average the efficiency is large enough in both cases, rising from about 0.8 to about 0.9 as the intensity of the TPMs decreases. In addition, also the standard deviation of the efficiency decreases as the TPM intensity decreases.

A similar behavior for the CBC efficiency in closed loop for constant TPM conditions, but variable OPD is shown in Fig. 2.17. Indeed, on average the CBC efficiency increases as α, which characterize how large the OPD is between the combined beams, decreases.

Fig. 2.18 shows the performances of the SPGD given a completely random initial phase difference and with different center to center distance values in a noiseless condition. Clearly, the SPGD can indeed reach the optimal CBC efficiency independently of the initial condition in very few steps, a result that may be further improved using the adaptive updating steps already discussed. This allows setting the minimum SPGD working frequency equal to a value one order of magnitude larger the average phase perturbation frequency if a constant updating step is used.

These results can be explained considering that the SPGD is an iterative optimizer and not a predictive one. In fact, it is not able to predict when the next phase jump will occur and how strong it will be; it only updates the driving signals once the jump has occurred and it will take a variable number of iterations to maximize the target function again. Therefore, if the phase jumps are too large and occur too frequently between one SPGD iteration and the next one, the SPGD will not actually have enough time to maximize the efficiency and will always remain a step behind the phase variations. Conversely, if the phase jumps are very weak but way more frequent than the SPGD updates, then the net effect will be a small constant phase shift that the SPGD can efficiently compensate. Finally, another parameter that must be taken into account is the the number of devices

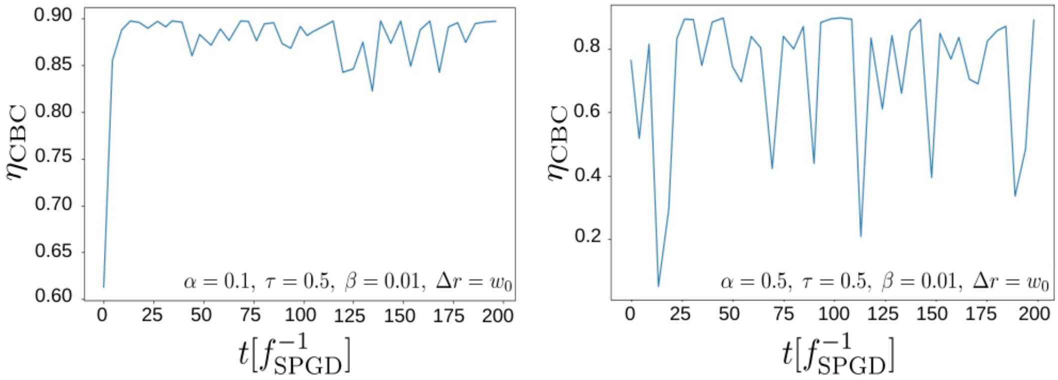

Figure 2.17: CBC efficiency as function of time in SPGD closed loop regime under different OPD conditions.

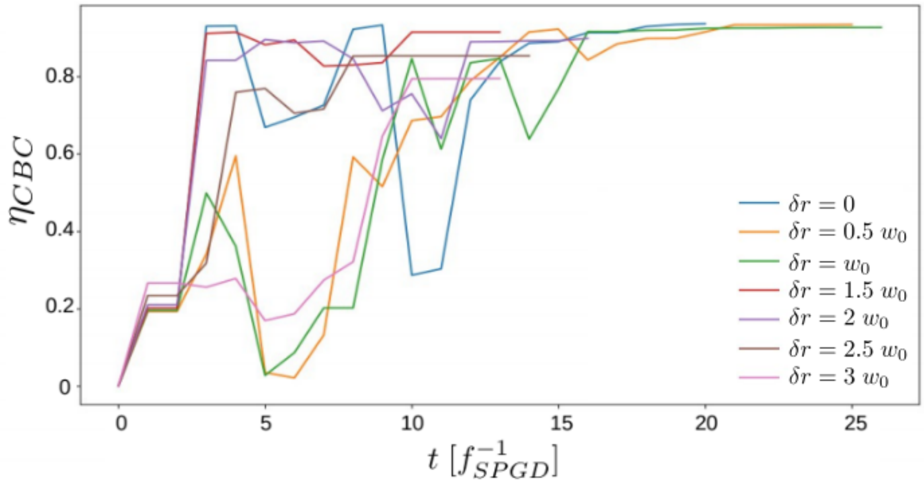

Figure 2.18: CBC efficiency as function of time in SPGD closed loop regime with several initial center to center distance δr normalized to the collimated beam spot size.

that the SPGD controls. Indeed, as the number of driven devices increases, the dimensionality of the space the target function lives in increases as well, leading to the so called curse of dimensionality: as the dimensionality of the target function increases, the SPGD latency in restoring the CBC efficiency increases exponentially. As a matter of fact, this is the main problem of the SPGD, which severely limits the number of beams that can be coherently combined. It is true that the use of specialized hardware, such as Field Programmable Gate Arrays (FPGAs), can ease this problem; however, this approach too is quickly reaching its limit. This is the reason why, in the following section, a new strategy based on the use of neural networks is proposed and its feasibility is numerically analyzed.

2.3 Neural Network assisted coherent beam combining

As pointed out in the previous section, the main limitation of the A-CBC in scaling up the number of combined beams consists in the SPGD latency: as the number of devices to be controlled increases, the dimensionality of the space the target function lives in increases as well, leading to an exponential increase of the time needed by the SPGD to maximize the target function. A first approach to overcome this problem is to increases the SPGD working frequency as much as possible using, for instance, specialized hardware such as FPGA. A less brute-force-like approach consists in the use of an adaptive updating steps α_{k}, which has already extensively proven to be a game changing approach in the field of deep learning. Both approaches are valid, still none of them tackle the problem at its root, which is the number of devices that the SPGD must drive. It has already been mentioned that the phase perturbations may be external, in which case it is principally due to mechanical noise, or intrinsic to to the source. In the case of mechanical noise, it is reasonable to expect that its frequency spectrum has a larger intensity at lower frequencies and that it decreases as the frequency increases. Moreover, in the previous section, it has been discussed that a phase noise characterized by frequencies larger than f_{SPGD} and small amplitude is perceived by the SPGD only as slow net phase perturbation on a time scale in the order of f_{SPGD}^{-1}. On the contrary, these considerations cannot be done for the intrinsic phase noise. Hence, it is evident that the SPGD, working at quite large frequency, is overpowered when it comes to drive the PESs, whose driving signal may be updated way less frequently.

Indeed, a better strategy consist in the use of the SPGD to drive only the OEMs while having a different algorithm controlling in parallel the PESs, thus reducing the number of devices controlled by the SPGD with a consequent decrease in latency and improvement in the CBC performances. The main idea here is to correct the errors due to mechanical perturbations in real time using an Artificial Neural

Network (ANN) to predict the deviation of a beam from its ideal alignment. ANNs have already been used to assist in the assembly of the collimating optical elements inside multi-emitter laser modules [74]: in that case an ANN is exploited to extract some parameters defining the tilts and shifts of a lens from the analysis of beam images. In this work a similar approach is extended to find the correction commands for the displacement stages to counteract the mechanical perturbations from the analysis of just two beam images. In particular, the developed correction method exploits a Fully Connected Artificial Neural Network (FCANN) [75, 76] that takes as input some numerical parameters automatically extracted from the beam images at two different locations and infers from them the beam direction with respect to a given reference system and therefore the correction for the ideal alignment. This allows the piezoelectric stages to correct the beam position in a single step. The process can then be repeated for each beam to be combined by having several FCNNs running in parallel. This way, the proposed approach allows correcting the propagation direction of each beam independently, reducing the number of elements to be controlled by the PSGD algorithm and thus contributing to increase the number of lasers that can be coherently combined. In general, simultaneously extracting the beam shift and tilting with respect to the camera orientation from two images is not a trivial task since this can be formulated as the problem of inverting an unknown function given only some measured values. Fortunately, what it is known as the classical formulation of the Universal Approximation Theorem [77] states that a neural network can approximate any well-behaved function with an accuracy that depends only on the neural network free parameters and the extension of the training dataset. This means that to ensure a low enough error for CBC applications, it is essential to have a very large dataset for training the ANN. As it is practically impossible to have such a large dataset of experimental values, the solution is to train the FCANN using a synthetic dataset built from numerical computations; in turn, this requires the accurate simulation of a laser beam propagation in an arbitrary direction with respect to a given reference frame, a task that can be easily accomplished using the WOF detailed in Sect. 2.2.1. A possible practical implementation of such approach is depicted in Fig. 2.19. The simplest way to control the propagation direction of the beams is to have each of them reflected by a motorized mirror. Each reflected beam then propagates through a couple of polarization insensitive beam splitters, used as beam samplers, aligned along the optical path. The small fraction of the reflected beam is imaged into a high speed and high resolution camera. The two beam splitters for each beam are positioned at a slightly different distance along the propagation direction. A tilted source when imaged into a camera is not very different from a shifted source, especially in ordinary operations for a CBC system in which the shift is in the order of fractions of millimeters and the tilt of few milliradians (see also Fig. 2.21). In these conditions, determining if the source is tilted or shifted, left alone quantifying the tilt or the shift, is extremely difficult. However, this problem can be solved by using two images of the same beam at two distances along the optical path. Intuitively, if the beam is simply shifted, the centroid, at different distances, does not change, while the beam waist changes. If instead the beam is tilted compared to the camera input plane, not only the standard deviation but also the centroid, the kurtosis γ and the skewness κ of the images, defined in Eq. 2.46, change.

$$\begin{aligned}\gamma_{\mathrm{i}} &= \frac{1}{Z}\int_{\mathrm{CW}} \mathrm{d}x\mathrm{d}y\ (r_{\mathrm{i}} - r_{\mathrm{c,i}})^3 ||g(x,y)||^2 \\ \kappa_{\mathrm{i}} &= \frac{1}{Z}\int_{\mathrm{CW}} \mathrm{d}x\mathrm{d}y\ (r_{\mathrm{i}} - r_{\mathrm{c,i}})^4 ||g(x,y)||^2\end{aligned} \tag{2.46}$$

with Z defined in Eq. 2.35. This justifies the need for two beam splitters and two cameras for each beam to be coherently combined.

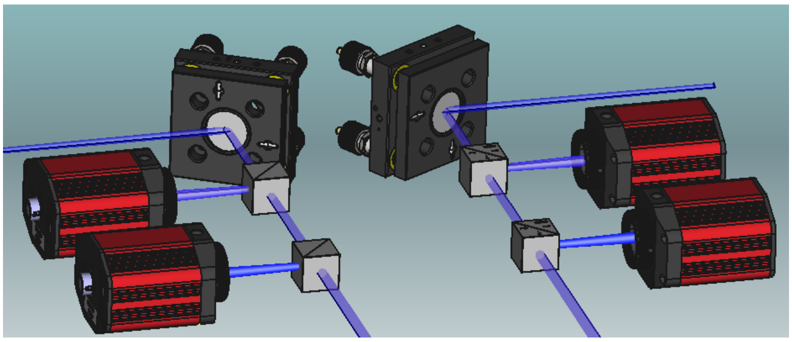

Figure 2.19: A possible implementation of the mechanical perturbation control setup. The blue lines represent the beams, while the red elements are the cameras and the grey blocks in front of the cameras the beam splitters (or samplers); in the back there are mirrors mounted on motorized stages and/or gimbal mounts.

To test the potential of this approach, an FCANN has been trained on a synthetic dataset built using the parallel version of the NUADAS algorithm detailed in previous sections. Considering the available equipment for future experimental implementations, a relatively reduced power version of fiber laser sources has been considered. The dataset has been built simulating the propagation of a tilted and shifted Gaussian beam at 1070 nm with $\sigma_{\mathrm{x}} = 70\,\mu\mathrm{m}$ and $\sigma_{\mathrm{y}} = 100\,\mu\mathrm{m}$ and storing the field centroid, the standard deviation, the kurtosis and the skewness along x and y at a distance of 50 mm and 100 mm. The source tilt has been restricted to rotations around the x and y axis for a random angle in the range −10 mrad to 10 mrad, while the shift has been considered only for x and y (leaving the z shift to be dealt together with phase drifts by an EOM) both randomly selected in the −0.15 mm to 0.15 mm. In total, the built dataset is composed by 160 000 simulations, each of a source randomly shifted and tilted with respect to the target plane; 5% of the dataset has been used as a validation set and the other 95% as a training set. The neural network free parameters are the number of hidden layers, the number of neurons in each hidden layer and the activation function, which is assumed to be the same for all the neurons for simplicity. In general, those parameters are chosen to minimize the neural network error on the validation set; however, for the current application there is another constraint: the neural network speed. Indeed, if used to align the beam in a CBC setup, the neural network response must be faster than the period of beam displacements caused by the mechanical perturbation. This constraint rules out all the most complicate neural network architectures, such as the convolutional one, which are also the most difficult to train, leaving with the used FCANN. Hence, with the goal of a FCANN as simple and fast as possible, and given the excellent agreement between the NUADAS result and the experimental one, it has been chosen a FCANN with only one hidden layer of 8 neurons densely connected with the input made of 16 neurons and the output layer composed of 4 neurons; the input and hidden layer neurons use as activation function the ReLu [78], which has been reported to accelerate the accuracy convergence rate of neural networks avoiding the vanishing gradient problem [79], and the output neurons a linear function. The 16 inputs are centroid, standard deviation, kurtosis and skewness along x and y for both images. The output neurons are the source tilting angle around the x and y axes normalized to 1 mrad and the source shift along the x and y axes normalized to 1 mm.

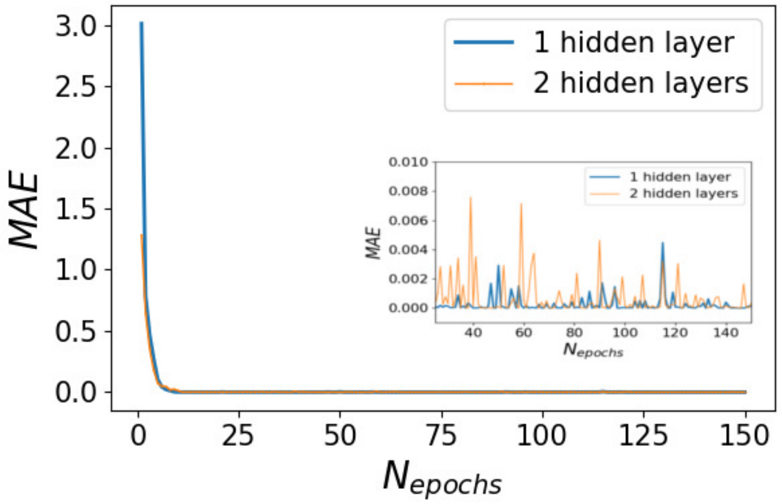

Figure 2.20: Mean absolute error versus the number of training epochs. The blue curves refer to the case of a FCANN composed of only one hidden layer of 8 neurons and the orange curves to the FCANN composed of 2 hidden layers, having 12 and 8 neurons, respectively.

Fig. 2.20 reports the Mean Absolute Error (MAE) versus the number of training epochs for the implemented FCANN. The MAE on the validation dataset is defined as:

$$L_\mathrm{j} = \frac{1}{N_\mathrm{testset}} \sum_{\mathrm{i}=1}^{N_\mathrm{testset}} |y_\mathrm{i} - \bar{y}_\mathrm{i}| \tag{2.47}$$

where L_j is the loss on the validation dataset after the j-th training epoch and $\bar{y}_\mathrm{i}$ is the neural network prediction on the i-th input of the test set. As it can be seen from Fig. 2.20, the FCANN shows excellent performances even if its structure is very simple: indeed, after 150 epoch of training the average MAE is of the order of 5×10^{-4} with a standard deviation of about 7.5×10^{-4}. The FCANN output is a vector whose entries are the shift and angular errors, so, in the worst case, it is a vector having only one entry different from zero. In this case, the FCANN estimation error differs from the actual error of about 1 µm for a shift error along a single direction or 1×10^{-3} rad for an angular error about a single axis. In the present case, the beam needs to be aligned with respect to a combining element, either a focusing lens or a volume holographic grating. In this scenario, a residual angular error corresponds, in first approximation, to an error of the beam position on the combining element that can be estimated as $d \tan \alpha_\mathrm{res}$, where d is the distance between the sources and the combining element and α_res is a residual tilt error of the source. Assuming an already collimated source, the combining element can be placed as close as possible to the source, hence the FCANN estimation error of the angular error is negligible in a practical case. Moreover, as illustrated in Fig. 2.13, the CBC efficiency shows a non negligible decrease only for normalized shift errors greater than two, which is far greater than the FCANN worst case normalized residual error, demonstrating that the neural network prediction are accurate enough to correct the tilting and positioning errors during the CBC process. The execution time on a common high performance laptop is about 1.2 ms, so close to a frequency of 1 kHz on a non specialized hardware. Clearly, the frequency performance can be increased by using a specialized hardware such as an FPGA [80].

In principle, the error could be further reduced by increasing the complexity of the neural network. However, in the considered case, unless a very complex, hence time-consuming, configuration is considered, very little improvements occur. For example, another FCANN with two fully connected hidden layers (16 neurons in the first hidden layer and 8 neurons in the second, all using a ReLu activation function) provided a level of accuracy similar to that of the simpler FCANN (Fig. 2.20), but with almost half the maximum frequency (execution time is 1.6 ms, leading to a frequency of 0.625 kHz), therefore not justifying its use.

Before moving on to the next chapter, it may be useful to briefly recap the work and results presented in this chapter. In the first part of it the CBC as the only viable approach to further increase the output power of current high power laser sources without compromising their beam quality has been introduced. The accurate evaluation of its performance and the identification of the limiting parameters required the development of a method to compute the propagation of a laser beam with a very high accuracy and speed also in presence of tilts and shifts.

This method can be taken as a reference for studying real optical systems and used for simulation aided design, also besides the analysis of CBC. As an example of this application, Fig. 2.21 and Fig. 2.22 show the propagation of a Gaussian beam for two different shift-tilt cases. In Fig. 2.21 the physical space window has size $1024\lambda \times 1024\lambda$, where λ is the wavelength, and the distance between the target planes is 512λ. The source is a Gaussian beam with $\sigma_{\mathrm{x}} = 64\lambda$ and $\sigma_{\mathrm{y}} = 32\lambda$. The source plane is tilted by $\theta_{\mathrm{x}} = -\pi/50$ and $\theta_{\mathrm{z}} = \pi/6$. In Fig. 2.22, the input Gaussian beam is the same as before, but the distance between the target planes is 1024λ and they have a relative tilting of $\pi/10$. In addition, another possible field of application of the NUADAS is the simulation of non linear wave propagation, as in the case of high power laser propagation subject to self-focusing effects. In fact, the joint use of the CZT and the BLAS, which lies at the core of the NUADAS, may be used to increase the numerical accuracy of the split step Fourier method, leading to a decrease of the computation burden and so an increase of the performances of the algorithm. Then, in the second part, an approach to overcome a limitation of the classical CBC implementation has been presented. This approach is based on the analysis of beam images with a FCANN, which required, once more, the use of the developed simulation method for its training. In this case too, the obtained results can find application besides the use in the CBC. Indeed, the FCANN assisted alignment can be used as a substitute for the common active alignment procedures in the assembly of optical elements, for example in the laser diode multi-emitter module assembly, with a substantial reduction of the required time, confirming and extending the results reported in Ref. [74].

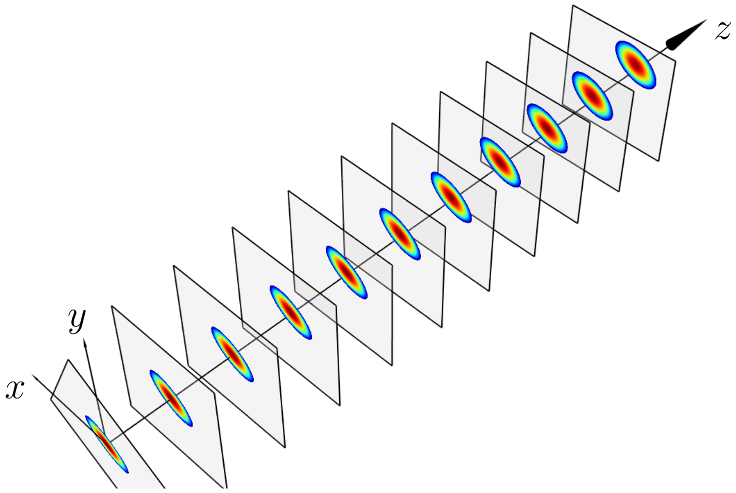

Figure 2.21: Propagation of a Gaussian beam from a tilted source plane to equispaced target planes.

The WOF method can, in future, be further extended to take into account also the interfaces between different dielectrics and used also to simulate misaligned

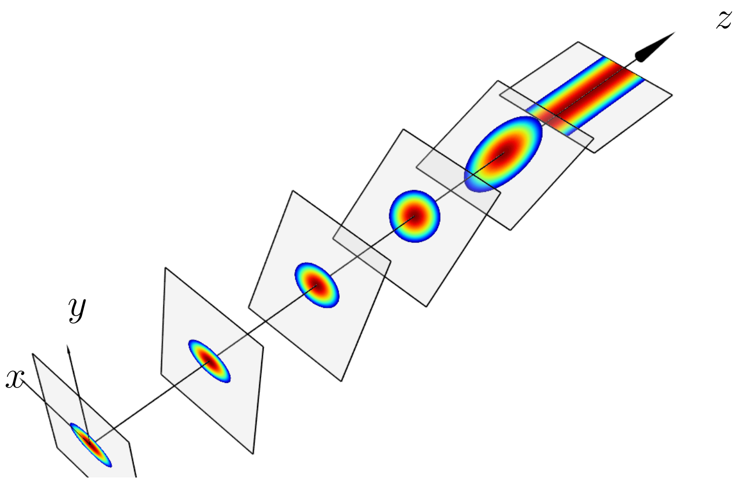

Figure 2.22: Another example of propagation of a Gaussian beam in equispaced and tilted target planes.

lenses or other optical components, as the propagation through an arbitrary tilted and shifted lens can be broken down into three smaller problems: the propagation from the source to the elements input plane, which may be arbitrarily tilted and shifted with respect to the source plane, the propagation through the lens itself and, finally, the propagation from the lens output plane to the target plane, which, with respect to the lens output plane, could also be arbitrarily tilted and shifted. This would allow building accurate datasets for training FCANNs to assist in the automatic assembly of optical devices. Indeed, the alignment of lenses and of other optical elements is well known to be one of the most time consuming steps in the packaging of optoelectronic devices [81, 82]. This is particularly critical when several components have to be aligned, such as in high power multi-emitter laser diode modules, in which, for example, tens of lenses and mirrors have to be accurately positioned with sub-micrometric accuracy [18, 83]. A multi-emitter laser diode module is a device composed of a number of single semiconductor emitters, called chips, whose output beams are combined inside a common package exploiting various multiplexing levels (usually spatial multiplexing first, followed by polarization and/or wavelength multiplexing) implemented with free-space techniques and therefore making use of micro-optics. In most of these modules the combined beams are then focused onto a collecting fiber. Today, the assembly of these devices is typically carried out with automated machines, which make use of active alignment procedures to optimally place the micro-optical components. Active alignment requires turning-on the laser source and then optimizing its coupling by raster scanning the position of the lens (or of the optical component, in general) while continuously monitoring the transmitted power or the beam profile. This is clearly a long process that takes several minutes for each component to be carried out, for an overall assembly time that can easily exceed a couple of hours for the higher power modules since these are composed of about 20 chips, each with its associated set of lenses and mirrors. As these high-power multi-emitter modules are the key component of industrial lasers and their cost accounts for almost 50% of the overall cost of the laser source, it is evident that any improvement in their assembly procedure has a huge economical impact. The use of an artificial neural network to correctly position in a single step the Fast Axis Collimating (FAC) lenses of laser chips has already been proved to be effective in comparison with active alignment procedures [74, 84]. However, in that case the training set was based on simplified Gaussian beam propagation model (the “five-ray approach”) [85, 84] and limitations applied. For instance, it was shown that the ANN is able to infer the shift error and the tilt error about the fast axis direction with an accuracy down to the micrometer; however, in reality, the lens position is affected also by shifts and tilt about the slow axis. To do so, the ANN must be trained on a larger dataset, that would include also these kind of errors, which could not be taken into account by the five rays model previously employed, hence the need of a different, more accurate, numerical method, such as the NUADAS.

Lately, another possible field of application of the NUADAS is in the simulation of non linear wave propagation, as in the case of high power laser propagation subject to self-focusing effects. In fact, the use of the CZT and the BLAS may be used to increase the numerical accuracy of the split step Fourier method, leading to a decrease of the computation burden and so an increase of the performances of the algorithm.

Chapter 3

Spectral stabilization of laser diodes.

As discussed in Ch. 2, the coherent multiplexing approach requires the use of stable, almost monochromatic laser sources with a very low phase noise, such as fiber lasers, to reach the maximum efficiency. In addition, maintaining a constant, close to zero, phase difference among the combined beams, requires complex – thus expensive – configurations, which account for the limited diffusion of coherent beam combining for scaling the output power of laser sources. An alternative approach is the spectral multiplexing, which exploits the combination of several laser beams, each at a different wavelength, into a single beam. The drawback of this approach is the increase of the overall spectral width, which implies a decrease of the spectral power density (the ratio of the beam power to its spectral width); this can or cannot be acceptable depending on the target application. The spectral width of the combination can be minimized by using narrow and spectrally dense beams, although the tolerances in the fabrication of the dichroic mirrors used to combine them pose a limitation on the wavelength separation between two lasers. More details on the spectral multiplexing will be discussed in Ch. 4.

In any case, the main requirement for an efficient spectral multiplexing is to have lasers with outstanding spectral features, both in terms of a spectral width – about 2 nm at 90% of optical power – and of peak wavelength shift with temperature – about $0.01\,\mathrm{nm\,K^{-1}}$. This requirement rules out most of the high power laser diodes because, being based on a multimode Fabry-Perot (FP) cavity, are characterized by a spectral width larger than 5 nm at 90% of power and a peak wavelength shift of about $0.3\,\mathrm{nm\,K^{-1}}$, as shown in the following chapter.

Nevertheless, such lasers can meet the spectral multiplexing requirements if they are spectrally stabilized, namely if they are inserted into an external cavity that dominates over the laser intrinsic cavity [86]. This approach, which is called spectral stabilization, has been known for several decades and widely exploited in the realization of low power, spectrally narrow single mode lasers for telecommunication applications [87] and high power laser bars [88, 89], and of tunable laser sources [90].

Spectral stabilization of high power laser diodes, besides for making them suitable for spectral multiplexing, can be useful also in the case of single modules for pumping of fiber lasers. Indeed, most fiber lasers are pumped by spectrally non-stabilized high power laser diodes modules, whose spectral width at 90% of power is larger than 5 nm (at the about 10 A working driving current), resulting in a non optimal absorption by the active fiber, whose absorption peak is usually about 1 nm wide. Moreover, such HPLD modules require a careful control of their temperature, in turn depending on the working current, to counteract the emission wavelength peak shift and keep the optical pumping as efficient as possible. The use of spectrally stabilized HPLDs, instead, increases the optical pumping efficiency by increasing the active fiber absorption peak overlap with the module spectrum and reduces the thermal control requirements because the peak emission wavelength is determined by the external cavity and not by the intrinsic one, whose gain is strongly dependent on the temperature of the diode and thus on its driving current [86].

The remaining of this chapter is organized as follows: in Sect. 3.1 a phenomenological approach to semiconductor laser diodes, useful to understand the general working principles of these devices, is recalled, followed by a discussion on the effect of the external cavity on the laser diode; then, in Sect. 3.2, the experimental results about the spectral stabilization and narrowing of a broad area, high power laser diode by means of external cavities using Volume Bragg Gratings (VBGs) is discussed. Finally, in Sect. 3.3 a novel approach to the stabilization of high power laser diodes exploiting fiber Bragg gratings in Large Mode Area (LMA) fibers is presented and experimental results demonstrating the feasibility of this approach are discussed.

3.1 A phenomenological approach to semiconductor laser theory

A semiconductor laser, in its simplest configuration (Fig. 3.1), is made of a volume of active material (a III-V semiconductor, alloys of GaAs for the diodes of main interest in this work) in which the stimulated emission process takes place, placed in an optical cavity delimited by two reflectors [86], which are typically obtained by depositing suitable dielectric layers directly on the active material facets to form dichroic mirrors. Such a structure is called the gain cavity and its design is responsible for all the features of the laser diode, from the emitted wavelength to the electro-optical efficiency and output power. In the case of edge emitting laser diodes – the only considered in this work –, the gain cavity develops along the laser optical axis, which is customarily taken as the z direction, and is two-dimensional being the active volume made up of quantum wells, whose thickness is negligible compared to its width and length [91]. With reference to figure 3.1, the current is injected along the y direction through two metal layers.

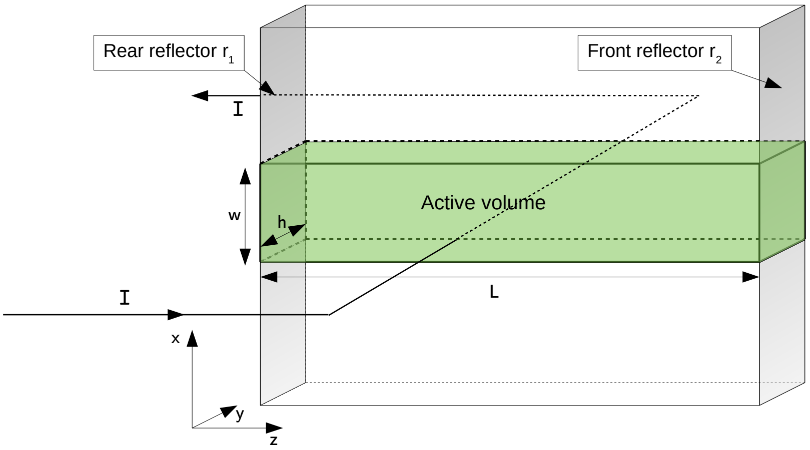

Figure 3.1: In plane, edge emitting laser diode structure. The green area represents the active layer, the grey surfaces represent the rear and front reflectors delimiting the optical cavity.

The physical mechanism that allows the generation of coherent radiation, which is what distinguishes laser diodes from LED [92], is the stimulated emission and is modeled by the photons and carriers rate equations [86]:

$$\begin{aligned}\frac{\mathrm{d}\,N}{\mathrm{d}t} &= \frac{\eta_{\mathrm{i}} I}{qV} - \frac{N}{\tau} - v_{\mathrm{g}} g N_{\mathrm{p}} \\ \frac{\mathrm{d}\,N_{\mathrm{p}}}{\mathrm{d}t} &= \Gamma v_{\mathrm{g}} g N_{\mathrm{p}} + \Gamma \beta_{\mathrm{sp}} N_{\mathrm{sp}} - \frac{N_{\mathrm{p}}}{\tau_{\mathrm{p}}}\end{aligned} \tag{3.1}$$

where N is the density of carriers and N_{p} is density of photons, η_{i} is the quantum efficiency, q is the electron charge, I is the injected current, τ is the carrier relaxation time, τ_{p} is the photon relaxation time, v_{g} is the photon group velocity, g is the optical gain, Γ is the so-called optical confinement factor and, lately, β_{sp} is the spontaneous emission factor and N_{sp} is the spontaneous photon generation rate. Note that the optical gain, which is function of the carrier density, temperature and wavelength. According to the width of the optical cavity, the laser diode can be single (transverse) mode, namely only the fundamental electromagnetic transverse mode is supported in the optical cavity, or multi mode. In the latter case the electric field in the cavity is given by the superposition of several electromagnetic modes and N_p is given by the sum of the photons associated with each mode, each one characterized by its own gain and group velocity [93].

The analysis of the behavior of a laser diode requires the simultaneous resolution of the rate equations in Eq. 3.1 using some numerical algorithms; however, for the stationary conditions, a quite detailed insight can be gained by a simpler phenomenological approach. Indeed, following the approach described in Ref. [86], in stationary conditions, as the injected current I increases, the density of carriers N increases too, leading to an increase of the gain, which is also a function of N. However, the electromagnetic field inside the optical cavity is basically the field in a waveguide and so it is given by the sum of the propagating modes, each characterized by its propagating constant:

$$\beta_\mathrm{m} = \beta^\mathrm{r}_\mathrm{m} + j\beta^\mathrm{i}_\mathrm{m} = \frac{2\pi n_\mathrm{m}}{\lambda} + \frac{j}{2}(\alpha_\mathrm{i} - g_\mathrm{m}) \tag{3.2}$$

where α_i takes into account the intrinsic losses, g_m is the modal gain, and n_m is the modal refractive index of the m-th propagating mode. The lasing condition is reached when, for any of the optical cavity modes $\vec{\mathcal{E}}_\mathrm{m}(x, y, z)$, the modal field is exactly equal to itself after one round trip, that is:

$$\vec{\mathcal{E}}_\mathrm{m}(x, y, z = 0) = \vec{\mathcal{E}}_\mathrm{m}(x, y, z = 2L_\mathrm{a}) \Longrightarrow r_\mathrm{rear}\, r_\mathrm{front}\, \mathrm{e}^{-2j\,\beta_\mathrm{m}\, L_\mathrm{a}} = 1 \tag{3.3}$$

where $r_\mathrm{rear/front}$ is the reflection coefficient of the rear/front facets. The real part of Eq. 3.3 is satisfied when the net modal gain g_m equals the net modal losses, that is when

$$g_\mathrm{m} = \alpha_\mathrm{i} + \alpha_\mathrm{m} = \alpha_\mathrm{i} + \frac{1}{2L_\mathrm{a}} \log\left(\frac{1}{r_\mathrm{rear} r_\mathrm{front}}\right) \tag{3.4}$$

Clearly, neither the gain can increase indefinitely (it would lead to an infinite electromagnetic field), nor the carrier density. Indeed, once the number of carriers reaches a threshold level N_th, which is also stationary, the number of generated carriers is equal to the recombining carriers, therefore:

$$\frac{\mathrm{d}N}{\mathrm{d}t} \Longrightarrow \frac{N_\mathrm{th}}{\tau} = \frac{\eta_\mathrm{i} I_\mathrm{th}}{qV} \tag{3.5}$$

It is worth noting that, at this point, the stimulated recombination, which is responsible for the recombination of the injected carriers in excess with respect to N_th, is negligible since there are no carriers in excess. As the number of carriers clamps to N_th, also the gain clamps at a threshold level:

$$g_\mathrm{th,m} = \alpha_\mathrm{i} + \alpha_\mathrm{m} \tag{3.6}$$

At this point, if the injected current increases, all the carriers in excess undergo a stimulated recombination processes contributing to the output power emitted by the laser. Consequently, above the threshold, the carrier rate equation, in stationary conditions, can be rewritten as:

$$\begin{aligned} \frac{\mathrm{d}\,N}{\mathrm{d}t} &= \frac{\eta_\mathrm{i}}{qV}(I - I_\mathrm{th}) - v_\mathrm{g} g_\mathrm{th} N_\mathrm{p} \Longrightarrow \\ \Longrightarrow \frac{\eta_\mathrm{i}}{qV}&(I - I_\mathrm{th}) = (\alpha_\mathrm{i} + \alpha_\mathrm{m}) v_\mathrm{g} N_\mathrm{p} \Longrightarrow \\ \Longrightarrow N_\mathrm{p} &= \frac{\eta_\mathrm{i}(I - I_\mathrm{th})}{qV(\alpha_\mathrm{i} + \alpha_\mathrm{m}) v_\mathrm{g}} \end{aligned} \tag{3.7}$$

Lately, the overall optical power emitted by the laser diode can be expressed as:

$$P_\mathrm{out} = \eta_\mathrm{i} \frac{h\nu}{q} (I - I_\mathrm{th}) \frac{\alpha_\mathrm{m}}{\alpha_\mathrm{m} + \alpha_\mathrm{i}} \tag{3.8}$$

The actual usable power is the one emitted by the front facet of the optical cavity, which is a fraction of the total emitted optical power and can be expressed as:

$$P_\mathrm{front} = F_\mathrm{front} P_\mathrm{out} = \frac{t^2_\mathrm{front}}{(1 - r^2_\mathrm{front}) + \dfrac{r_\mathrm{front}}{r_\mathrm{rear}}(1 - r^2_\mathrm{rear})} P_\mathrm{out} \tag{3.9}$$

where $t_\mathrm{rear/front}$, $r_\mathrm{rear/front}$ are, respectively, the absolute value of the transmission and reflection coefficient of the rear/front reflector in the optical cavity. For lossless reflectors, $t^2 + r^2 = 1$; in case $r^2 = t^2$ then $F_\mathrm{front} = 0.5$. It is clear that the optimal values for $r_\mathrm{rear/front}$ and $t_\mathrm{rear/front}$ must be determined according to the target application. For instance, in case of HPLDs, it is desirable to have a rear reflectivity as large as possible and a front reflectivity as small as possible, so that the largest part of the output power is emitted by the front facet, as can be from Fig. 3.2. These reflectivity values cannot be obtained by the bare refractive index contrast between the semiconductor facet and the surrounding air and this is why high reflectivity and low reflectivity coatings are deposited, respectively, on the back and front facet of the laser diodes.

3.1.1 External cavity laser theory

In Sect. 3.1, the basics of semiconductor laser theory have been briefly discussed, without, however, mentioning the laser diode spectrum, even if the spectral behavior of laser diodes largely depends on the optical cavity. As already pointed out in the previous section, the lasing condition is met when the modal gain equals the sum of intrinsic and mirror losses, reaching a threshold level.

Independently of the optical cavity dimensions, assuming a harmonic time dependence, the space varying part of the electric field within it can be written as

$$\vec{\mathcal{E}}_\mathrm{oc}(x, y, z) = \hat{e} \sum_\mathrm{l}^\mathrm{M} \phi_\mathrm{l}(x, y) e^{j\beta_\mathrm{l} z} \tag{3.10}$$

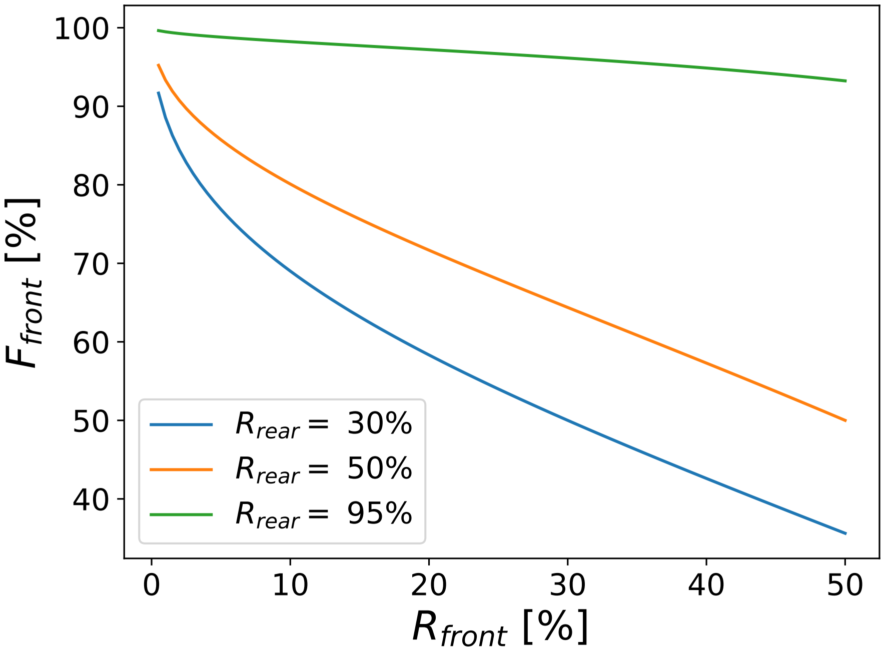

Figure 3.2: Fraction of power emitted from the front facet F_{front} as function of the front facet reflectivity R_{front} for three different values of rear reflectivity R_{rear}.

where M is the number of propagating modes, $\phi_{\mathrm{l}}(x, y)$ is the l-th mode of the electric field propagating along the z direction with a propagation constant β_{m} as defined in Eq. 3.2, and $\hat{e}$ is the polarization vector. The set of propagation constants and modes is obtained by finding the eigenvalue and eigenmodes of the electromagnetic field within the optical cavity. As already pointed out, the axial modes that actually give rise to the lasing condition are those such that the modal gain is equal to net modal losses. This condition allows not only finding the gain value at threshold, as shown in Eq. 3.6, but also determining the modal wavelength by solving the imaginary part of Eq. 3.3, which leads to [86]:

$$\beta_{\mathrm{m}} L_{\mathrm{a}} = m\pi \tag{3.11}$$

where it is assumed that the optical cavity is made only of an active part.

As it can be seen in Fig. 3.4, for a GaAs active layer characterized by an active length $L_{\mathrm{a}} = 500\,\mu\mathrm{m}$, a width of 200 µm, an height of about 1.5 µm ,and a refractive index around 3.5, which may realistically be the active layer of an edge HPLDs emitting in the wavelength interval delimited by 900 nm and 1 µm, the lowest longitudinal modes are well separated one from the others but, as the mode number m increases, the inter-modal wavelength separation decreases, becoming so dense for practical values of m that it can be approximated by a continuous set. Of course, of all the cavity modes, only those whose net modal gain equals their net modal

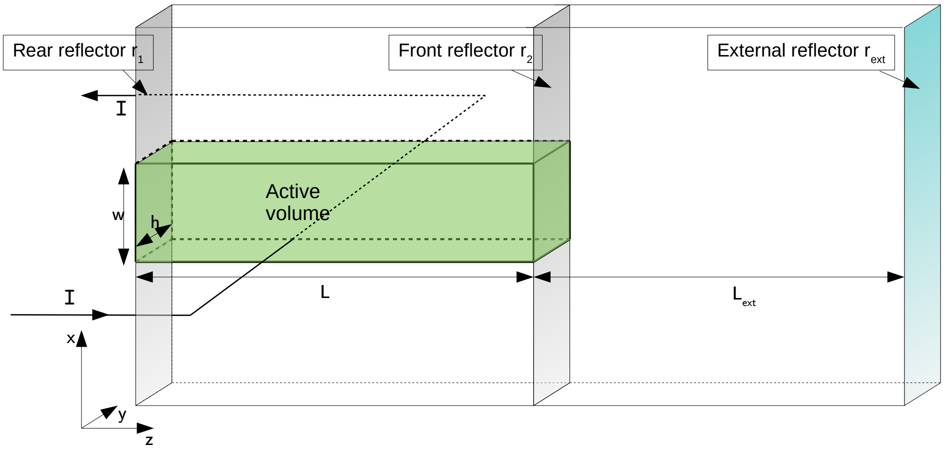

Figure 3.3: In plane, edge emitting laser diode structure complemented with an external cavity. The green area represents the active layer, the grey surfaces represent the rear and front reflectors delimiting the active part of the optical cavity, and the blueish surface represents the external reflector.

losses will actually reach the lasing condition and this can be controlled through the optical cavity design. HPLDs have a much wider spectrum than single mode laser diodes because of the combination of long cavities – leading to extremely small longitudinal intermode spacing around the lasing wavelength –, poor wavelength selectivity of the mirrors, and non linear thermo-optical effects [94, 95, 96].

As discussed above, since any axial mode can satisfy Eq. 3.11, what actually determines the spectral characteristics of HPLDs is the modal gain. The HPLD peak wavelength and spectral width are determined by the gain peak wavelength and by the spectral width of the gain. As shown in Fig 3.5 and in Fig. 3.6, the gain shape, in general, is indeed mainly a function of the temperature and the carrier density [97]. As the temperature increases, the gain peak shifts toward larger wavelengths. As the carrier density increases, the gain peak increases as well until the threshold value is reached. From this point on, which coincides with the driving current reaching the threshold value, the modal gain changes are essentially driven by changes in the laser temperature. Consequently, as the device temperature increases, the laser peak wavelength shifts towards longer wavelength and the laser spectral width increases.

The Laser Diode Spectral Stabilization (LDSS) can be achieved by complementing the laser diode optical cavity with an external passive cavity formed by an additional wavelength selective reflector, characterized by a reflection coefficient

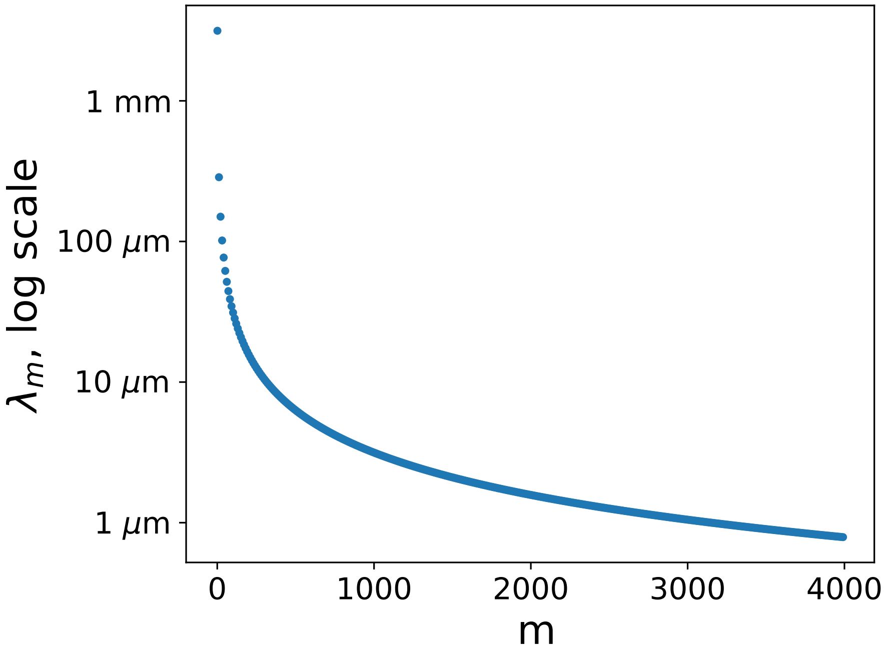

Figure 3.4: Modal wavelength of the longitudinal modes as function of the modal number.

$r_{\mathrm{ext}}(\lambda)$, which is in general complex and not constant over the given target wavelength range, at a distance L_{ext} from the front reflector of the diode optical cavity, as shown in Fig. 3.3. The behavior of this structure can be conveniently analyzed considering an equivalent complex reflector that takes into account the features of the front reflector, the free space between the front reflector and the external one and, finally, the external reflector. As shown in Ref. [86], the equivalent reflection coefficient can be computed from the transmission matrix resulting from cascading the transmission matrix of the reflectors and the free space, or exploiting the scattering (S), matrix of the single elements. In any case, with reference to Fig. 3.3, the equivalent reflection coefficient $r_{\mathrm{eff}}(\lambda)$ is:

$$r_{\mathrm{eff}}(\lambda) = r_2 + \frac{t_2^2\, r_{\mathrm{ext}}(\lambda)\, \mathrm{e}^{-2j\beta_{\mathrm{ext}}L_{\mathrm{ext}}}}{1 + r_2\, r_{\mathrm{ext}}(\lambda)\, \mathrm{e}^{-2j\beta_{\mathrm{ext}}L_{\mathrm{ext}}}} = |r_{\mathrm{eff}}(\lambda)|\mathrm{e}^{j\theta_{\mathrm{eff}}(\lambda)} \tag{3.12}$$

Once $r_{\mathrm{eff}}(\lambda)$ is computed, the real part of the round trip equation takes the form

$$\begin{aligned} g_{\mathrm{m}}(\lambda) &= \alpha_{\mathrm{i}} + \alpha_{\mathrm{m,eff}}(\lambda) \\ \alpha_{\mathrm{m,eff}}(\lambda) &= \frac{1}{2L_{\mathrm{a}}} \log \frac{1}{r_{\mathrm{rear}}|r_{\mathrm{eff}}(\lambda)|} \end{aligned} \tag{3.13}$$

while the imaginary part takes the form

$$\beta_{\mathrm{m}} L_{\mathrm{a}} + \theta_{\mathrm{eff}}(\lambda) = l\pi \tag{3.14}$$

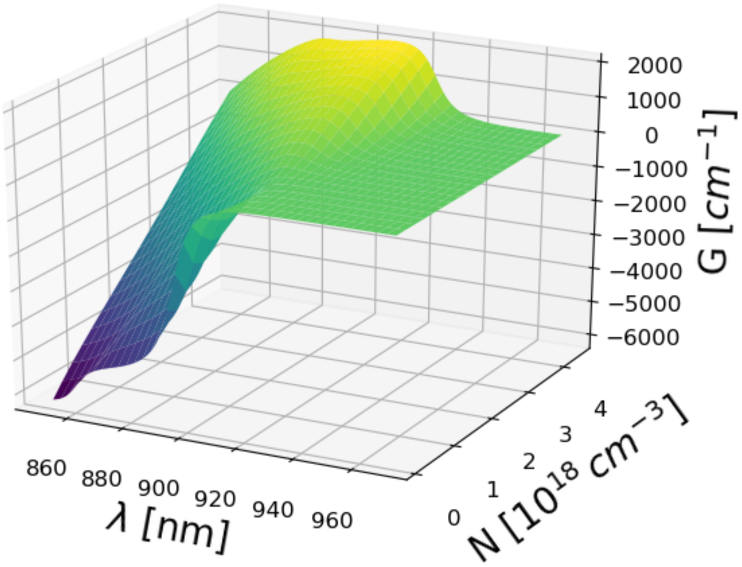

Figure 3.5: Typical GaAs quantum well gain for different values of carrier density at constant temperature.

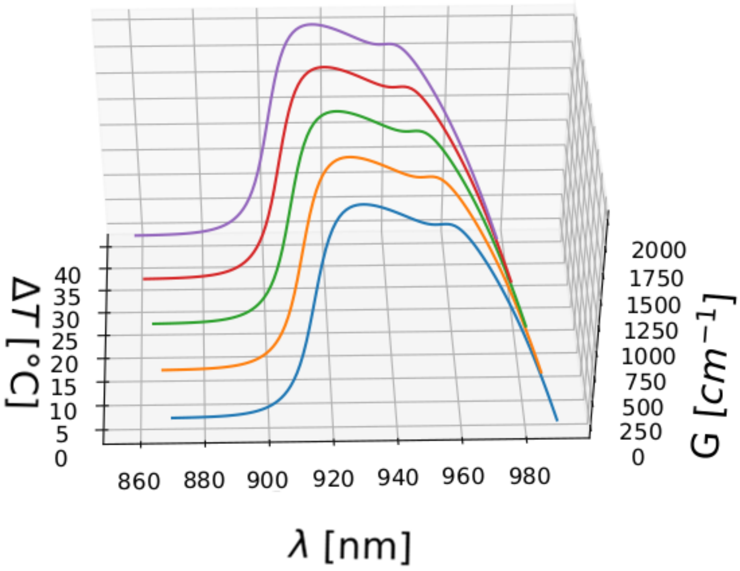

Figure 3.6: Typical GaAs quantum well gain for different values of temperature shifts at fixed at constant density of carrier density.

All the physical, steady state properties, of these devices, as the power versus injected current characteristic for instance, can be obtained just by substituting r_2 with $r_{\text{eff}}(\lambda)$ in Eq. 3.4, Eq. 3.8, and Eq. 3.6. As in the case of the single cavity laser diode, Eq. 3.14 does not tell much about the spectral behavior of the laser diode. Indeed, since L_{a} is much larger that the wavelength, the longitudinal modes whose wavelength is in the spectral gain region form an almost continuous set allowing the propagation of any transverse mode. In case of HPLDs, the effect of the external cavity can be appreciated mostly by analyzing Eq. 3.13.

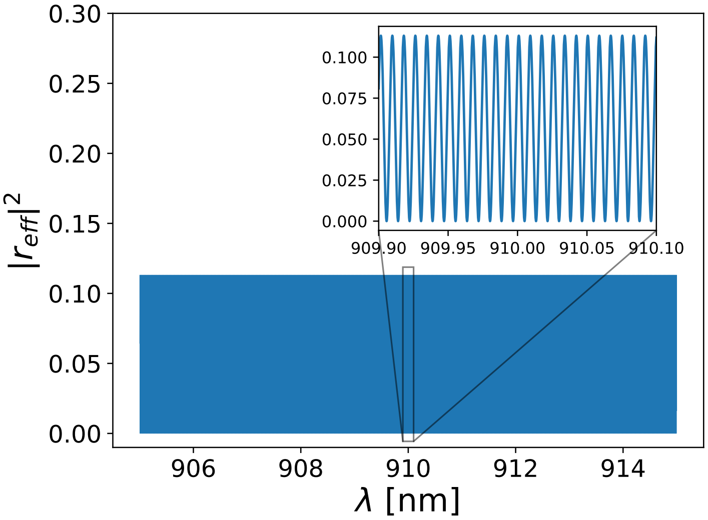

Figure 3.7: Reflectivity of the effective reflector equivalent to a front reflector with a reflectivity equal to 3% and a broadband external reflector with a reflectivity of 8% placed at a distance of 10 cm from the front reflector.

Indeed, as it can be seen comparing Fig. 3.7 and Fig. 3.8, the reflectance of the external reflector changes extremely as the external reflector varies from a broadband mirror with a 10% reflectivity to an extremely narrow notch filter having a peak reflectivity equal to 8.5% at 910 nm. In both cases, the front reflector has been considered to be a broadband mirror with a 3% reflectivity, while the external reflector is placed at 10 cm from it, a distance that is typical for HPLD modules spectral stabilization. In the first case, the effective refractive index shows the periodicity typical of a 3 mirror Fabry-Perot cavity, with an extremely small wavelength period due to $L_{\text{ext}} \gg \lambda$ [98, 99]. In the second case, the notch filter generates a significant change of $r_{\text{eff}}(\lambda)$ with respect to r_2 only around the notch filter peak wavelength. The nature of this kind of filter and how it can be obtained will be discussed lately in this chapter.

Since the reflectivity of the facets is constant all over the considered wavelength range, in the case of a single-cavity broad-area laser, the spectrum is essentially

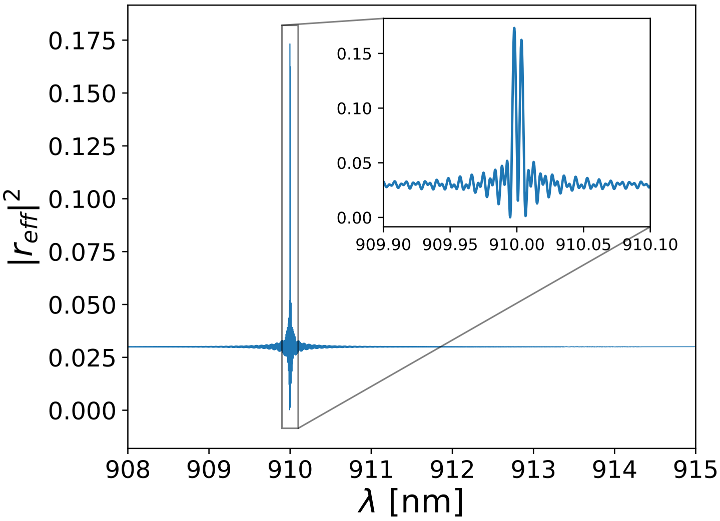

Figure 3.8: Reflectivity of the effective reflector equivalent to a front reflector with a reflectivity equal to 3% and an optical notch filter with a maximum reflectivity of 8% placed at distance at a distance of 10 cm from the front reflector.

determined by the modal gain, which shift as the temperature increases. This is not true for the external cavity configuration made by a laser and and a notch filter, as can be the one resulting from using a fiber Bragg grating or a volume Bragg grating to implement the external cavity. Indeed, the spectrum is the result of the competition between the modal gain and the effective optical losses, which are wavelength dependent. As can be seen from Fig. 3.9, the net gain $g_{\mathrm{net}}(\lambda) = g_{\mathrm{m}}(\lambda) - \alpha_{\mathrm{eff,m}}(\lambda)$ does not maintain the shape and features of the modal gain, as in the case of single cavity broad area lasers, but it shows a peak around the filter peak wavelength, which corresponds to the laser peak wavelength if it is also a global maximum of the net gain. If this happens, and the external cavity contribution on the net gain is dominant, a change in the temperature will affect the laser spectrum in the same way as it affects $r_{\mathrm{eff}}(\lambda)$. As shown in Fig. 3.6, typically a HPLD without external cavity exhibits a peak wavelength shift of about $0.3\,\mathrm{nm\,K^{-1}}$, while using a fiber Bragg grating or a volume Bragg grating for the external stabilization the increase in the temperature results in peak wavelength shift of about $0.01\,\mathrm{nm\,K^{-1}}$, which is about one order of magnitude smaller than the bare laser spectral shift.

It is possible to identify three different working regime of a HPLD externally stabilized through a notch filter depending on the reflectivity of the front and external reflector. If the front reflector has a much higher reflectivity than the external reflector, the external cavity contribution will be negligible since the gain curve will be dominated by the modal gain; hence, the laser will behave just like a spectrally unstabilized laser, so that the peak wavelength will keep shifting towards

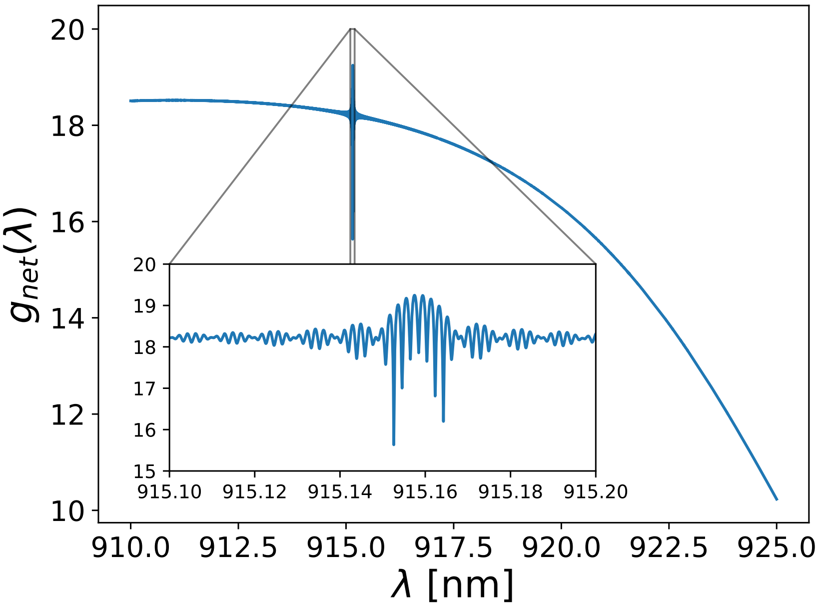

Figure 3.9: Net modal gain with $r_{\text{front}} = 0.03$ and $max_{\lambda}\{|r_{\text{ext}}|^2(\lambda)\} = 0.08$.

longer wavelengths as the temperature of the device increases, except for a very small temperature interval in which the peak wavelength is stable because of the external cavity contribution (Fig. 3.10). In this case, the steady state properties of the weakly stabilized laser are basically the same as the steady state properties of the unstabilized one, including the threshold current and the PI slope, except for the stabilized spectrum in a very small narrow temperature range.

If the front reflector reflectivity is of the same order of magnitude of the external reflector, a second working regime can be observed. In this regime, the HPLD is "semi-stabilized" since there is a wider temperature interval in which the external cavity dominates over the internal cavity (Fig. 3.11). In this case, the stabilized HPLD shows a decrease of the PI slope larger than the one in the regime of weak stabilization. Indeed, as the temperature increase, the laser passes from a condition where the external cavity dominates over the intrinsic one, to a condition where the intrinsic cavity dominates and the laser behavior becomes equal to that of the unstabilized version. This transition is marked by the appearance of two wavelengths sharing the same net gain, which makes possible the simultaneous presence of two peaks in the laser spectrum.

Finally, a third stabilization regime is verified when the front reflector has a reflectivity much smaller than the notch filter peak reflectivity. From a quantitative point of view this condition happens when the reflectivity of the external reflector is about one order of magnitude larger than the reflectivity of the front facet. In this case, the HPLD is spectrally stabilized over a very large temperature interval

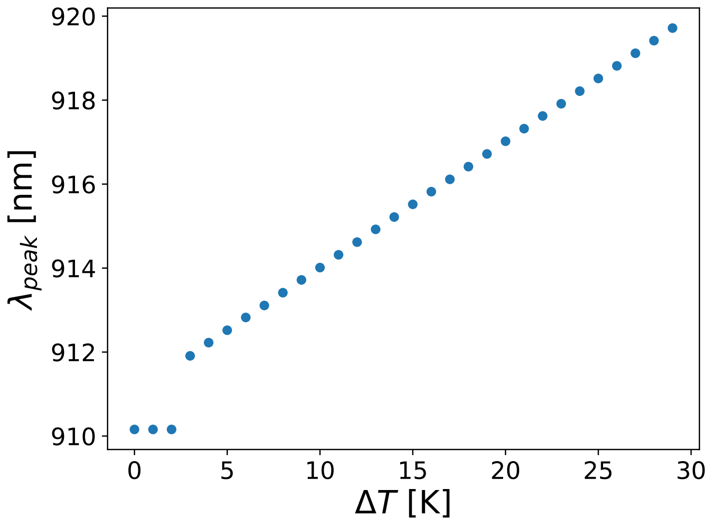

Figure 3.10: Laser peak wavelength λ_{peak} versus the device temperature increase $\Delta T = T - T_{\text{ref}}$ in the first spectral regime, with $r_{\text{front}} = 3\%$, $\max_{\lambda}\{r_{\text{ext}}(\lambda)\} = 0.2\%$, and $T_{\text{ref}} = 291.15\,\text{K}$.

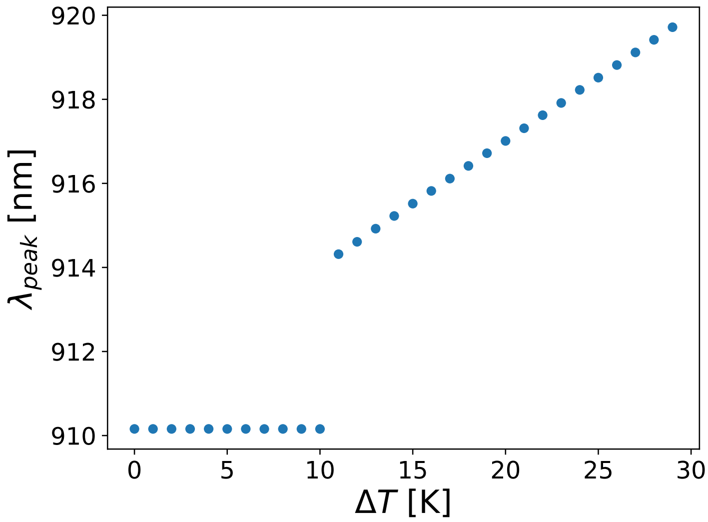

Figure 3.11: Laser peak wavelength λ_{peak} versus the device temperature increase $\Delta T = T - T_{\text{ref}}$ in the second spectral regime, with $r_{\text{front}} = 3\%$, $\max_{\lambda}\{r_{\text{ext}}(\lambda)\} = 1.5\%$, and $T_{\text{ref}} = 291.15\,\text{K}$.

because the net gain curve is dominated by the effective optical losses; therefore, the wavelength for which the net gain is maximum corresponds to the notch filter peak wavelength, as can be seen in Fig. 3.12. In this case, which is typical when the external cavity is made by a highly reflective VBG and is discussed in deeper details in the next section, the threshold current decreases significantly since, on average, the effective reflectivity is higher than in the single cavity case; on the contrary, the PI slope decreases compared to the other regimes and the spectrum remains narrow with an almost constant peak wavelength over a temperature interval as wide as 40 K.

It is worth noting that in all these spectral regimes the peak wavelength of the stabilized laser diode is not exactly constant with temperature but it shows some extremely small variations, in the order of 1 pm. These variations, underlined in the inset of Fig. 3.12, are originated by the interference between a front and an external reflectors placed at a distance much greater than the laser wavelength one from the other, which also give rise to the complex and periodic pattern that characterizes $g_{\mathrm{net}}(\lambda)$, as it can be seen in Fig. 3.9. This phenomenon, here theoretically predicted, is actually very difficult, if not impossible, to experimentally measure since it would require to appreciate peak wavelength shift of the order of 1 pm that can be easily confused with random variation of the dominant electromagnetic modes or be given by shifts due to thermal noise.

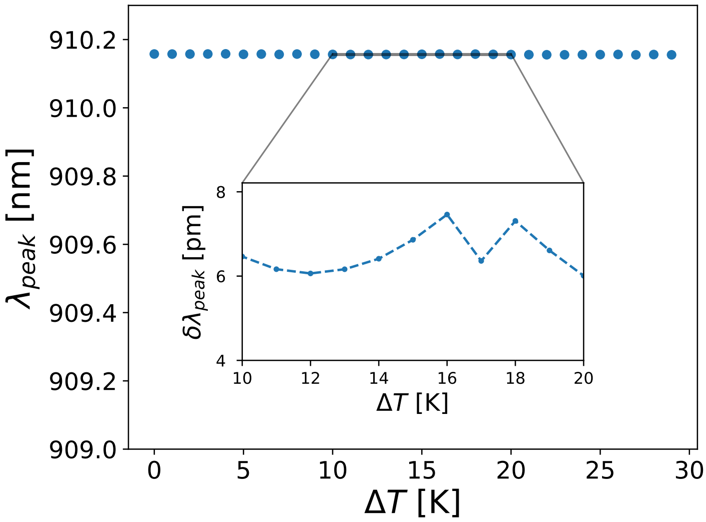

Figure 3.12: Laser peak wavelength λ_{peak} versus the device temperature increase $\Delta T = T - T_{\mathrm{ref}}$ in the third spectral regime, with $r_{\mathrm{front}} = 3\%$, $max_{\lambda}\{r_{\mathrm{ext}}(\lambda)\} = 8\%$ and $T_{\mathrm{ref}} = 291.15\,\mathrm{K}$. The inset highlights the small variations of the peak wavelength from the average value equal to 910.15 nm.

3.2 Spectral stabilization via volume Bragg grating

So far a theoretical model of an external cavity, high power laser diode has been discussed and, particularly, the effect of this configuration on the laser spectrum has been examined. According to the reflectivity of the front and external reflector and to the modal gain curve, the external cavity HPLD, from now on EC-HPLD, can show an almost constant peak wavelength over a temperature interval up to some tens of degrees. In order to realize an EC-HPLD, a HPLD must be complemented with an external cavity, which means, experimentally speaking, that an optical notch filter must be precisely placed at a distance L_{ext} from the front reflector, as shown in Fig. 3.3. In realistic applications such an optical notch filter, which selects the optical feedback fed into the active cavity, can either be a Volume Bragg Grating (VBG) or a Fiber Bragg Grating (FBG).

3.2.1 Volume Bragg grating theory

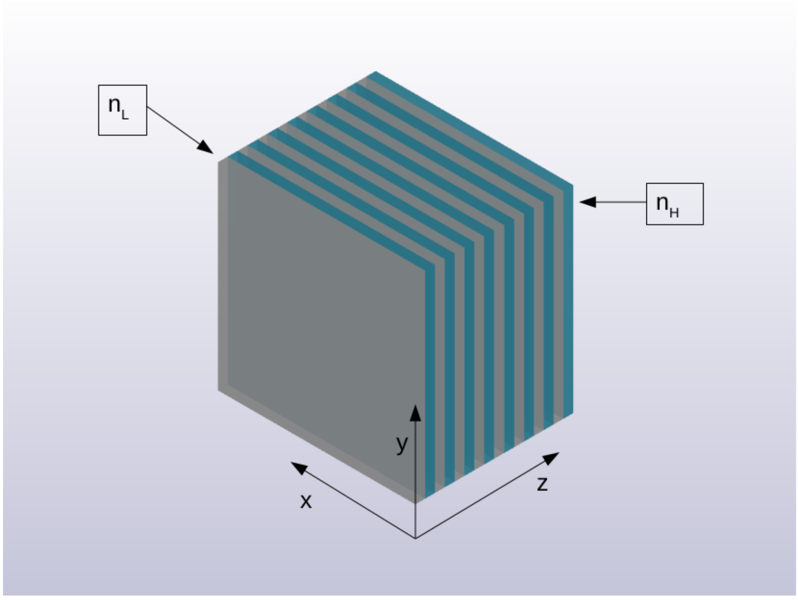

Figure 3.13: Schematic representation of a VBG. The blueish layers represents the high refractive index layers, the grayish layers the low refractive index ones.

As already pointed out, the notch filter required to build an external cavity on top of an HPLD can be a VBG, which in general is a stack of dielectric layers engineered in such a way that the partial reflections of an incident electromagnetic wave interfere constructively at each dielectric interface only for a target wavelength.

With reference to Fig. 3.13, is it clear that a VBG is just a sequence of dielectric layers stacked along the laser propagation direction, each one characterized, in general, by its own thickness and refractive index. Assuming that the incident beam extension is much smaller than the VBG extension, it is well known that in this kind of geometry any electromagnetic field can be decomposed in TE (or s-polarized) and in TM (or p-polarized) plane waves conserving, at any point of the stack, the transverse component of the wave vector $k_{\mathrm{x}} = \xi$, assuming an invariance along y. In this framework, Maxwell equations can be reduced to a cascade of equivalent transmission lines, one for each incident plane wave [100]. The evolution of an incident plane wave into each layer is governed by

$$\begin{cases} -\dfrac{\mathrm{d}V}{\mathrm{d}z} = jk_{\mathrm{z}} Z_{\infty} I \\[2ex] -\dfrac{\mathrm{d}I}{\mathrm{d}z} = jk_{\mathrm{z}} Y_{\infty} V \end{cases} \tag{3.15}$$

where $k_{\mathrm{z}} = \sqrt{\left(\dfrac{2\pi n}{\lambda}\right)^2 - \xi^2}$, $Y_{\infty} = \dfrac{1}{Z_{\infty}}$ and

$$\begin{array}{c|c} TE \text{ modes} & TM \text{ modes} \\ & \\ V(z,\xi) = E_{\mathrm{y}}(z,\xi) & V(z,\xi) = E_{\mathrm{x}}(z,\xi) \\ I(z,\xi) = -H_{\mathrm{x}}(z,\xi) & I(z,\xi) = H_{\mathrm{y}}(z,\xi) \\ Z_{\infty} = \dfrac{\omega\mu}{k_{\mathrm{z}}} & Z_{\infty} = \dfrac{k_{\mathrm{z}}}{\omega\epsilon} \end{array} \tag{3.16}$$

The solution of Eq. 3.15 can be written in the form of traveling waves as:

$$\begin{aligned} V(z,\xi) &= V_0^+(\xi)\mathrm{e}^{-jk_z z} + V_0^-(\xi)\mathrm{e}^{jk_z z} \\ I(z,\xi) &= I_0^+(\xi)\mathrm{e}^{-jk_z z} + I_0^-(\xi)\mathrm{e}^{jk_z z} \end{aligned} \tag{3.17}$$

which is the form of the eigenmodes of the electromagnetic field in a homogeneous space with refractive index n.

With reference to the cascade of transmission lines in Fig. 3.13, the reflectivity of a cascade of such dielectric layers can be computed using a recursive algorithm to compute the reflectivity of the equivalent transmission line cascade. Letting $M+2$ to be the number of equivalent transmission lines, which correspond to M dielectric layers and an infinitely thick surrounding medium at the begin and at the end of the dielectric stack, firstly the characteristic impedance $Z_{\infty,\mathrm{i}}$ and propagation constant $k_{\mathrm{z,i}}$ for each transmission line must be computed. Then, the Fresnel reflection coefficients can be computed at each interface as:

$$\rho_{\mathrm{i}} = \frac{Z_{\mathrm{inf,i}} - Z_{\mathrm{inf,i-1}}}{Z_{\mathrm{inf,i}} + Z_{\mathrm{inf,i-1}}} \tag{3.18}$$

Starting from the last interface, the reflection coefficient Γ_l can be computed backward as

$$\Gamma_\mathrm{l} = \frac{\rho_\mathrm{l} + \Gamma_\mathrm{l+1}\mathrm{e}^{-2jk_{\mathrm{z,l}}L_\mathrm{l}}}{1 + \rho_\mathrm{l}\Gamma_\mathrm{l+1}\mathrm{e}^{-2jk_{\mathrm{z,l}}L_\mathrm{l}}}, \quad l = M, M-1, ...1 \tag{3.19}$$

Finally, the reflectivity of the stack can be computed as

$$R(\lambda) = |\Gamma_1(\lambda)|^2 \tag{3.20}$$

In the case of a VBG, the optical notch filter is made by a periodic variation of the refractive index obtained from a binary stack of M dielectric layers with 0.25 optical thickness. It is preferable that the refractive index variation between the high refractive index layer and the low refractive index layer is very small, in the order of few percents. Assuming that the surrounding medium is air, it can be shown that, at the peak wavelength and for normal incidence, the reflection coefficient Γ_1 of the stack is [100]:

$$\Gamma_1(\lambda_\mathrm{peak}) = \begin{cases} \dfrac{\left(\dfrac{n_\mathrm{H}}{n_\mathrm{L}}\right)^{2M} - 1}{\left(\dfrac{n_\mathrm{H}}{n_\mathrm{L}}\right)^{2M} + 1} & \text{if M even} \\[2ex] \dfrac{1 - \left(\dfrac{n_\mathrm{H}}{n_\mathrm{L}}\right)^{2M} n_\mathrm{H}^2}{1 + \left(\dfrac{n_\mathrm{H}}{n_\mathrm{L}}\right)^{2M} n_\mathrm{H}^2} & \text{if M odd, } \mathrm{n_1 = n_M = n_H} \end{cases} \tag{3.21}$$

with λ_peak being the central wavelength of the reflected band, $n_\mathrm{H} > n_\mathrm{L}$ the high and low refractive index, respectively. Fig. 3.14 shows the spectral response of this kind of filter as the number of layers they are made of increases. Indeed, with a refractive index difference equal to 0.001, which in this case corresponds to refractive index variation of just about 0.05%, as the number of layer increases from 1600 to 3000, the reflectivity increase from 15% to 40%, while the reflectivity peak width at 90% decreases as the number of layers increases.

Once the reflectivity is computed, it can be inserted into Eq. 3.13 to determine the behavior of a given laser diode when such a Bragg grating is used as the external reflector. In a typical case of a laser diode emitting at 9xx nanometers (a compact form used to identify any wavelength in the 900 nm to 999 nm, which is one used for pumping Yb-doped industrial fiber lasers), a peak grating reflectivity as large as 15% is enough to spectrally stabilize the diode in a temperature range as large as 30 K.

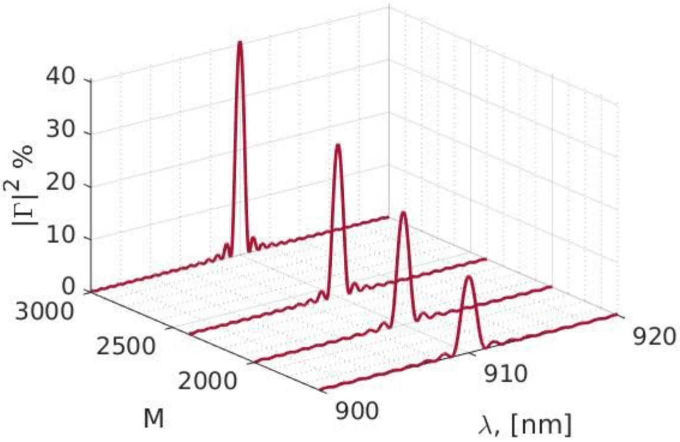

![ht]

Figure 3.14: Theoretical reflectance of a VBG with $n_\mathrm{H} = 1.989$, $n_\mathrm{L} = 1.988$ for increasing number of layers.

3.2.2 Experimental results

The spectral stabilization of a single HPLD exploiting a VBG as an external reflector has been experimentally tested using Fabry-Perot, broad area, semiconductor laser diodes nominally emitting at 973 nm produced by Convergent Photonics. These emitters generate up to 10 W of optical power with a driving current equal to 10 A as it is shown in Fig. 3.15, and an electro-optical efficiency of about 50%; their spectrum exhibits a peak wavelength ranging from 965 nm to 973 nm, shown in Fig. 3.16, with a spectral width at 95% ranging from 2 nm to 4.5 nm as the driving current increases from 2 A to 10 A, which is shown in Fig. 3.17. A set of VBGs, manufactured by Ondax, with peak reflectivity equal to 20% or 30% at 976 nm and a FWHM reflectivity equal to 1 nm has been used as the external cavity reflector. It is well known that the spectral stabilization is particularly sensible to the alignment of the external reflector in front of the front reflector. Therefore, the placement and alignment of the external reflector in front of the diode facet at about 10 cm from it has been carried out using a gripper mounted on a 6-axis piezoelectric movement system having an angular accuracy of the order of 1^{-2} degrees and a linear translation accuracy better than 0.1 µm. A manual active alignment approach has been used by raster scanning the VBG position with respect to the diode front facet while continuously monitoring the output power and spectral shape until the diode is spectrally stabilized, namely the spectral width at 95% reduces drastically and the spectral shape changes from one characterized by multiples peaks and valleys to one with a single peak that closely resembles the VBG reflectivity shape.

As it can be seen in Fig. 3.15 the slope of the PI curve of the stabilized laser is smaller than that of the unstabilized diode. This is expected not only because of the losses in the VBG but also because the emitter differential efficiency is decreased due to the increase in the front reflectivity (through the effective reflectivity mechanism). Quantitatively, this is translated into an average loss of 22.5% using the 30% reflectivity VBG and of 19% using the 20% reflectivity VBG. The main effect of the spectral stabilization is instead clearly visible in Fig. 3.16, in which the peak wavelength of the stabilized and unstabilized chips versus the driving current in shown to demonstrate the effectiveness of the stabilization, since for both values of the VBG reflectivity, the emitted wavelength barely changes over the entire driving current range. Finally, also the 95% spectral width of the stabilized emitter shows a drastic improvement compared to the 95% spectral width of the unstabilized one, as it is possible to appreciate in Fig. 3.17.

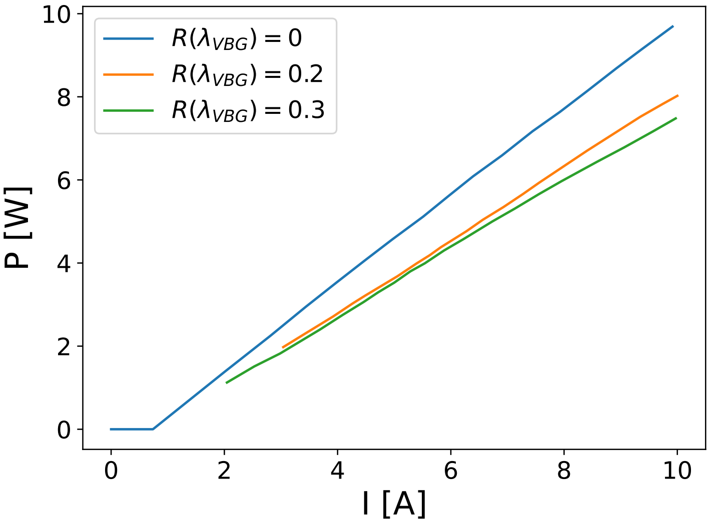

Figure 3.15: Comparison of the PI curves for a Fabry-Perot laser diode from Convergent Photonics nominally emitting at 973 nm in three conditions: unstabilized (blue curve), stabilized with a 20% reflectivity VBG (orange curve), and stabilized with a 30% reflectivity VBG (green curve).

The experimental data show very good performance in terms of spectral width and stability of the peak wavelength however the main drawback of this approach is a 20% decrease, on average, of the emitter output power. Nevertheless, the performances of the stabilized diodes can be improved decreasing the reflectivity of the external grating. Indeed, it would in turn results in an increase of the diodes efficiency, as demonstrated by Fig. 3.15, showing better performances for diodes stabilized by a 20% reflectivity grating compared to diodes stabilized by a 30% reflectivity one.

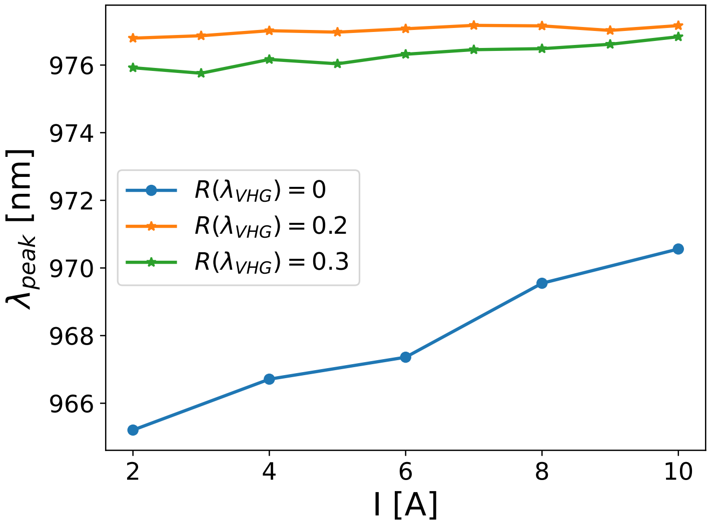

Figure 3.16: Peak wavelength shift against the driving current at a constant heat sink temperature equal to 18 °C for the laser diode in Fig. 3.15. The colors of the curves have also the same meaning of the cited figure.

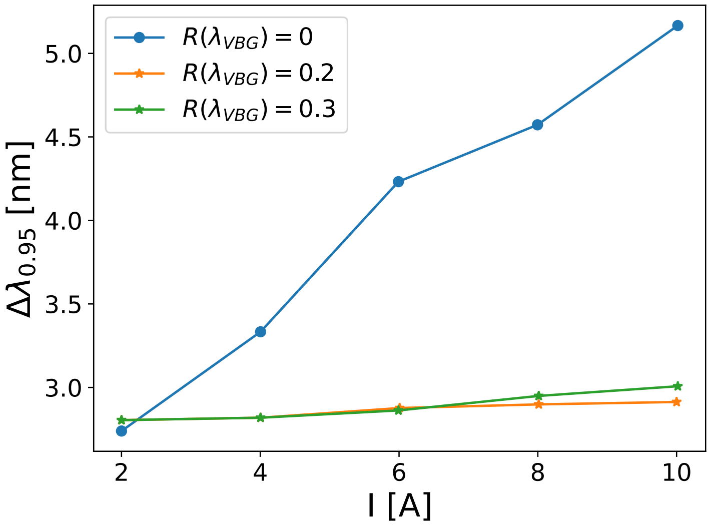

Figure 3.17: Spectral width at 95% against the driving current at a constant heat sink temperature equal to 18 °C laser diode in Fig. 3.15. The colors of the curves have also the same meaning of the cited figure.

3.3 Spectral stabilization via fiber Bragg grating

Another approach for the single emitter spectral stabilization consists in the use of FBGs instead of VBGs. VBGs and FBGs share the same working principle

– a periodic refractive index variation – but implement with discrete bulk and waveguide components, respectively. The reasons for FBGs being advantageous over VBGs in the emitter spectral stabilization are mainly two: flexibility and loss reduction. Indeed, as already pointed out, the use of VBGs implies a substantial decrease of the emitter output power due to the bulk nature of the VBG. With reference to Fig. 3.13, in the case of an FBGs the external reflector is incorporated inside the delivery optical fiber itself, so (ideally) no additional scattering loss occurs. Moreover, in order to spectrally stabilize an emitter exploiting a VHG, the VHG must be inserted into the emitter package, thing that implies additional costs both for the assembly time and the need a specific package. On the contrary, an FBG can be written in the delivery fiber, which has to be assembled in any case. However, there is also a drawback in choosing FBGs over VBGs: inscribing FBGs in very large core area fibers, as typically are the fibers used for high power laser delivery, is more difficult. Indeed, FBGs can be fabricated by exposure through a phase mask to UV or femtosecond laser or by direct exposure to focused femtosecond laser pulses. In order not to couple light from the core to the cladding, the refractive index modifications the FBG is build upon should be as homogeneous as possible covering the whole area of the fiber core which, in case of the delivery fiber for HPLDs, can be be as large as 200 µm. In general, the phase mask based method allows for the inscription of extremely precise refractive index modulation with a spatial extend of very few tens of micrometers at most, hence it is not suited for FBG inscription in very large core area fibers. The direct exposure to focused femtosecond laser pulses is a younger fabrication method compared to the already mentioned one, and have been extensively used to manufacture FBGs for many type of fibers, including multimode ones. Indeed, it allows for the control of the spatial extension of the refractive index at the expenses of the refractive index variation homogeneity. Based on that, the use of the latter fabrication method may cause the coupling of the core modes with the cladding and radiating modes. While it would not be a concern for sensing application, it poses a challenge for high power application where optical losses should be reduced to the minimum both for safety and economical reasons.

3.3.1 Fiber Bragg grating theory

With reference to Fig. 3.18, FBGs are essentially made of weak, periodic variations of the refractive index induced in the core of an optical fiber. The FBG refractive index can, therefore, be expressed as:

$$\begin{gathered} n_{\text{fbg}}^2(z) = n_0^2 + \delta n^2(z) \\ n_{\text{fbg}}(z+\Lambda) = n_{\text{fbg}}(z) \Longrightarrow \delta n(z+\Lambda) = \delta n(z) \\ \delta n << n_0 \end{gathered} \tag{3.22}$$

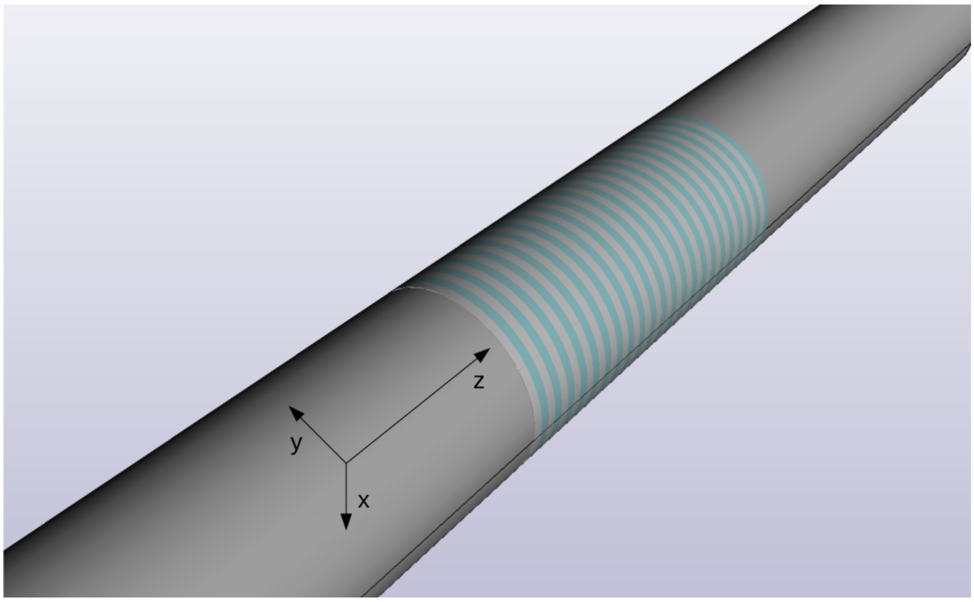

Figure 3.18: Schematic representation of an FBG inside the optical fiber core. The bluish and light gray layers represent the refractive index variation inside the fiber.

where n_0 is the refractive index of the pristine optical fiber core, Λ is the grating period and $\delta n(z)$ is a small and periodic refractive index variation. Such optical structure can be analyzed by means of the so called Coupled Mode Theory (CMT) [101]. The CMT is a general perturbative framework that allows reducing Maxwell equations into a set of first order partial differential equation relying on two assumption: i) the electromagnetic field can be decomposed into a discrete number of modes; ii) the Slowly Varying Envelope Approximation (SVEA) holds. In the case of FBGs both assumptions are valid. The electromagnetic field is guided by the optical fiber, so it can be decomposed in a superposition of optical fiber modes:

$$\vec{E}(\vec{r}) = \sum_{\mathrm{m,n}} \alpha_{\mathrm{m,n}} \vec{\phi}_{\mathrm{m,n}}(x,y) e^{-j\beta_{\mathrm{m,n}} z} \tag{3.23}$$

where $\vec{\phi}_{\mathrm{m,n}}(x,y)$ is a fiber mode normalized to have $|\alpha_{\mathrm{m,n}}|^2$ representing the power carried by that particular mode, and $\beta_{\mathrm{m,n}}$ is the mode propagation constant. The SVEA holds because the refractive index variation $\delta n(z)$ is assumed to be small [102]. In general, in the case of an unperturbed refractive index, being orthogonal, the modes do not exchange power among themselves so the mode amplitudes remain constant along the fiber. However, in presence of a refractive index perturbation, a power exchange between the modes can occur and the mode amplitudes change along the propagation direction. It can be shown that the evolution along z of these coefficients is described by 3.24 [103]:

$$
\begin{aligned}
\frac{\mathrm{d}\,\alpha_{\mathrm{l,m}}}{\mathrm{d}\,z} &= j\sum_{s,t}\kappa_{\mathrm{l,s}}^{m,t}(z)\alpha_{\mathrm{s,t}}(z)\mathrm{e}^{j(\beta_{\mathrm{s,t}}-\beta_{\mathrm{l,m}})z} \\
\kappa_{\mathrm{l,s}}^{m,t}(z) &= \frac{\omega}{4}\iint \vec{\phi}^{\dagger}_{\mathrm{l,m}}(x,y)\delta n^2(x,y,z)\cdot\vec{\phi}_{\mathrm{s,t}}(x,y)\,\mathrm{d}x\mathrm{d}y
\end{aligned}
\tag{3.24}
$$

where the $\vec{\phi}^{\dagger}$ stands for the transposed complex conjugate of $\vec{\phi}$ and $\{\alpha_{\mathrm{m,n}}(z)\}_{\mathrm{l,m}}$ is the set of complex mode amplitude including both the forward and backward propagating modes. In general, Eq. 3.24 does not have an analytical solution, so numerical solvers, particularly those based on the finite difference method [103] or the Runge-Kutta method [104], need to be used. However, some insight about the general behavior of FBGs can be gathered by studying FBGs in single mode fibers (SMF), the only case for which an analytical solution of Eq. 3.24 can be found.

In an SMF only the fundamental mode can propagate through the fiber without (ideally) experiencing any loss. The mode amplitude can be written as a superposition of a forward propagating and backward propagating components; therefore the electric field inside the fiber can be written as:

$$
\vec{E}(x,y,z) = \alpha_0(z)\vec{\phi}_0(x,y) = [\alpha_+(z)\mathrm{e}^{-j\beta_0 z} + \alpha_-(z)\mathrm{e}^{j\beta_0 z}]\vec{\phi}_0(x,y)
\tag{3.25}
$$

Once the coupling coefficient between the forward and backward propagating parts of the fundamental mode is expressed as a Fourier series along the z axis as

$$
\kappa_0(z) = \sum_{\mathrm{i}=-\infty}^{\infty} c_i\,\mathrm{e}^{j2\pi i\,\frac{z}{\Lambda}}
\tag{3.26}
$$

Eq. 3.24 reduces to:

$$
\begin{cases}
\dfrac{\mathrm{d}\,\alpha_+(z)}{\mathrm{d}\,z} = -j\alpha_-(z)\displaystyle\sum_{\mathrm{l}} c_{\mathrm{l}}\,\mathrm{e}^{jz(2\beta_0-2\pi\,\frac{l}{\Lambda})} \\
\dfrac{\mathrm{d},\alpha_-(z)}{\mathrm{d},z} = j\alpha_+(z)\displaystyle\sum_{\mathrm{l}} c_{\mathrm{l}}\,\mathrm{e}^{-jz(2\beta_0-2\pi\,\frac{l}{\Lambda})}
\end{cases}
\tag{3.27}
$$

The sign of the terms in the sum on the right hand side of Eq. 3.27 rapidly oscillates with z unless the argument of their exponential tends to zero. Such condition, called the phase matching condition, is verified if

$$
2\beta_0 = \frac{4\pi n_{\mathrm{eff}}}{\lambda} = 2\pi\,\frac{l}{\Lambda} \Longrightarrow \lambda = \frac{2n_{\mathrm{eff}}\Lambda}{l}
\tag{3.28}
$$

where n_{eff} is the effective refractive index of the fundamental mode. Eq. 3.28 shows clearly that for a given grating period Λ the phase matching condition can be verified for an infinite number of wavelengths. By choosing to neglect all terms not satisfying the phase matching condition for a given wavelength interval, Eq. 3.27 further simplifies to:

$$\begin{cases} \dfrac{\mathrm{d}\,\alpha_+(z)}{\mathrm{d}\,z} = -j\alpha_-(z)c_l \exp\left[jz(2\beta_0 - 2\pi\,\frac{l}{\Lambda}\right] \\[2ex] \dfrac{\mathrm{d}\,\alpha_-(z)}{\mathrm{d}\,z} = j\alpha_+(z)c_{-l} \exp\left[-jz(2\beta_0 - 2\pi\,\frac{l}{\Lambda}\right] \end{cases} \tag{3.29}$$

whose solution is:

$$\begin{cases} \alpha_+(z) = \alpha_+(0)\mathrm{e}^{j\pi l/\Lambda}\dfrac{\Delta\beta_l\,\sinh(S(z-L)) - j\,S\,\cosh(S(z-L))}{-\Delta\beta_l\,\sinh(SL) - j\,S\,\cosh(SL)} \\[3ex] \alpha_-(z) = -j\,c_l\alpha_+(0)\mathrm{e}^{-j\pi l/\Lambda}\dfrac{\sinh(S(z-L))}{\Delta\beta_l\,\sinh(SL) + j\,S\,\cosh(SL)} \end{cases} \tag{3.30}$$

with

$$\begin{gathered} \Delta\beta_l = 2\beta_0 - 2\pi l/\Lambda \\ S = \sqrt{|c_l\,c_{-l}|^2 - \Delta\beta_l^2} \end{gathered} \tag{3.31}$$

and using as boundary conditions $\alpha_+(0) = 1$ and $\alpha_-(L) = 0$. Finally, the complex reflection coefficient of the grating is given by

$$r(\lambda) = \frac{\alpha_-(0)}{\alpha_+(0)} = \frac{-j\,c_l\,\sinh(SL)}{-\Delta\beta_l\,\sinh(SL) + j\,S\,\cosh(SL)} \tag{3.32}$$

where L is the length of the FBG.

As it can be seen from Fig. 3.19, the SM FBG reflectance is quite similar to that of the VBG shown in Fig. 3.14; therefore, it is clear that the effect induced on a HPLD by the VBG can be induced by an FBG too. However, it has to be noted that the delivery fiber of HPLDs are generally highly multimode fibers, which is characterized by a reflectivity spectrum quite different from the one shown in Fig. 3.19 and much more similar to the reflectivity shown in figure Fig. 3.20. In fact, in a multimode delivery fiber there is a very large number of propagating modes so the phase matching condition can be satisfied not only by the forward and backward component of the same mode, leading to multiple reflectivity peaks at any wavelength such that

$$\lambda = \frac{2\,n^{\mathrm{eff}}_{\mathrm{n,l}}\Lambda}{l} \tag{3.33}$$

but also by the forward and backward component of different modes, which gives rise to multiple reflectivity peaks at any wavelength such that

$$\lambda = \frac{(n^{\mathrm{eff}}_{\mathrm{n,l}} + n^{\mathrm{eff}}_{\mathrm{s,t}})\Lambda}{l} \tag{3.34}$$

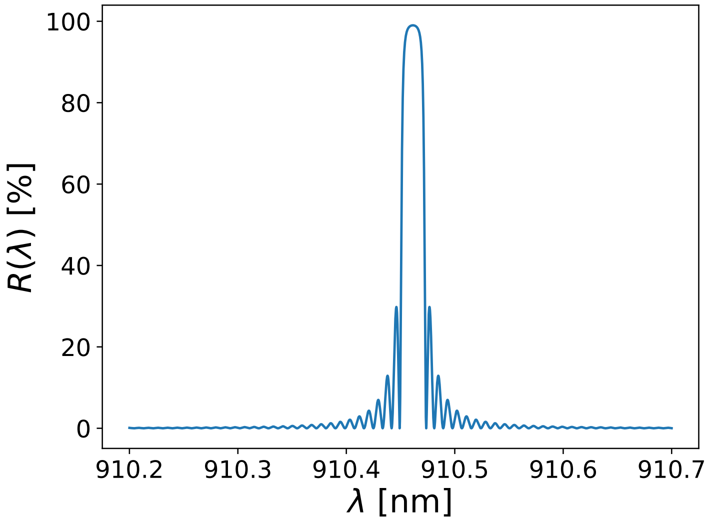

Figure 3.19: Reflectivity of an FBG in a single mode fiber computed according to Eq. 3.30 and Eq. 3.32 with a coupling coefficient equal to $100\,\mathrm{m}^{-1}$ and length equal to 30 mm.

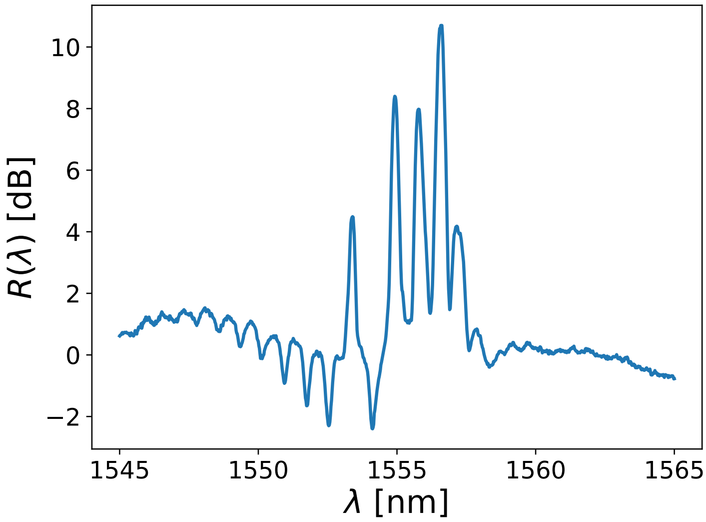

Figure 3.20: Experimentally measured reflectivity of an FBG in a 62.5 µm core optical fiber realized by femtosecond laser inscription. Due to the splice to an SMF needed to connect the FBG to the interrogation system, the reflectivity shows some spurious oscillations created by a parasitic Fabry-Perot cavity.

Therefore, each wavelength such that either Eq. 3.33 or Eq. 3.34 is satisfied can potentially corresponds to a peak in the reflectivity. As shown later in Sect. 3.3.3, the presence of these multiple reflection peaks can, sometime, be the cause of the stabilization of laser diodes in unexpected spectral ranges. Finally, the reflectivity computed solving either numerically or analytically Eq. 3.24 can substituted into the external cavity laser diode stabilization model to study the behavior of an arbitrary emitter, given its modal gain, when an FBG is used to delimit an external cavity.

3.3.2 Fiber Bragg gratings inscription by femtosecond laser pulses

Commercially available FBGs are generally inscribed into single mode fibers used for telecom applications and therefore working mostly in the 1400 nm - 1500 nm or 1300 nm - 1400 nm bands. However, to spectrally stabilize an HPLDs, these kind of commercially available FBGs are not useful at all since high power emitters are generally coupled with highly multimode optical fibers whose core diameter ranges from 50 µm to 200 µm. For this very reason, the FBGs exploited for HPLDs spectral stabilization experiment need to be custom made. Part of the following section has been already published by the author in [105].

In early times, FBG manufacturing was done by exposing the fiber to an intense UV-laser; today, a femtosecond laser is preferred. The first fiber Bragg grating inscription using a high energy femtosecond laser source was reported in 2003 [106]. This inscription process is based on the absorption phenomenon induced by focusing the femtosecond laser beam into the fiber core, which causes a highly localized deposit of energy into an electron plasma that is formed within the focal volume. This energy is then absorbed by the underlying lattice which undergoes a permanent and localized material modification (e.g., localized melting, creation of defects, material compaction, micro-void formation, nano-grating etc.), the type of modification being determined by the intensity of the laser pulse and the irradiation conditions. With respect to the FBGs induced by UV sources, the femtosecond laser induced FBGs can be inscribed in any optical waveguide through the cladding itself. This is a very important property for FBGs used in high power applications because it allows not stripping the coating off the fiber. The resulting FBGs keep the same robustness and mechanical properties of the bare fiber, avoiding possible mechanical defect that can be caused by the stripping procedure and that could lead to the formation of hot point during the laser operation and also to a particularly detrimental phenomenon known as “fiber fuse” [107].

The grating inscription process can be done either by direct writing or using a phase mask. In the former method the laser pulses are individually focused into the fibre core through a high numerical aperture microscope objective, while the fiber is translated below it with submicrometric precision by a piezoelectric stage; this approach is more critical from the point of view of the mechanical stability requirements, but it allows creating arbitrary refractive index patterns, with any periodicity. Therefore, it is particularly suited for fabricating custom FBGs in any kind of optical fiber, including the HPLD delivery fiber. On the other hand, the phase mask approach allows reducing the alignment tolerance requirement, but as different masks are required for the inscription of different FBGs, it not suited for research and prototyping activities involving the realization of many different gratings with different Bragg wavelength and optical features. Therefore, the FBGs used in the spectral stabilization experiments presented in this work have been realized using a variant of the line by line [108] inscription method with a laser micro-machining workstation from Workshop of Photonics, which is based on a femtosecond laser by Light Conversion. This micro-machining workstation consists of the femtosecond laser, a software controlled translating stage and a 100x microscope system allowing for both focusing the femtosecond laser into the fiber core and for observing the fiber core through the integrate vision system. In order to fabricate the FBGs, once it has been loaded onto the translating stage in the micro-machining workstation, the fiber must be positioned in the focus of the microscope objective by moving the translating stage through the provided software. This task is generally accomplished when the fiber core can be observed in the vision system. However, in case of very large mode area fiber, the core may even be too large to fit in the vision system field of view, leading to an wrong positioning of the optical fiber. In particular, considering the application of HPLD spectral stabilization coupled to a 105 µm core, 125 µm cladding and 0.22 numerical aperture optical fiber, the gratings have been inscribed in the core of a Double Cladding Fiber (DCF) whose inner core diameter is about 9 µm, similar to that of standard single-mode fibers used for telecommunication applications, and outer core diameter is 105 µm. The choice of the DCF is dictated by two reasons: on one hand the need of using the inner core, which can be clearly imaged by the vision system, as a reference to inscribe the grating into the center of the fiber first cladding; on the other hand the DCF first cladding matches the HPLD delivery fiber so it can be directly spliced to it in a lossless fashion.

In general, the FBG inscription process is monitored using a setup based on a supercontinuum source and an optical spectrum analyzer (OSA) coupled through a circulator and a switch, as sketched in Fig. 3.22. The supercontinuum light source is a SuperK from NTK Photonics and is characterized by a flat spectrum from about 600 nm to about 2000 nm. The SuperK is connected to the fiber sample through the circulator which can transmit light only from port 1 to port 2 and from port 2 to port 3, allowing to decouple the source signal coming from the SuperK from the reflected signal coming from the fiber sample. A SMF patch cable allows for the transmission of the light coming from the fiber sample to the OSA through one of the switch input. The other input, instead, is connected through another SMF patch cord to the third port of the circulator allowing for the collection of light reflected by the fiber sample. Clearly the fiber sample needs to be spliced at both ends to SMF pigtails before the begin of the inscription procedure. The OSA, an Agilent 86140b characterized by a spectral resolution as small as 0.06 nm, can internally store up to four different spectra and can be controlled by a LabView program from a computer to store the desired spectra. Therefore, the reflection and transmission spectra from the fiber sample can be easily saved on a computer for further processing or can be shown on the OSA screen. Depending on the inscription speed, this system can be used to acquire one or more transmission and reflection spectra during the grating fabrication, which is independently carried on by the micro-machining system, allowing for the online monitoring of the process. Fig. 3.21 shows an example of a reflection and transmission spectra acquired by the above mentioned monitoring setup of a 10 mm long line by line inscribed grating in a SMF by the micro-machining system. Clearly, the monitoring system in better suited to measure the spectra of single mode fibers. It can be extended to multi mode fibers at the cost of severe signal losses due to the core area mismatch between the single mode fibers and multi mode fibers and, when used with double cladding fibers, it is only able to measure the optical spectrum of the light transmitted through and from the DCF core.

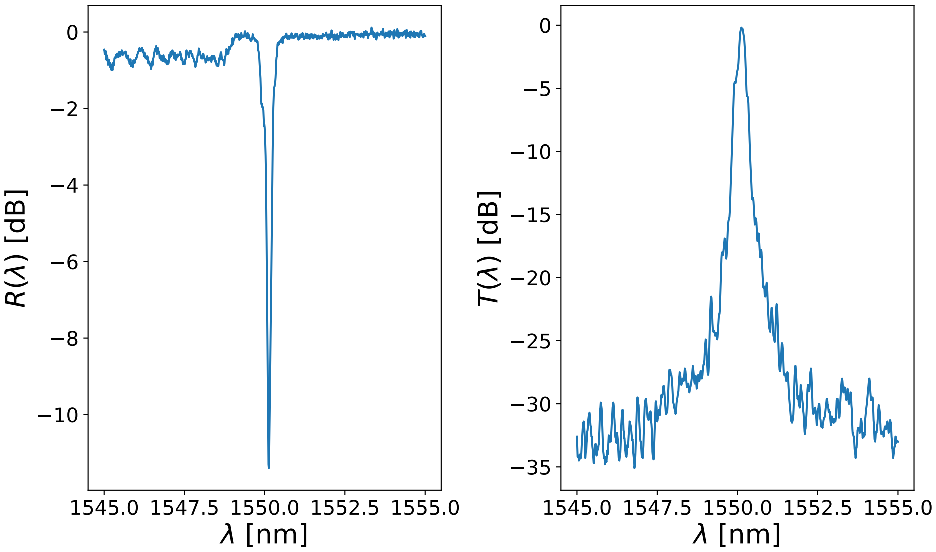

Figure 3.21: On the left: reflectivity of a 10 mm long grating inscribed in a DCF. On the right: transmittance of the same grating. Both measures have been taken using the monitoring setup detailed in this section and using as reference the transmission spectrum of the same sample fiber before the inscription.

When the DCF is spliced to high power laser diodes, only a tiny fraction of the power, of the order of $r_{core}^2/r_{first\ clad}^2$, is guided by the fiber core so the reflection and transmission spectrum taken using the aforementioned setup can only quantify the amount of light, guided by the core, transmitted through or reflected by the grating. However, since the quantity of interest for the spectral stabilization of high power

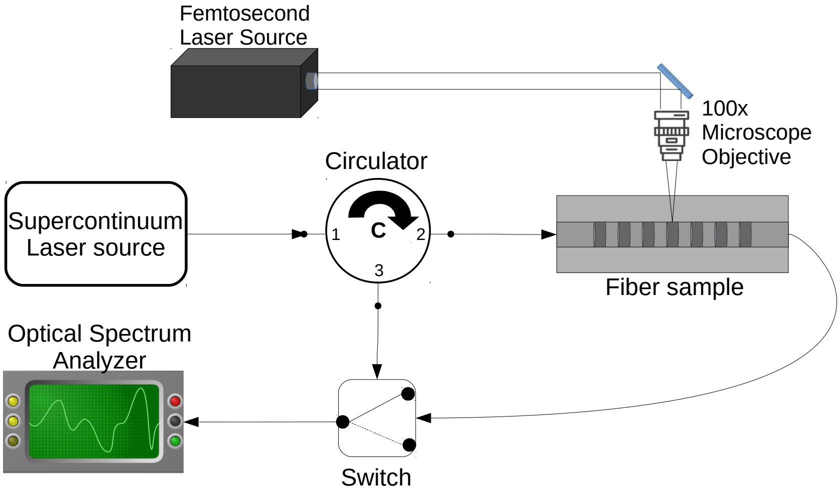

Figure 3.22: Schematic illustration of the optical setup employed for the online monitoring of the FBGs inscription procedure.

laser diodes is the amount of light reflected by the first cladding, corresponding to the amount of light fed back into the laser by the external cavity, the monitoring setup can only be used to qualitatively check weather the grating is working or not. Indeed, when the microscope is focused into the fiber core, it is possible to actually observe, in real time, the modification of the fiber refractive index induced by the femtosecond pulse as a darker spot in the fiber core. However, observing through the microscope it is not possible to tell if the refractive index modifications are actually being effective or not in producing the expected reflectivity, which can be measured only by splicing the grating to an HPLD and evaluating its effect on it. In Fig. 3.23 the results of inscription procedure can be appreciated: the refractive index modification are clearly visible as vertical darker lines, which periodically repeat along the fiber propagation axis; the boundary between the core and the first cladding, where the refractive index jumps from the the higher core refractive index to the smaller first cladding refractive index, is visible as an horizontal dark line, even if partially overlapped with the grating refractive index modulation. The inscription process induces a modification in the refractive index of the order of 10^{-4}. Performing a periodic line by line inscription extending beyond the inner core, the fiber refractive index can be described by the equation:

$$\begin{cases} n_{\mathrm{c}} = n_0 + \Delta n & 0 < x \leq \Lambda\,(\mathrm{DC}) \\ n_{\mathrm{c}} = n_0 & \Lambda\,(\mathrm{DC}) < x < \Lambda \end{cases} \tag{3.35}$$

where n_{c} is the core refractive index after the inscription process, n_0 the core original refractive index, Δn the change in the refractive index induced by the femtosecond

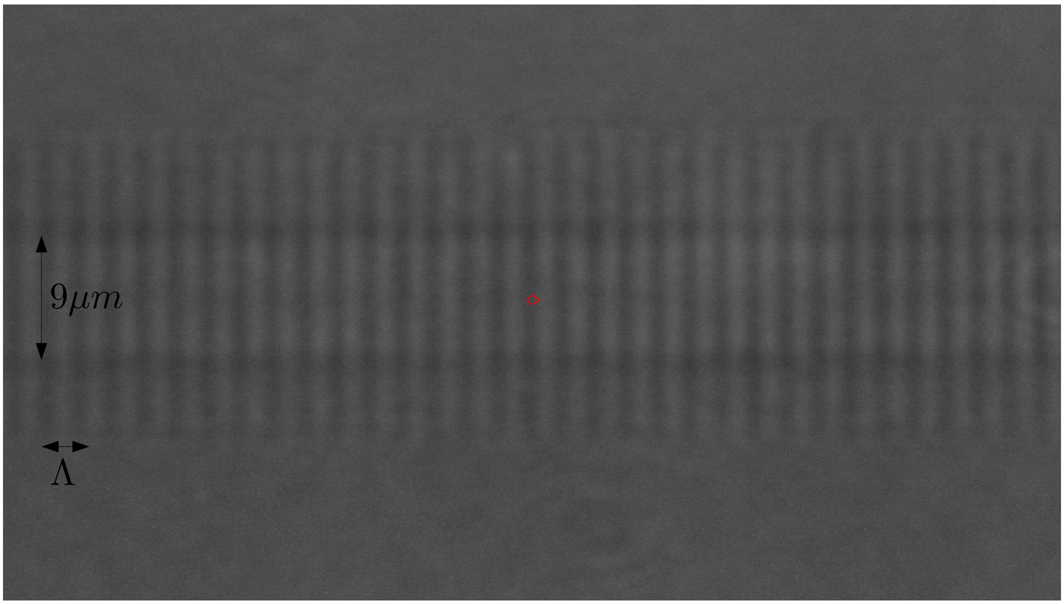

Figure 3.23: Example of a FBG inscribed by femtosecond laser pulses into a DCF fiber exploiting a line by line inscription procedure as shown by the machine vision system integrated into the micro-machining workstation

laser inscription, DC the duty cycle and Λ the period of the grating. As well known, the Bragg wavelength λ_B is given by Eq. 3.33:

$$\lambda_B = 2n_{\text{eff}}\,\Lambda \tag{3.36}$$

where n_{eff} is the effective refractive index of the fiber, which in turns depends on Δn and DC.

3.3.3 Experimental results

The spectral stabilization with FBGs has been experimentally demonstrated using 105 µm fiber coupled Fabry-Perot laser chips by Oclaro (BMU10A-915-01-R). The measurment setup, schematically shown in Fig. 3.24, makes use of a temperature controlled cold plate on which the diode under measure is mounted using some thermal paste to reduce the thermal impedance at the interface between the emitter and the cold plate. The setup is then completed by a power meter (Thorlabs S322C) with a resolution of 0.1 mW over a dynamic of 100 W, a spectrometer (AvaSpec-ULS2048CL-EVO from Avantes) characterised by a resolution of 0.5 nm, a thermistor (EPCOS B57861S0103F040, from NTK) to measure the temperature of the emitter package with a resolution of 0.1 K, and a laser driver (LDP-CW 20-50 from Picolas) able to inject current with an accuracy of 0.1 A. The whole setup is controlled by a Labview script that can perform measurements varying the current

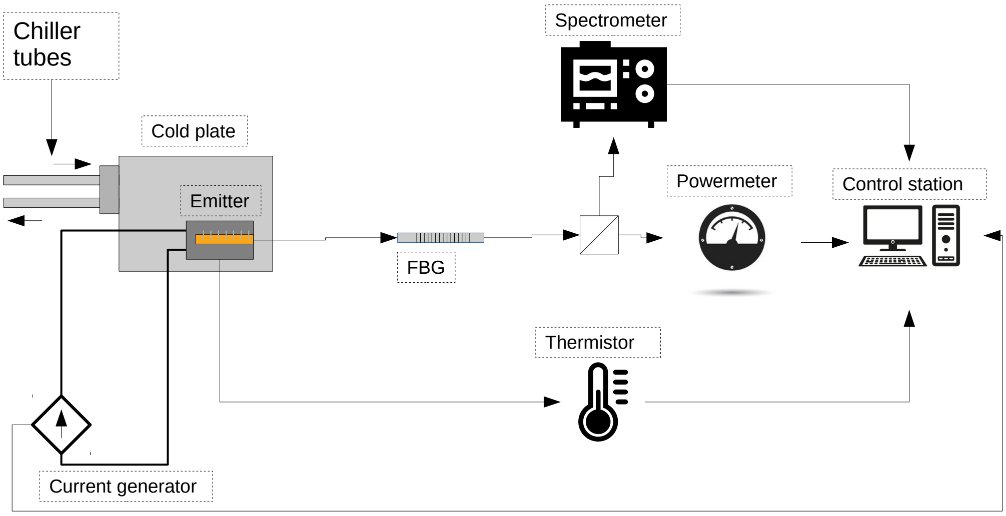

Figure 3.24: Schematic illustration of the spectral stabilization setup.

but keeping the temperature constant or varying the temperature while keeping the current constant.

As it can be seen from Fig. 3.25 and Fig. 3.26, the considered emitters are able to deliver up to 9 W in CW at a driving current of 11 A. As the driving current increases from 1 A to 11 A, the full width at half maximum ranges from 2 nm to 4 nm, the peak wavelength ranges from 905 nm to 920 nm, and the spectral efficiency η_s, defined as

$$\eta_\mathrm{s} = \frac{\displaystyle\int_{\lambda_\mathrm{peak}-1\,\mathrm{nm}}^{\lambda_\mathrm{peak}+1\,\mathrm{nm}} P(\lambda)\,\mathrm{d}\lambda}{\displaystyle\int_{\infty}^{\infty} P(\lambda)\,\mathrm{d}\lambda} \tag{3.37}$$

which is the fraction of power enclosed in a 2 nm interval around the peak wavelength, ranges from 0.7 to 0.4. The emitter shows a peak wavelength shift at constant temperature equal to about $0.3\,\mathrm{nm\,K^{-1}}$, which is compatible with the thermal peak wavelength shifts for other HPLDs reported in the literature.

As already pointed out, the FBGs used for the experimental validation have been inscribed in a DCF fiber (DCF13 from Thorlabs) using a repeated line by line technique. Letting the y direction to be the incidence direction of the femtosecond laser pulse, the z direction the fiber propagation axis, and the x direction the remaining direction perpendicular the y and z directions, this technique consist in inscribing several different lines along the x direction one above the other at a variable distance along the y direction and then to repeat the whole inscription process periodically along the z direction. An example of the result of this kind

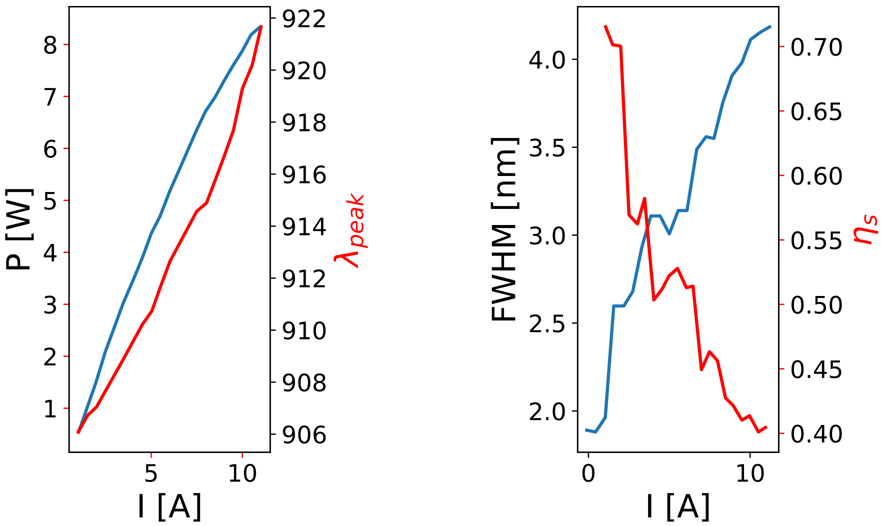

Figure 3.25: Characterizations of the “as is” considered Oclaro diode. Left: peak wavelength (in red) and emitter output power (in blue) versus the driving current; right: FWHM (in blue) and spectral efficiency (in red) versus the driving current.

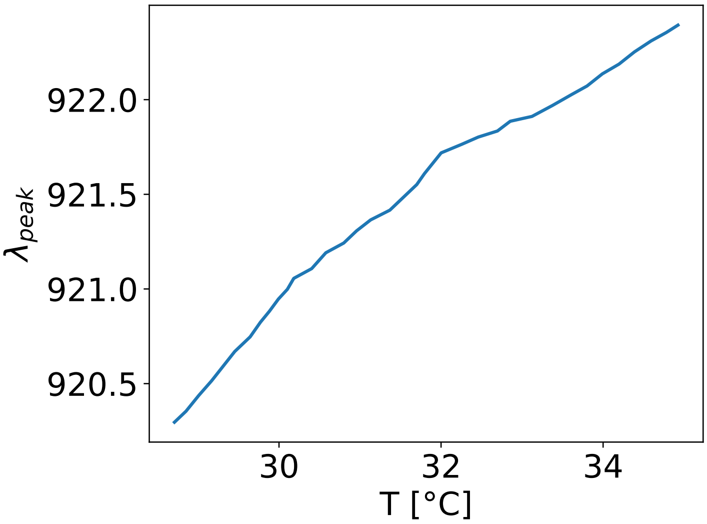

Figure 3.26: Peak wavelength of the Oclaro diode versus the temperature at a fixed injected current equal to 10 A.

of fabrication technique is shown in FIg. 3.23 The refractive index modification induced by a single femtosecond pulse follows a somehow radially hat distribution that can be well approximated by a stigmatic Gaussian distribution [109, 110]. Its characteristic radius is equal to about 1 µm in the plane perpendicular to the femtosecond pulse incidence direction and 3 µm to 4 µm along the remaining direction. Being so, the repeated inscription of multiple lines along the y direction generates a refractive index modification that increases the coupling coefficient between modes and therefore increases the reflected electromagnetic wave intensity. This inscription methods presents a large number of parameters, such as the femtoscond pulse energy and temporal width, the length of a single inscribed line, the distance between lines and so on and so forth, which is why a large number of gratings has been fabricated and tested in order to tune the fabrication process. Then the actual spectral stabilization tests, which are presented in the following of this subsection, have been performed.

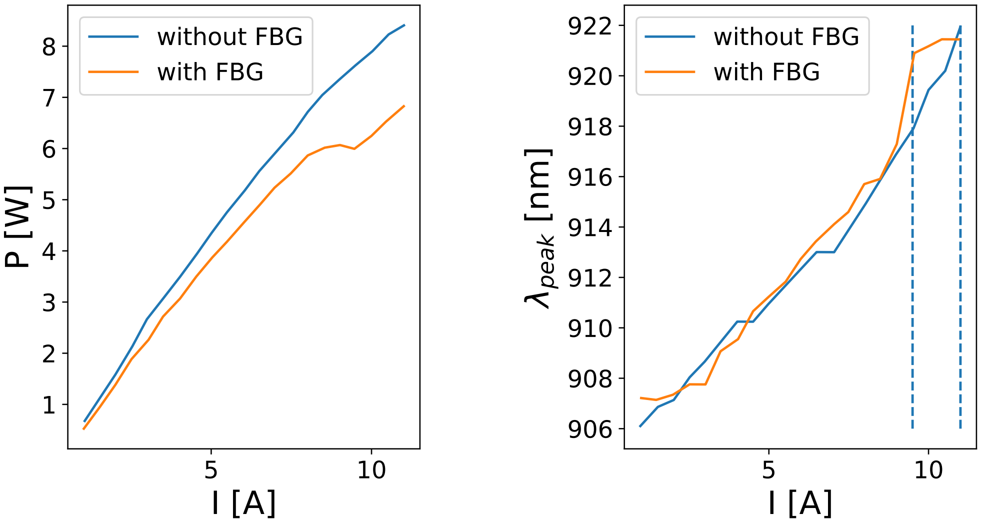

Figure 3.27: Characterizations of the considered Oclaro diode. Left: a comparison between the delivered optical power with and without the FBG reflecting at 920 nm versus the driving current; right: the emitter peak wavelength, with and without the FBG reflecting at 920 nm, versus the driving current.

The first spectral stabilization test has been executed with a 20 mm long, third order FBG whose Bragg wavelength is 925 nm. As it can be seen from Fig. 3.27 and Fig. 3.28, it is clear that the HPLD is spectrally stabilized around the grating Bragg wavelength only for a small interval of driving currents, which is underlined by the dashed blue lines, ranging from 9.5 A to 11 A. In this driving current interval, indeed, it can be seen a reduction of at most of the 12% of the emitted power, shown in Fig. 3.27, and, however, an increase of the spectral efficiency, which means a decrease of the 95% spectral width of the emitter. The peak wavelength stability with respect to an increase of the emitter temperature, shown in Fig. 3.28, further confirms the emitter spectral stabilization by the FBG. It is worth noticing that

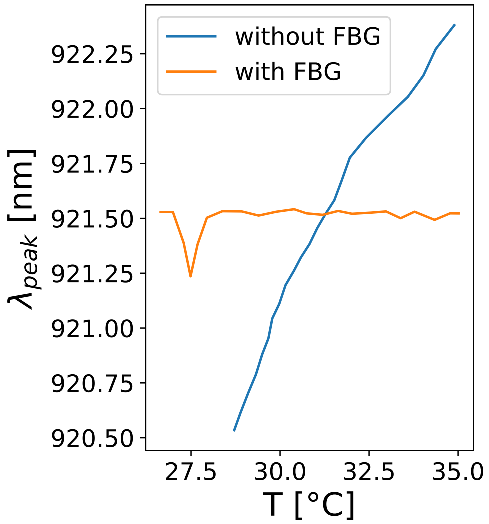

Figure 3.28: Characterizations of the considered Oclaro diode. Left: a comparison between the spectral efficiency, with and without the FBG reflecting at 920 nm versus the driving current; right: comparison between the peak wavelength with and without the FBG reflecting at 920 nm shift versus the emitter temperature at a driving current equal to 9 A.

it is very probable that the actual driving current stabilization interval extends beyond the maximum driving current used for this emitter; this hypothesis can be supported also by the very large temperature range in which the spectral stability condition holds, as shown in Fig. 3.28.

A second spectral stabilization test has been carried out with a third order, 18 mm long FBG, whose Bragg wavelength is equal to 915 nm. It can be seen from Fig. 3.29 that also in this case the spectral stabilization occurs only in a small interval of currents, as highlighted by the blue dashed lines in the right plot of Fig. 3.29. The occurrence of the spectral stabilization is further supported by the measurement of the spectral efficiency, which shows a spike in the same driving current range for which the peak wavelength remains constant, as shown in Fig. 3.30. Finally, in Fig. 3.30 it is shown that the emitter peak wavelength remains essentially constant over a large temperature interval, a behavior that is a sure signature of the spectral stabilization. Compared to the previous stabilization case, it is worth noticing the reduction of power loss, which in this case is no larger than 10%.

To the best of the author's knowledge, this is the first time that a HPLD has been spectrally stabilized, even if only for a small driving current range, thanks to an FBG inscribed by femtosecond laser pulses, hence few consideration are in order. Due to the multimode optical fiber, the FBG reflection spectrum has a main

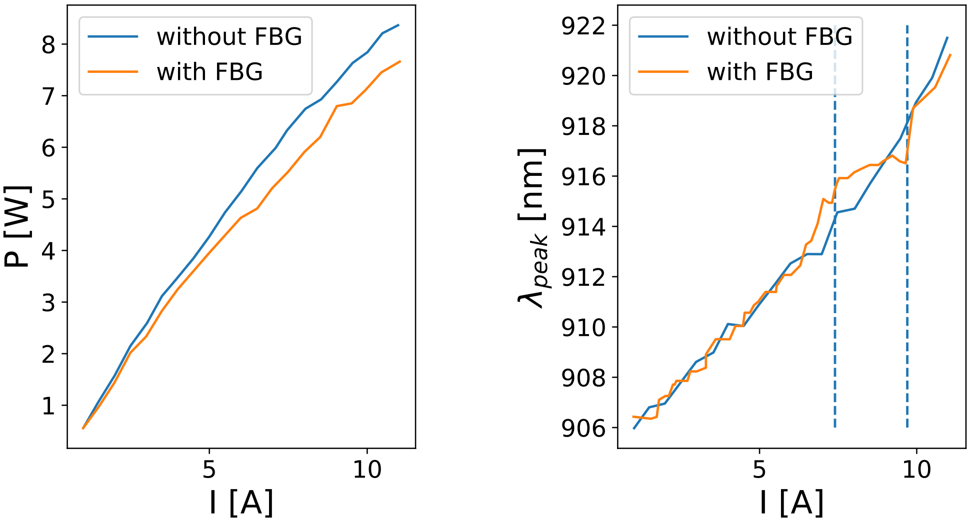

Figure 3.29: Characterizations of the considered Oclaro diode. Left: a comparison between the delivered optical power with and without the FBG reflecting at 915 nm versus the driving current; right: the emitter peak wavelength, with and without the FBG reflecting at 920 nm, versus the driving current.

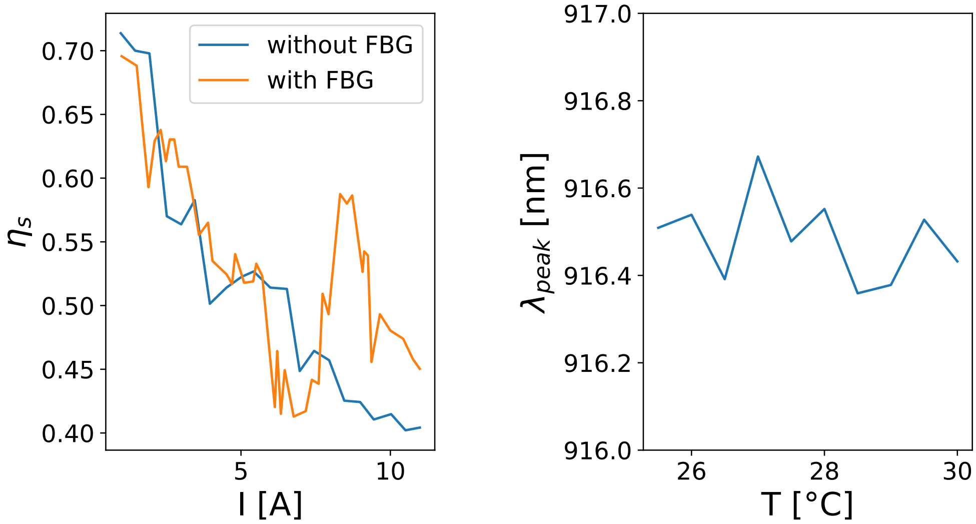

Figure 3.30: Characterizations of the considered Oclaro diode. Left: a comparison between the spectral efficiency, with and without the FBG reflecting at 915 nm versus the driving current; right: peak wavelength of the emitter stabilized by an FBG reflecting at 920 nm shift versus the emitter temperature at a driving current equal to 8 A.

reflectivity peak at the Bragg wavelength for the fundamental mode and other multiple minor peaks at shorter wavelengths. Despite the FBG being few tens of millimeter long, the driving current interval where the FBG is spectrally stabilized is no larger than 3.5 A, which corresponds to a rather small temperature interval where the FBG is stabilized. According to the theory detailed in Sect. 3.1.1, these experimental data suggest that the FBG maximum reflectivity is not larger than few percents. However, the data are remarkable since they pave the way for a new, cheap and flexible method to spectrally stabilize HPLDs. Indeed, considering that the femtosecond laser technology allows the inscription of any kind of FBG in an arbitrary fiber without the need of stripping or mechanically weaken the optical fiber, the advantages of using FBGs instead of VBGs are clear: cost reduction and flexibility, thanks to the use of the direct writing technique. Moreover, it has to be considered that the FBG peak wavelength can be easily tuned by applying some strain without any bending that could cause an additional power loss. Being so, an FBG can be used, potentially, to tune the output wavelength of an HPLD, a feature that cannot be replicated by VBGs.

Chapter 4

Spectral multiplexing

As illustrated in the introductory chapter, there clearly is a requests for more efficient and powerful laser systems in many application fields. From a purely theoretical point of view, the best approach to satisfy these requests would be a massive exploitation of the CBC, detailed in Ch. 2, since the CBC would allow multiplexing together an arbitrary number of laser beams into a single brighter beam while preserving the quality of the combined beam. However, compared to other multiplexing approaches, such as the spatial and the polarization multiplexing, the CBC approach is way more complex to implement and hence it is much more expensive, mostly because it makes use of expensive specialized hardware and it requires laser sources with extremely stable phase. A quite less expensive class of high power lasers is the class of HPLDs, which, however, are limited to a maximum power in CW of about 20 W [111], but with an electro-optical efficiency ranging from 50% to 60%, being defined as

$$\eta_{\mathrm{EO}}(I) = \frac{P_{\mathrm{optical}}(I)}{P_{\mathrm{electrical}}(I)} = \frac{P_{\mathrm{optical}}(I)}{V_{\mathrm{diode}} I} \tag{4.1}$$

where P_{optical} is the optical power emitted by the laser diode, V is voltage across the diode and I is the injected current. Indeed, the increase of popularity of the fiber lasers recorded in the last 15 years is also due to the improvement of the output power of a single HPLDs and of HPLD modules, used to optically pump fiber lasers. A HPLD module is an architecture aiming at multiplexing a multitude of HPLDs into a single laser beam delivering an amount of power that scales as the number of emitters involved, and generally coupled to an optical fiber for power delivery. The combined emitters are customarily multiplexed using the beam stacking technique, also known as spatial multiplexing, and the polarization multiplexing [112]. The beam stacking technique consists in stacking, along a single direction, several collimated laser beams, as shown in Fig. 4.1. The resulting beam is then focused into a delivery optical fiber, which is mostly a multi-mode fiber (MMF). The implementation simplicity of this method, which in principle allows for an arbitrary

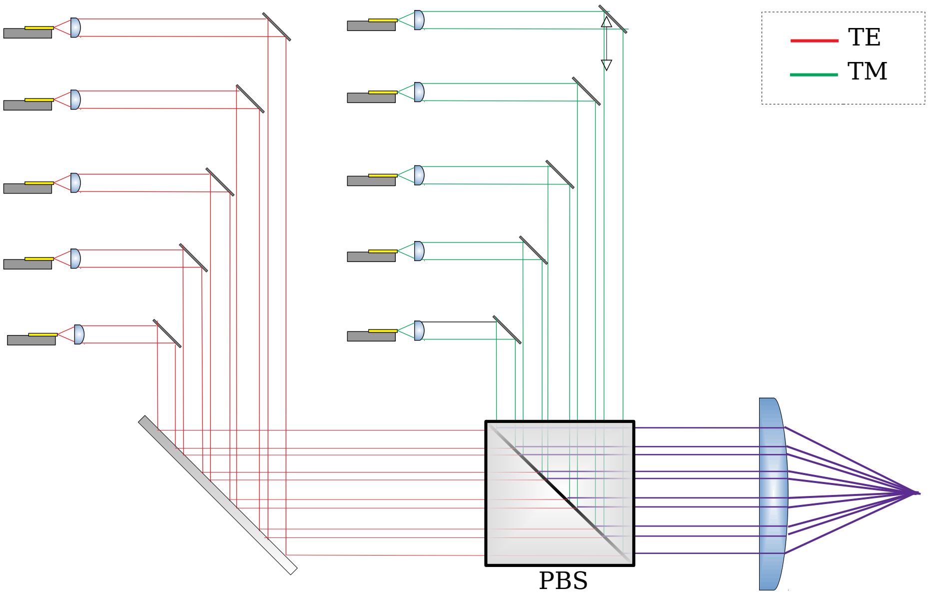

Figure 4.1: Schematic representation of a HPLD multiplexing architecture that exploits spatial and polarization multiplexing. Two sets of HPLDs are firstly collimated and the beams of each stack are spatially combined using mirrors; then, the two sets are overlapped using a Polarization Beam Splitter (PBS).

number of beams to be multiplexed together, is balanced out by the degradation of the resulting beam NA. Indeed, if the combined beams share, once collimated, the same beam size, then, referring to Fig. 4.1, the resulting beam size will roughly be $h_{\mathrm{CLD}} \times N w_{\mathrm{CLD}}$, hence the beam NA, once focused by the focusing system, will increase as the number of combined emitter increases along the stack direction and will remain unchanged along the other perpendicular direction. As discussed in Ref. [23], in order to guarantee an almost lossless fiber coupling, the resulting beam NA must be smaller than or equal to the delivery fiber NA, which can be put as the upper bound for the combined beam NA. The naive solution would be to choose a focusing system having a larger focal length. In fact, it would decrease the beam NA but also increase the magnification, resulting in a larger beam size on the optical fiber facet, which would cause part of the power to be coupled into the fiber cladding instead of the fiber core, leading again to a lossy fiber coupling. Therefore, these two constraints are what actually limits the number of laser diodes that can be spatially multiplexed.

The other multiplexing method largely used in HPLDs architecture is the polarization multiplexing. The polarization multiplexing method exploits one of the basic properties of light, that is polarization: any electromagnetic wave in free space can be decomposed in two orthonormal polarization components [41] – known as TE (or s) and TM (or p) components – that can be manipulated and recomposed into a single beam using proper optical components such as polarization beam splitters. Defining the degree of polarization DoP as

$$DoP = \frac{P_\nu}{P_{\mathrm{tot}}} \tag{4.2}$$

where $\nu \in$ TE,TM, P_ν is the power carried by the ν polarization and P_{tot} is the total power carried by the beam, and assuming that the beams are almost completely ν-polarized, namely $DoP \simeq 1$, then the two beams can be completely overlapped in space without any beam quality degradation using a polarization rotation plate to rotate one of the two beams polarization by 90° and a PBS, resulting in a beam having exactly the same quality as the combined beams but a twofold increase in optical power. The major advantage of the polarization multiplexing is that it can be used just as easily on the spatial multiplexing resulting beam, as shown in Fig. 4.1, allowing doubling the HPLD optical power. The drawback is that it can be exploited only once; therefore, it is preferable to use it as the last multiplexing level.

It is evident that, in order to further scale up the optical power delivered by a HPLD module, a new multiplexing level has to be used. A different approach, not discussed so far, is the spectral multiplexing. Just like beams having perpendicular polarization can be combined by polarization beam splitters, also beams having different wavelength can be combined together by means of dichroic mirrors [113]. Dichroic mirrors are basically wavelength filters able to transmit and reflect only selected wavelengths. Exploiting such optical elements, spectral multiplexing allow for the combination of an arbitrary number of beams, virtually in a lossless fashion and avoiding the beam quality degradation typical of the beam stacking technique, at the cost of an increase of the resulting beam spectral width, a condition that can or cannot be accepted depending on the target application. The remaining of this chapter is organized as follows: is Sect. 4.1 a WOF-based model for multiemitter simulation aided design is presented along with its experimental validation; in Sect. 4.2 a statistical model based on experimental data of HPLDs for dichroic mirrors design is illustrated; in Sect. 4.3 the design and experimental data of a 400 W HPLD module based on DBR-HPLDs is presented; in Sect. 4.4, the design and experimental results of a 400 W multiemitter module based on externally stabilized HPLDs are presented.

4.1 WOF-based model for multiemitter simulation-aided design

As already pointed out, multiemitter modules exploit mostly beam stacking and polarization multiplexing to combine together a large number of HPLDs into a single beam and then couple it to a delivery optical fiber. From an implementation point of view, the concept behind spectral multiplexing is quite similar to the concept of polarization multiplexing: two beams, typically resulting from beam stacking of HPLDs, each one having a well defined wavelength, are spatially overlapped by means of a dichroic mirror, resulting in a beam carrying the sum of the combined beam optical power, but having the same NA and beam size of the individual beams. Unfortunately, the emitted spectrum becomes equal to the sum of the combined beam spectra. Clearly, each level of multiplexing brings its own set of optical elements that must be carefully chosen, keeping also into account the characteristics of the beams coming from the diode, in order to optimize not only the multiemitter module output power, but also the beam quality. In terms of computational effort, the easiest method for the design of a multiemitter module is the ray tracing method. This method treats any laser beam as an envelope of rays whose trajectory is determined by the eikonal equation [42]. Despite the reduction of the propagation of light to a matrix multiplication problem makes this method easy to be implemented, neglecting the wave nature of light poses some important limits on its applicability, particularly in the computation of the field in the focal plane of the focusing lenses. These limits can be partially overcome by the so-called “five rays model” [43], which approximates any beam with a gaussian beam whose propagation through an optical system can be described by a transfer matrix. This method too does not require an important computational effort, but the approximation to a gaussian beam can be fairly inaccurate in some practical frameworks, such as in the evaluation of the probability of a lens catastrophic failure due to the optical filamentation of the HPLD slow axis profile. A possible trade-off between accuracy of the model and computational effort is represented by those models based on wave optics. To model a multiemitter using a wave optics based approach, firstly the output field of the HPLD must be expressed as a complex amplitude function that can lately be propagated through an optical path and coupled to the delivery fiber. A rigorous model of the HPLD would require the numerical resolution of the associated rate equations, coupled to a non linear propagation algorithm, such as the beam propagation method, in order to take into account the thermal and non linear effects that give rise to the optical filamentation [114, 94, 95, 96]. While rigorous, this approach would be time-expensive, since the coupling between the rate equation and the beam propagation method may not converge and be extremely dependent on the microscopic features of the HPLDs, such as the semiconductor doping levels. Considering that these data are not public and the need of a method that is not computationally expensive, a HPLD beam model taking only into account the macroscopic and known diode features has been adopted. Generally, such features include only the geometry, the dimensions and the base material of the HPLDs. It should be recalled that HPLD have a strongly asymmetric form factor due to its width being generally two orders of magnitude larger than its depth. Due to this geometry, the HPLD field is highly multimode along the slow axis because of the very large width and almost single mode along the fast axis along being its depth generally equal to about 1 µm. Therefore, in a macroscopic model the HPLD can be efficiently described in terms of a suitable superposition of the modes of an equivalent rectangular waveguide along the slow axis times a gaussian profile along the fast axis:

$$\begin{gathered}\vec{E}_j(x,y,0) = \vec{e}\,A_0\,\phi_{\mathrm{SA,j}}(x,0)\,\phi_{\mathrm{FA}}(y,0)\\ \phi_{\mathrm{SA,j}}(x,0) = \sum_{i=0}^{N} c_{\mathrm{i}}\,u_{\mathrm{i}}(x,0)\,\mathrm{e}^{j\beta_{\mathrm{i}}L_{\mathrm{j}}}, \qquad \sum_{i=0}^{N}|c_{\mathrm{i}}|^2 = 1\\ \phi_{\mathrm{FA}}(y,0) = \mathrm{e}^{-\frac{y^2}{w(0)_{\mathrm{y}}^2}}\end{gathered} \tag{4.3}$$

where $\vec{e}$ is the polarization vector, $u_{\mathrm{i}}(x)$ are the rectangular waveguide modes [115] shown in Fig. 4.2, L_{j} is a random propagation distance depending on the laser diode profile realization, N is the number of guided modes of the waveguide, c_{i} are random real numbers extracted from a uniform distribution and $w_{\mathrm{y}}(0) = h_{\mathrm{ridge}}$ is the gaussian beam size in the origin of the system. The slow axis divergence is de-

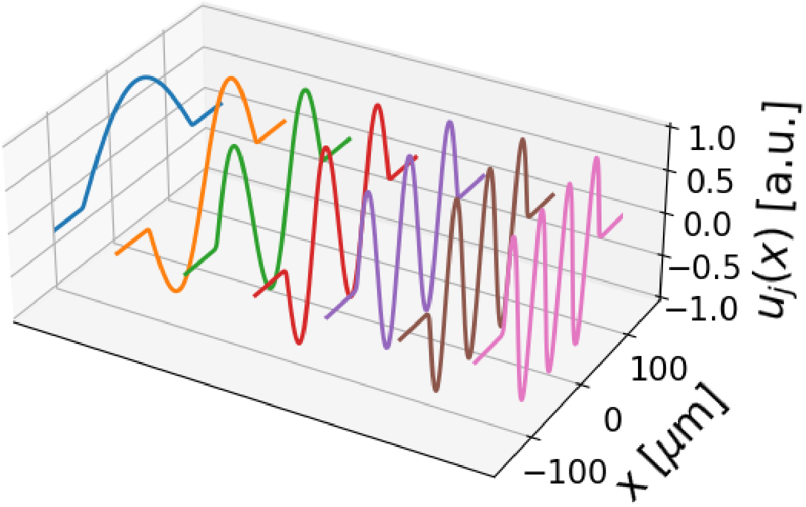

Figure 4.2: Representation of the first 7 out of 35 guided modes of a 190 µm wide slab waveguide, for a substrate refractive index of 3.5096 and a core-cladding refractive index difference of 1.25×10^{-3} at a wavelength of 976 nm.

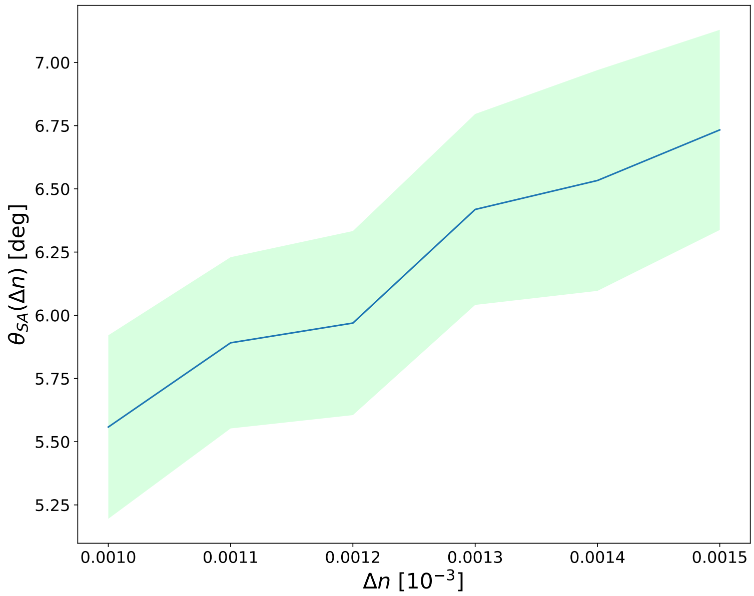

Figure 4.3: Slow axis divergence versus the core-cladding refractive index difference Δn for the slab waveguide considered in Fig. 4.2.

termined by the HPLD geometry, substrate refractive index n_{cl} and core-substrate effective refractive index difference δn_{eff}, as shown in Fig. 4.3, while the fast axis divergence is solely related to the ridge height h_{ridge}. In reality, the HPLDs SA profile changes in time, a phenomenon known as filamentation [116], due to thermal effect and residual strain from soldering the laser diode on its carrier. Indeed, in working conditions, the HPLD thermal profile changes over time, causing the semiconductor refractive index to lose its homogeneity due to its thermo-optical properties. In turn, it leads to a coupling among the propagating modes that, in homogeneous conditions, would not exchange energy one to another. In addition, the soldering process induces some localized strain in the semiconductor which further increases the non-homogeneity of the refractive index due to the photoelastic effect. Combined together, these phenomena are responsible of the SA filamentation. In the adopted HPLD model, this effect can be taken into account allowing for a lack of coherence between the equivalent waveguide modes; therefore the beam intensity at any point is given by an incoherent average of N_{r} HPLD profiles:

$$\begin{aligned} I(x,y,z) &= \sum_{\mathrm{j}=0}^{N_{\mathrm{r}}} |E_{\mathrm{j}}(x,y,z)|^2 = \\ &= |A_0|^2 |\phi_{\mathrm{FA}}(y,z)|^2 \frac{1}{N_{\mathrm{r}}} \sum_{\mathrm{j}=0}^{N_{\mathrm{r}}} |\phi_{\mathrm{SA}}(x,z)|^2 \end{aligned} \tag{4.4}$$

Given the complex amplitude describing the HPLD field, the next step consists in the simulation of the propagation through its optical path. For a multiemitter module, the optical path is composed mostly of homogeneous space, lenses and mirrors, either selective in polarization or wavelength or not, whose effect and modeling has already been discussed in detail in Sect. 2.2.1.

Finally, the coupling between the propagated beam and the delivery fiber can be computed to estimate the beam to fiber coupling loss. In particular, in the case of multiemitter modules, the HPLD beams are incoherently coupled to the delivery fiber, thus each beam coupling can be computed independently. Given the fiber core radius r_{co}, the core refractive index n_{co} and the cladding refractive index n_{cl}, the x component of the guided electric field is a sum of Linearly Polarized (LP) modes [101]:

$$\begin{gathered}\vec{\mathcal{E}}^{\,\mathrm{guided}}(x,y,z) = \sum_{\nu,\mu} A_{\nu,\mu}\vec{\mathcal{E}}_{\nu,\mu}(x,y)\,\mathrm{e}^{j\beta_\nu z} \\ \vec{\mathcal{E}}_{\nu,\mu} = \hat{\mathrm{u}}\left\{\begin{array}{lll} J_\mu(\kappa_\nu r) & \text{if} & r \le 1 \\ K_\mu(\gamma_\nu r) & \text{if} & r > 1 \end{array}\right\}\left\{\begin{array}{l} \sin(\mu\phi) \\ \cos(\mu\phi) \end{array}\right\}\end{gathered} \tag{4.5}$$

$$\kappa_\nu = \frac{2\pi}{\lambda}\sqrt{n_{\mathrm{co}}^2 - n_\nu^2}, \quad \gamma_\nu = \frac{2\pi}{\lambda}\sqrt{n_\nu - n_{\mathrm{cl}}^2} \tag{4.6}$$

where $\hat{u} \in \{\hat{x},\hat{y}\}$, $A_{\mu,\nu} \in \mathbb{C}$ is the coupling coefficient, J_μ and K_μ are, respectively, the Bessel function and the modified Bessel function of first kind and order μ, $r = \sqrt{x^2+y^2}/r_{\mathrm{co}}$ is a normalized radial coordinate, $\phi \in [0,2\pi]$ is the azimuthal coordinate and n_ν is the ν-th modal refractive index For i-th realization of the j-th HPLDs in the stack, the coupling coefficient is

$$A^{\mathrm{i,j}}_{\nu,\mu} = \tau_{\mathrm{i}} \int \mathrm{d}x\,\mathrm{d}y\,\vec{\mathcal{E}}^{LD}_{\mathrm{i,j}}(x,y) \cdot \vec{\mathcal{E}}^{F}_{\nu,\mu}(x,y) \tag{4.7}$$

where $\tau_{\mathrm{i}} < 1$ is the transmission coefficient at the interface between the fiber facet and air experienced by the i-th stacked diode [117]. Finally, the guided power P_{guided} and the Beam to Fiber Coupling Losses (BFCL) L_{BFCL} can be computed as follows:

$$P_{\mathrm{guided}} = \frac{1}{N_{\mathrm{r}}}\sum_{\mathrm{j}=1}^{N_{\mathrm{r}}}\sum_{\mathrm{i}=1}^{N_{\mathrm{d}}}\sum_{\nu,\mu}|A^{\mathrm{i,j}}_{\nu,\mu}|^2 \tag{4.8}$$

$$L_{\mathrm{BFCL}} = \frac{P_{\mathrm{guided}}}{\sum_{\mathrm{i}=1}^{N_{\mathrm{d}}} P_{\mathrm{i}}} \tag{4.9}$$

where N_{d} is the number of stacked HPLDs and P_{i} is the power emitted by the i-th stacked diode. The model described above has been validated against experimental measurements on a set of HPLDs emitting at 976 nm. The HPLDs are characterized by a ridge height of 1.5 µm, a ridge width of 190 µm, a measured FA divergence angle θ_{FA} equal to 26.6° with a standard deviation of 1.81° and a SA divergence θ_{SA} equal to 5.6° with a standard deviation of 0.79°. As shown in Fig. 4.4, a HPLD propagates through an optical path formed by two collimating cylindrical

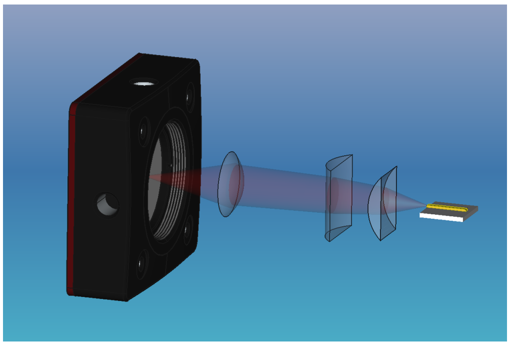

Figure 4.4: Validation setup consisting of two cylindrical lenses, one spherical lens and a CMOS camera.

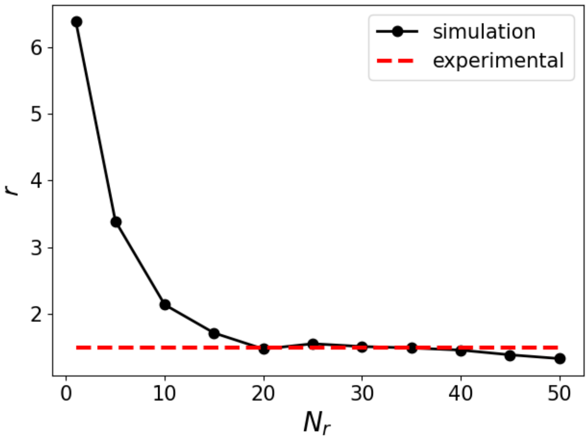

Figure 4.5: Simulated optical filamentation as a function of the number of realizations used to build the HPLD slow axis profile; r is defined as the ratio $\frac{\mathcal{I}_{\mathrm{SA}}^{\max}}{\bar{\mathcal{I}}_{\mathrm{SA}}}$, being $\bar{\mathcal{I}}_{\mathrm{SA}}$ and $\mathcal{I}_{\mathrm{SA}}^{\max}$ the average and maximum HPLD intensity along the slow axis.

lenses having respectively 0.3 mm and 12 mm focal length, a focusing spherical lens with a 250 mm focal length located 250 mm from the second cylindrical lens and is collected by a high resolution CMOS camera positioned in the spherical lens focal plane. Based on the beam intensity recorded by the CMOS camera, the beam size enclosing 80% of power is on average equal to 4.01 mm along the SA and 1.35 mm along the FA. A set of simulations using the aforementioned method has been carried out to compare the numerical results with the experimental ones. The model parameters are: i) the FA Gaussian beam waist, which has been extracted from a Gaussian distribution of mean equal to 0.85 µm and standard deviation equal to 0.02 µm and is essentially equal to half of the ridge height; ii) the equivalent waveguide width equal to the ridge width, namely 190 µm; iii) a core-substrate effective refractive index difference δn_{eff} equal to 10^{-3}; iv) a substrate refractive index equal to 3.5096, namely the GaAs refractive index. The simulated 80% beam size is on average 3.7 mm for the SA and 1.29 mm for the FA, showing a difference with respect to the measured one equal to 7.7% along the SA and 4.7% along the FA. This small deviation from the experimental measurements may be explained by systematic errors in the experimental setup, namely the CMOS camera quantization error and errors in the positioning and alignment of the optical elements which are not included in the simulations. A further validation of the empirical model of the slow axis profile has been carried out. As it can be seen from Fig. 4.5, the ratio r between the maximum intensity and the average intensity of the simulated HPLD profile, which is a measure of the optical filamentation, reaches a stationary value in excellent agreement with the measured one on the same class of IR diode. This result is quite remarkable since the HPLD profile is generate relying only on few macroscopic properties of the laser itself. Finally, an analysis of the BFCL has been performed. Customarily, the coupling loss is evaluate with a rule of thumbs in terms of the coupled beam NA and spot size at the optical fiber input facet. On the one hand, qualitatively speaking, in order to guarantee a good coupling, the beam NA, which in terms of geometrical optics is the maximum angle a ray belonging to the beam can show, must be smaller than the fiber NA. On the other hand, quantitatively speaking the losses are given as:

$$L_{\text{area}} = \frac{\displaystyle\int_{\mathrm{x}^2+\mathrm{y}^2<\mathrm{r}_{\text{core}}^2} \mathrm{d}x\mathrm{d}y \, |E(x,y)|^2}{\displaystyle\int \mathrm{d}x\mathrm{d}y \, |E(x,y)|^2} \tag{4.10}$$

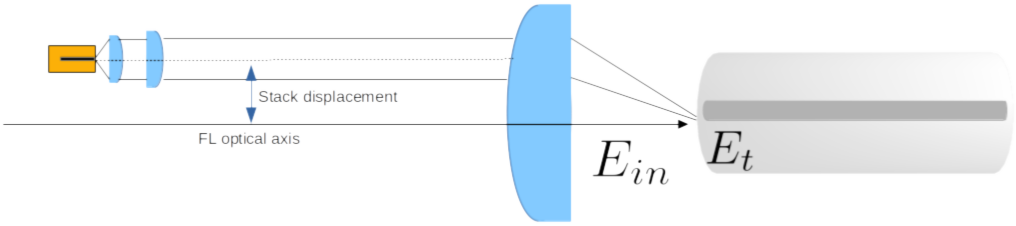

Figure 4.6: BFCL analysis setup. A laser diode is collimated by means of two cylindrical lenses and the focused by a spherical lens in order to couple it with an optical fiber.

The simulated setup, shown in Fig. 4.6, consists of a laser diode, off axis with respect to the optical axis by a variable distance, characterized by a ridge of 190 µm, a FA divergence of 59° and a wavelength of 976 nm, collimated by two cylindrical lenses and focused by a spherical lens into a multimode optical fiber with a core diameter of 200 µm, a core refractive index of 1.457 405, a cladding refractive index

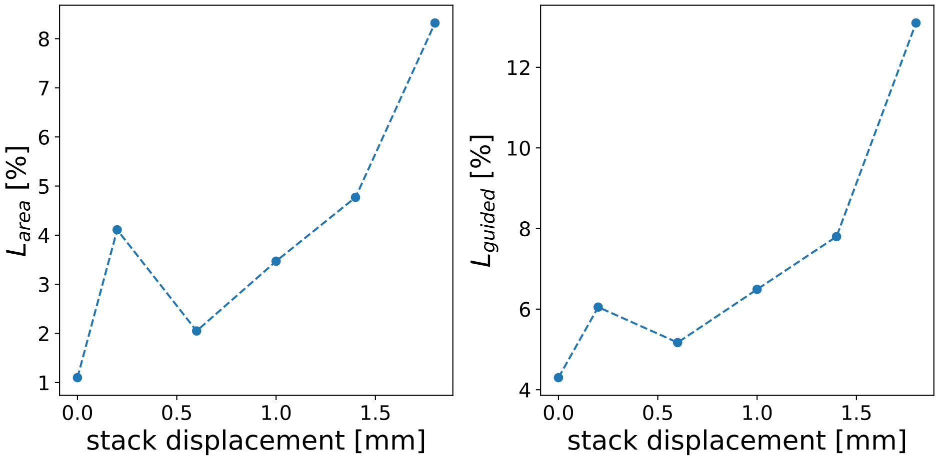

Figure 4.7: Analysis of the BFCL: on the left, L_{area}, on the right L_{BFCL}, both as function of the stack displacement as in Fig. 4.6. The average L_{BFCL} losses is about 7%.

of 1.439 44 and an NA of 0.22. As it can be seen in Fig. 4.7, both L_{area} and L_{BFCL} increase as the laser offset increases, although in a slightly different way, with L_{BFCL} showing an additional 4% of losses due to the beam reflection at the interface between the fiber and the air that may be removed using an anti reflection coating. For a beam offset greater or equal than 1.4 mm the beam NA becomes greater than the fiber NA, leading to a clear increase of loss that would be lower than 10% with a proper anti reflection coating. The losses continue to increase as the beam offset increases; however, it is evident that, accepting a loss up to 15% on a single diode, would allow increasing the number of stacked diodes beyond the number allowed by the fiber NA alone.

Finally, in light of these comparisons between experimental data and simulation results, it is safe to conclude that the model agrees very well with the experimental data and thus it can be employed in the design of HPLD multiemitters.

4.2 Spectral multiplexing via dichroic mirror: a statistical approach

Dichroic mirrors are composite elements made by a proper sequence of thin film layers deposited on a bulk substrate that act as an optical high pass or low pass filter around a certain wavelength λ_0, as shown schematically in Fig. 4.8. The spectral multiplexing technique is based on the use of dichroic mirrors to spatially overlap a number of collimated laser beams, each having a different wavelength, with an an accuracy limited only by the mechanical alignment and positioning accuracy of

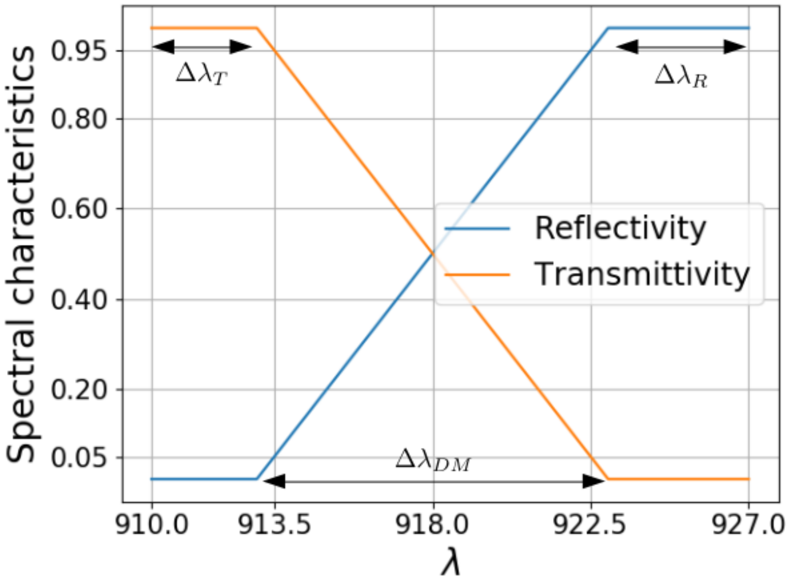

Figure 4.8: Ideal spectral characteristic of a dichroic mirror.

the optical elements involved. Letting the i-th combined beam to be characterized by an optical power P_i and a brightness B_i defined as:

$$B_\mathrm{i} = \frac{P_\mathrm{i}}{\pi^2\,\theta^2_\mathrm{FF,i}\,w_\mathrm{i,0}} \tag{4.11}$$

where $\theta_\mathrm{FF,i}$ is the far field divergence angle of the i-th beam and $w_\mathrm{0,i}$ is the i-th minimum beam spot size, the resulting beam is characterized by an optical power

$$P_\mathrm{sm} = \sum_\mathrm{i=0}^\mathrm{N} P_\mathrm{i} \tag{4.12}$$

and by a brightness

$$B_\mathrm{sm} = \sum_\mathrm{i=0}^\mathrm{N} B_\mathrm{i} \tag{4.13}$$

Clearly, if the combined beam are all equal, then both the resulting beam power and brightness scale linearly with the number of combined beam. Certainly, this scaling behavior represents the major advantage of spectral multiplexing with respect to both polarization multiplexing and beam stacking. Indeed, the beam stacking technique allows increasing linearly only the resulting beam optical power but actually decreases its brightness because its spot size, defined as the area that contains the 95% of its total power, increases as the number of combined beams increases as well. Just as the spectral multiplexing, the beam resulting from the polarization multiplexing is characterized by a linear increase of both optical power and brightness; however, the number of beam that can be combined is limited to the number of polarization states available, which is only two, while in case of spectral multiplexing the number of beams that can be combined is virtually unlimited. The major drawback of the spectral multiplexing is the linear decrease of the spectral density of power of the combined beam. As a matter of fact, each combined beam must be characterized by a different wavelength λ_{i}, hence the beam spectrum resulting from the spectral multiplexing will be the sum of many spectra each with a different peak wavelength. Depending on the application, the decrease of the spectral density of power may be acceptable or not. For instance, in case of direct laser diode application, such as in the case of welding, a wider spectrum is not really a concern, since what actually matters for that application is the spatial density of power and the total power carried by the laser. On the contrary, in case of fiber laser pumping applications, the absorption peak width of rare-earth doped fibers is usually of the order of 1 nm, hence the decrease of the spectral density of power severely limits the number of beams [118].

Ideally it would be sufficient to spectrally multiplex together beams whose wavelengths are only slightly different in order to minimize this major drawback, i.e., to exploit the capability of perfectly overlapping two different laser beams while still keeping a good spectral density of power. However, there are some fundamental limitation to this approach. With reference to Fig. 4.8, the wavelength interval $\Delta\lambda_{\mathrm{DM}}$ between the completely transmitted wavelength and the completely reflected wavelength cannot be arbitrarily small, setting a lower limit for the wavelength interval inside which the laser power is contained. Moreover, it should be also taken into account that a real laser source has non zero spectral variance; therefore, in order to reflect or transmit all of its power, the dichroic mirror spectrum should be characterized by a transmission flat band $\Delta\lambda_{\mathrm{R}}$ and a reflection flat band $\Delta\lambda_{\mathrm{T}}$, respectively wider that the transmitted and reflect beam spectra. Lastly, if the combined beam are originated by HPLDs, the dependence of their spectra from the temperature must be considered too. Indeed, it is well known that as the temperature rises, the peak wavelength of HPLDs shifts towards longer wavelengths; moreover, their spectral full width at half maximum increases too. Besides, also the dichroic mirror fabrication tolerances should be taken into account.

In such a complex scenario, it is only natural to resort to a statistical approach to evaluate the performance of a spectral multiplexing architecture in a realistic situation. To do so, applying the concept to a multiemitter module for simplicity, two sets of HPLDs are considered. In order to take into account the fact that the HPLDs are not completely equal one to the others, their peak wavelength is modeled as a random variable extracted from a gaussian distribution with a mean equal to $\lambda_0(T) + \delta\lambda_{\mathrm{s}}$ for the first set of laser diodes and $\lambda_0(T) - \delta\lambda_{\mathrm{s}}$ for the second set, and a standard deviation that can be derived from experimental measures. The quantity $\lambda_0(T)$ is instead function of the temperature

$$\lambda_0(T) = \lambda_0 + \rho_{\mathrm{T}} T \tag{4.14}$$

where ρ_{T} is a proportionality constant that can be determined experimentally and is related to the dependence on temperature of the HPLD spectral density of carriers [119]. Lately, λ_0 is equal to the wavelength such that the transmissivity of the dichroic mirror is equal to its reflectivity at room temperature. Each beam is assumed to be already well collimated and all the beams are assumed to deliver the same optical power. In a real application the latest assumption would not be true; however, as the variation in the optical power carried by each beam has nothing to do with the dichroic mirror and the multiplexing architecture itself, these are neglected in this model. The spectral density of power of each beam is assumed to be distributed according to the same distribution, which in this case is taken to be a Cauchy distribution:

$$\frac{\partial P}{\partial \lambda}(\lambda; \lambda_{\mathrm{pk}}, \gamma) = \frac{A}{\pi\gamma} \frac{\gamma^2}{(\lambda - \lambda_{\mathrm{pk}})^2 + \gamma^2} \tag{4.15}$$

where A is a constant such that the cumulative power is equal to 1 W and γ is the half width at half maximum of the spectral distribution. The reason for having chosen a Cauchy distribution is that the HPLD spectral density of power generally shows some long tails that cannot be modeled by mean of the more commonly used gaussian distribution. The dichroic mirror transmission spectrum $T_{\mathrm{DM}}(\lambda)$ is instead modeled by a piecewise linear function as follows

$$T_{\mathrm{DM}}(\lambda) = \left\{ \begin{array}{ll} 1 & \text{if} \quad \lambda - \lambda_0 \leq -\Delta\lambda_{\mathrm{DM}}/2 \\ \dfrac{\lambda - \lambda_0}{\Delta\lambda_{\mathrm{DM}}} + 0.5 & \text{if} \quad -\Delta\lambda_{\mathrm{DM}}/2 \leq \lambda - \lambda 0 \leq \Delta\lambda_{\mathrm{DM}}/2 \\ 0 & \text{if} \quad \lambda - \lambda_0 \geq \Delta\lambda_{\mathrm{DM}}/2 \end{array} \right\} \tag{4.16}$$

where it is assumed that the dichroic mirror spectrum is basically frozen and doesn't change substantially with temperature. In reality, also the spectrum of the dichroic mirror would shift as its temperature increases, as would happen if a high power beam passes through it for a long time; however the dichroic mirror spectrum shift due to the temperature is in general an order of magnitude smaller than the shift with respect to the temperature of the peak wavelengths, hence the validity of this assumption.

Letting the number of combined diodes to be $2N$, and supposing that the first N diodes have a peak wavelength equal $\lambda_0(T) + \delta\lambda_{\mathrm{s}}$ and that the remaining diodes have a peak wavelength equal to $\lambda_0(T) - \delta\lambda_{\mathrm{s}}$, the amount of power the i-th HPLD delivers, once it has passed through the dichroic mirror is equal to

$$
\begin{gathered}
P_{\mathrm{i}}^{\mathrm{del}}(\lambda_{\mathrm{pk}}^{\mathrm{i}}(T),\,\delta\lambda_{\mathrm{s}},\Delta\lambda_{\mathrm{DM}}) = \int \mathrm{d}\lambda\, \frac{\partial P}{\partial\lambda}(\lambda;\lambda_{\mathrm{pk}}^{\mathrm{i}}(T),\,\gamma)\, U_{\mathrm{DM}}^{\mathrm{i}}(\lambda;\lambda_0,\,\Delta\lambda_{\mathrm{DM}}) \\
U_{\mathrm{DM}}^{i}(\lambda_0,\,\Delta\lambda_{\mathrm{DM}}) = \left\{ \begin{array}{cl} T_{\mathrm{DM}}(\lambda;\lambda_0,\,\Delta\lambda_{\mathrm{DM}}) & \text{if}\ \ 1 \le i \le N \\ \\ 1 - T_{\mathrm{DM}}(\lambda;\lambda_0,\,\Delta\lambda_{\mathrm{DM}}) & \text{if}\ \ N+1 \le i \le 2N \end{array} \right\}
\end{gathered}
\tag{4.17}
$$

It is quite evident that, given a certain temperature, which can be regarded as the model independent variable, the delivered power from each diode is a function of two deterministic parameters ($\Delta\lambda_{\mathrm{DM}}$ and $\delta\lambda_{\mathrm{s}}$), which can be used as design parameters and be tuned to maximize the system performances, and a stochastic variable parametrized by $\lambda_{\mathrm{pk}}^{\mathrm{i}}(T)$, which takes into account the statistical features of the ensemble of the laser diodes. The total delivered power, for a single realization of the system, is given by:

$$
P_{\mathrm{DM}}^{\mathrm{tot}}(\{\lambda_{\mathrm{pk}}(T)\}_{\mathrm{r}},\,\delta\lambda_{\mathrm{s}},\Delta\lambda_{\mathrm{DM}}) = \sum_{\mathrm{i}=1}^{2N} P_{\mathrm{i}}^{del}(\lambda_{\mathrm{pk,r}}^{i}(T),\,\delta\lambda_{\mathrm{s}},\Delta\lambda_{\mathrm{DM}})) \tag{4.18}
$$

and the system efficiency can be expressed as

$$
\eta_{\mathrm{DM}}(\{\lambda_{\mathrm{pk}}(T)\}_{\mathrm{r}},\,\delta\lambda_{\mathrm{s}},\Delta\lambda_{\mathrm{DM}}) = \frac{P_{\mathrm{DM}}^{\mathrm{tot}}(\{\lambda_{\mathrm{pk}}(T)\}_{\mathrm{r}},\,\delta\lambda_{\mathrm{s}},\Delta\lambda_{\mathrm{DM}})}{2NP_0} \tag{4.19}
$$

where P_0 is the total power emitted by each emitter. Finally, the average efficiency of the spectral multiplexing system $\bar{\eta}_{\mathrm{DM}}(\delta\lambda_{\mathrm{s}},\Delta\lambda_{\mathrm{DM}})$ and its standard deviation $\sigma_{\mathrm{DM}}(\delta\lambda_{\mathrm{s}},\Delta\lambda_{\mathrm{DM}})$ can be simply computed, respectively, as an average and a standard deviation over multiple system realizations in order to integrate out the remaining dependence on the stochastic feature of the system

$$
\begin{gathered}
\bar{\eta}_{\mathrm{DM}}(\delta\lambda_{\mathrm{s}},\Delta\lambda_{\mathrm{DM}}) = \frac{1}{N_{\mathrm{r}}} \sum_{\mathrm{r}=0}^{\mathrm{N_r}-1} \eta_{\mathrm{DM}}(\{\lambda_{\mathrm{pk}}(T)\}_{\mathrm{r}},\,\delta\lambda_{\mathrm{s}},\Delta\lambda_{\mathrm{DM}}) \\
\sigma_{\mathrm{DM}}(\delta\lambda_{\mathrm{s}},\Delta\lambda_{\mathrm{DM}}) = \sqrt{\frac{1}{N-1} \sum_{\mathrm{r}=0}^{\mathrm{N_r}} (\eta_{\mathrm{DM}}(\{\lambda_{\mathrm{pk}}(T)\}_{\mathrm{r}},\,\delta\lambda_{\mathrm{s}},\Delta\lambda_{\mathrm{DM}}) - \bar{\eta}_{\mathrm{DM}}(\delta\lambda_{\mathrm{s}},\Delta\lambda_{\mathrm{DM}}))^2}
\end{gathered}
\tag{4.20}
$$

where N_{r} is the number or realization considered.

4.3 400 W multiemitter design exploiting WDM of DBR-HPLDs and polarization multiplexing

One of the main reason why the spectral multiplexing has not been yet widely adopted to further increase the output power of multiemitter modules is that it increases the multiemitter assembling complexity and time and reduces the emitters output power, as discussed in Ch. 3, ultimately increasing the cost per emitted watt (\$/W) ratio. A solution to this problem is the use of innovative HPLDs intrinsically wavelength stabilized. These chips integrate a wavelength stabilization grating and not only are capable of delivering about the same power of their FP counterpart, but outperform them in terms of thermal stability, spectral width and stabilization for different driving currents [120]. The module design is based on the use of intrinsically wavelength stabilized DBR-HPLD designed and produced by Convergent Photonics. These chips are not commercially available yet and emit about 10 W at a current of 10 A, hence more or less the same power as the standard FP-HPLD. However, thanks to the integrated DBR structure, compared

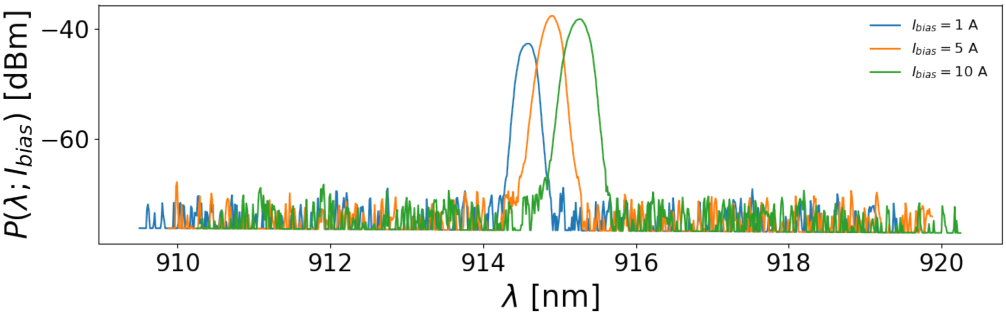

Figure 4.9: DBR-HPLDs spectra at different driving currents from which it is possible to note that 90% of the total power is contained in a wavelength interval of only 0.5 nm around their peak wavelength.

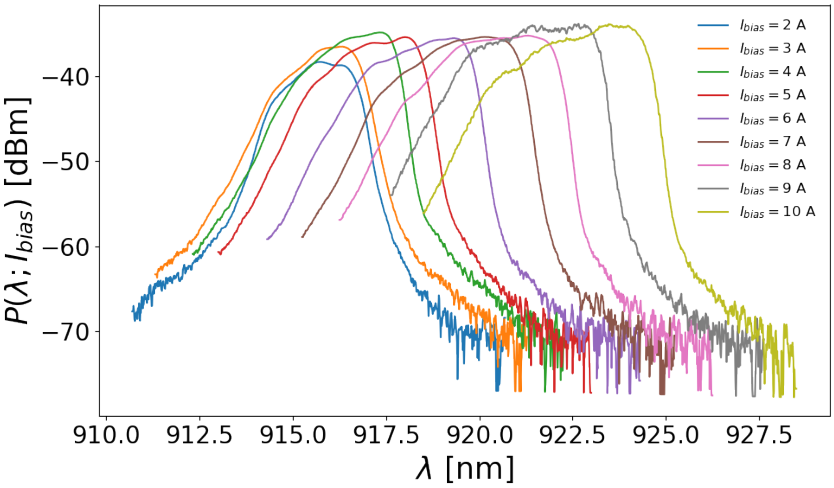

Figure 4.10: FP-HPLDs spectra at different driving currents.

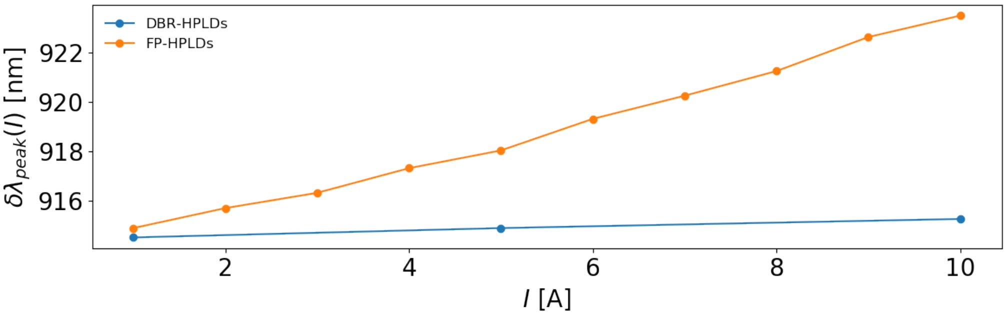

Figure 4.11: Peak wavelength shift as function of driving current. The peak wavelength has been computed as the maximum of the spectrum acquired by an OSA characterized by a minimum resolution of 0.06 nm

to standard FP-HPLD, whose 90% of power is contained in a wavelength interval ranging from 3 nm to 4.5 nm around their peak wavelength, as depicted in Fig. 4.10, they show a much narrower spectrum with about 90% of the total power in 0.5 nm, as clearly visible in Fig. 4.9, and an overall spectral shift with respect to injection current and temperature about one order of magnitude smaller, as evident from Fig. 4.11. Moreover, DBR-HPLD show an average spectral density of power of 20 W/nm, which is an order of magnitude higher than the FP-HPLDs average spectral density of power, which ranges from 3.3 W/nm to 2.3 W/nm as the driving current increases from 1 A to 10 A. These features make them ideal for WDM applications, which require very good wavelength stability and narrow spectra. In order to maximize the number of wavelengths that can be effectively multiplexed, and therefore choose the optimal wavelength spacing and the optimal design for the dichroic mirror, the stochastic model detailed in Sect. 4.2 has been exploited to simulate the module in realistic conditions. This model takes into account the DBR-HPLD peak wavelength and spectrum distribution to compute the total average and the standard deviation of the power transmitted through the dichroic mirror versus temperature in the 15 °C to 35 °C range and the design parameters, namely the dichroic mirror 5%-95% transition bandwidth $\Delta\lambda_{\mathrm{t}}$, which coincides with $\Delta\lambda_{\mathrm{DM}}$ of Sect. 4.2 model, and the laser diode wavelength spacing $\Delta\lambda_{\mathrm{l}}$, which corresponds to $2\delta\lambda_{\mathrm{s}}$ in Sect. 4.2 model. It is clear, from Fig. 4.12, that the best results are obtained having a $\Delta\lambda_{\mathrm{t}}$ as small as possible and $\Delta\lambda_{\mathrm{l}}$ at least 1 nm larger than $\Delta\lambda_{\mathrm{t}}$ to take into account possible peak wavelength shifts. Current state of the art dichroic mirror fabrication leads to at least 6 nm transmission wavelength, setting the laser diode wavelength spacing lower bound to 6.5 nm. The choice of the remaining optical elements has been carried out using the multiemitter model based on the WOF and extensively detailed in Sect. 4.1. The result is a DBR-HPLDS based multiemitter fitting up to seven 6.5 nm spaced wavelength into the 905 nm to 945 nm ytterbium pump band without the use of external stabilization devices. Combining it with a

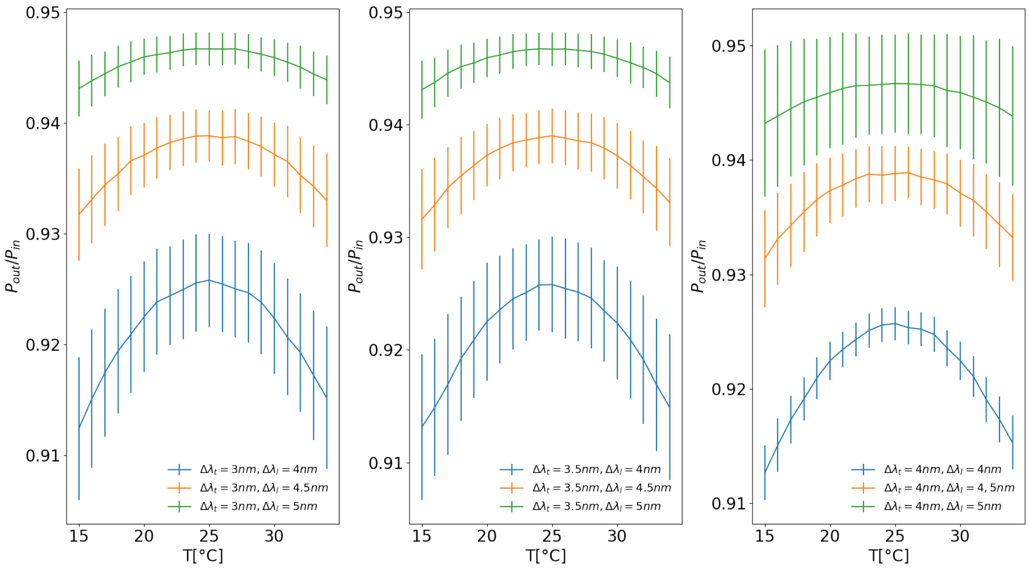

Figure 4.12: WDM efficiency versus temperature for different values of $\Delta\lambda_t$ and $\Delta\lambda_l$.

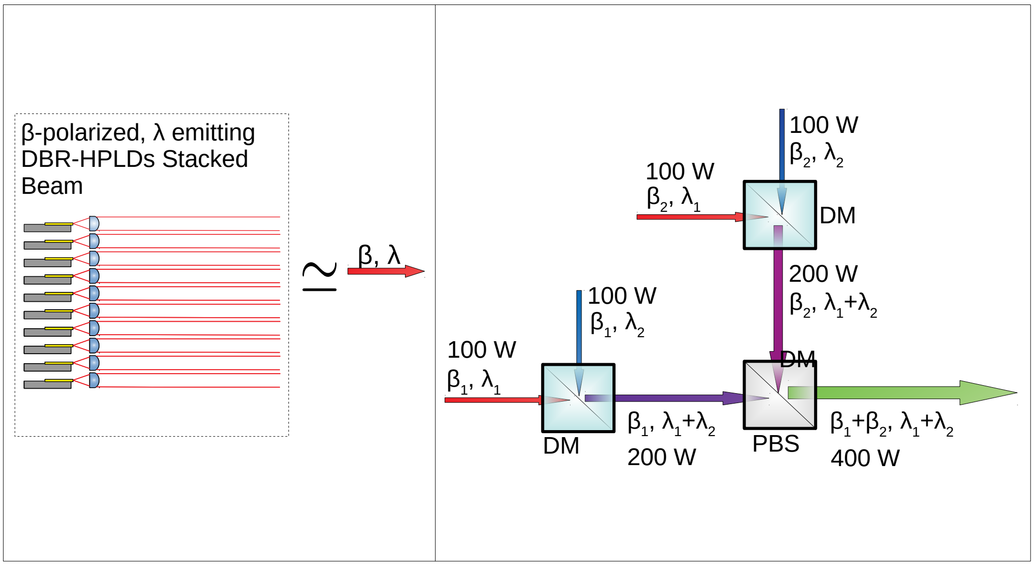

Figure 4.13: Schematic representation of a multiemitter that exploit beam stacking,WDM, and polarization multiplexing of DBR-HPLDs.

proprietary layout architecture, a family of high power modules that can be used both in pump sources for ytterbium-doped fiber lasers and in direct-diode material processing, whose output power ranges theoretically from 140 W to over 400 W in a 135/0.15 fiber at 10 A has been designed.

As shown in Fig. 4.13, the main building block for this family of modules is a stack of 10 large area DBR-HPLDs, sharing the same wavelength and polarization, such that the resulting stacked beam can be focused into a 135 µm optical fiber with a numerical aperture equal to 0.2 and delivering up to 100 W. Two of these beam can be combined by WDM into a single beam keeping the same numerical aperture and polarization but increasing the delivered optical power to 200 W and finally, exploiting the polarization multiplexing, two beam resulting from beam stacking and WDM can be multiplexed together into a single beam having, once again, the same beam quality as the original beam derived from beam stacking and delivering up to 400 W.

4.3.1 Experimental results

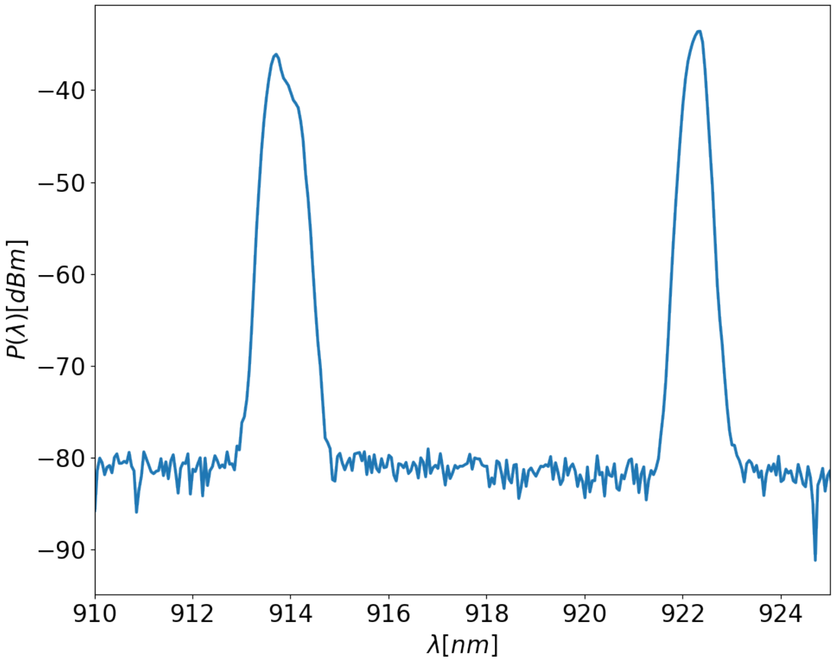

Figure 4.14: Measured spectrum of the HPLDs module exploiting WDM.

A 180 W demonstrator module has been assembled by spatial multiplexing of two sets of 9 DBR-HPLD, and then by spectrally combining the two resulted beams, whose design wavelength are 913 nm and 923 nm. To do so a custom dichroic filter with a 9 nm 5%-95% transition bandwidth, whose characterization is shown in Fig. 4.15, has been exploited. In Fig. 4.14 the spectrum of this prototype, which is composed of two narrow peaks at about 913 nm and 923 nm is shown. The measured power is about 120 W at 10 A and 150 W at 12.5 A, as it can be seen in Fig. 4.16. The difference between the predicted output power and the measured one

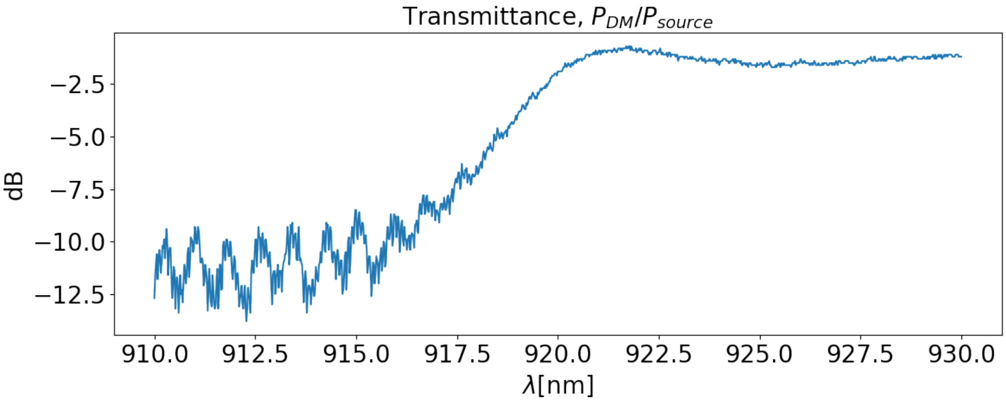

Figure 4.15: Measured transmission spectrum of the custom dichroic mirror.

is mostly due to DBR-HPLDs used in this module. Indeed, compared to the latest DBR-HPLDs available, which have an average output power of 9 W at 10 A, the DBR-HPLDs used in this experiment deliver about 8 W at 10 A, limiting the module maximum average output power to about 140 W at 10 A. Then, the remaining “missing” power is due to the dichroic mirror power dissipation, as predicted by the aforementioned stochastic model, and the optical coupling between the laser diodes and the rest of the optical elements involved. However, despite these imperfections, the reported module performance is in line with that of a standard modules composed by 2 polarization multiplexed 10-beam-stacked FP-HPLDs emitting about 9 W at 10 A since it delivers on average 150 W out of a theoretical maximum of 180 W, with a 83% efficiency. In addition, the proposed module can further exploit polarization multiplexing, therefore doubling the overall power. Its brilliance and spectral features makes it suitable for fiber laser pumping in the 905 nm to 945 nm ytterbium pump band, thanks to the extremely narrow and stable spectrum about the design wavelength, and direct laser diode application, especially in the material processing field. Moreover, a two wavelength multiplexing has been shown to be as or more efficient for (almost) doubling the power than the more common polarization multiplexing approach. Therefore, taking also into account that there is no theoretical upper bound to the number of wavelengths that can be spectrally multiplexed, the WDM emerges as a very promising approach to further scale up the power of HPLDs modules, especially for direct laser diodes applications. Given the excellent results obtained by this demonstrator, it is possible to conclude that the feasibility of a high power, high brilliance DBR-HPLD module exploiting beam stacking, WDM and polarization multiplexing has been demonstrated. Further work will be devolved to increase the module raw output power up to at least 200 W and increase its efficiency by further optimizations.

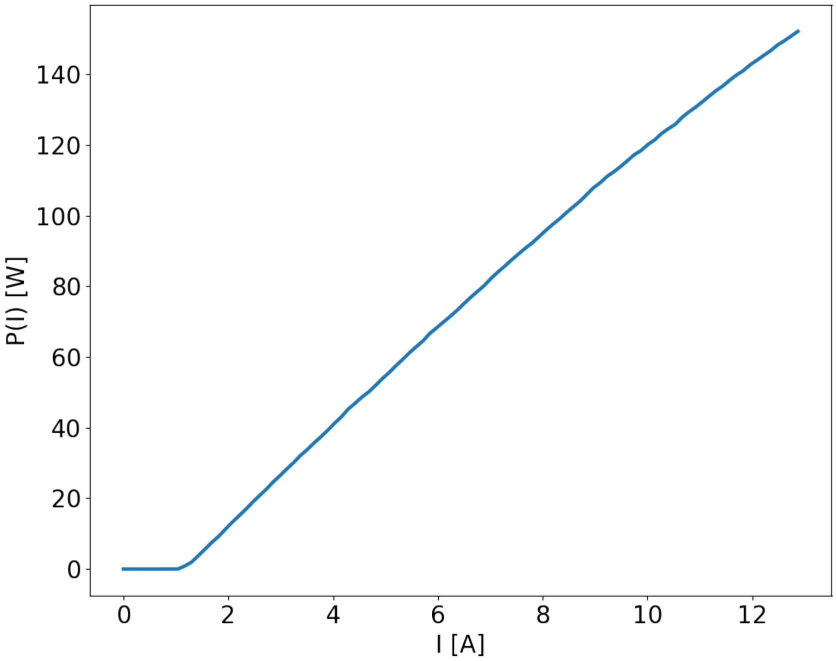

Figure 4.16: Measured PI of the HPLDs module exploiting a two wavelength multiplexing instead of polarization multiplexing. The power has been measured by a powermeter characterized by a resolution of 1 mW

4.4 400 W multiemitter design exploiting WDM of externally stabilized HPLDs and polarization multiplexing

As already demonstrated in Sect. 4.2, the emitter stability with respect to temperature changes is a parameter that largely determines the efficiency of the combining architecture based on spectral multiplexing. For this reason, the use of DBR-HPLDs as building block in a WDM architecture, discussed in Sect. 4.3, is most suited but presents a drawback in terms of assembling time and overall costs. Indeed, the fabrication of such emitters, compared to the fabrication process of FP-HPLDs, requires an additional electron beam lithography fabrication step that increases the fabrication time and thus the costs.

An alternative approach is to use externally stabilized HPLDs by mean of a VBG. As discussed in Sect. 3.2, in order to stabilize a single emitter a VBG must be carefully positioned along the emitter beam optical path to create an external cavity. If the feedback coming from the external cavity is stronger than the one provided by the intrinsic cavity, then the emitter wavelength is forced to the external cavity resonance wavelength at the cost of increasing the emitter threshold current and decreasing the emitter gain.

It is clear that this approach would be highly unfeasible if each emitter of a HPLD module were to be individually spectrally stabilized. Indeed, a VBG would be added to each emitter optical path, enormously increasing the overall multiemitter assembling time, thus cost, well beyond the cost of a DBR-HPLD module. The comparison between a DBR-HPLD module and a multiemitter made of externally stabilized diodes would be way less unbalanced toward the DBR-HPLDs module if the plurality of FP-HPLDs could be spectrally stabilized together by the same VBG.

Exploiting the multiemitter model based on the WOF, a family of multiemitter modules theoretically able to deliver up to 400 W exploiting externally stabilized broad area FP-HPLDs has been designed. The building block for this family of HPLD modules, as in Sect. 4.3, is a stack of spatially multiplexed FP-HPLDs, whose resulting beam, from now on referred to as stacked beam, can deliver up to 100 W and can be focused into an optical fiber with a 200 µm core and a 0.22 maximum numerical aperture. With reference to Fig. 4.17, a VBG is inserted after the stacked beam collimation system in order to obtain a spectrally stabilized stacked beam. Two of these stacked beams, having different wavelengths and same polarization, can then be multiplexed using a dichroic mirror, obtaining a beam able to deliver up to 200 W in the same optical fiber. Finally, exploiting a polarization multiplexing level, two of the aforementioned beams, having now different polarization, can then be combined together in order to obtain a beam delivering up to 400 W, with

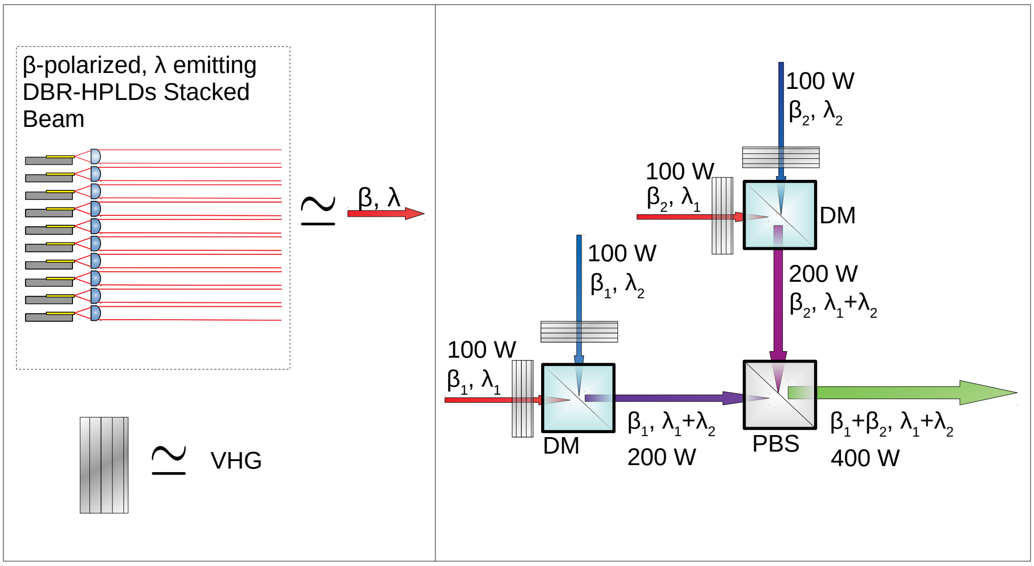

Figure 4.17: Schematic representation of a multiemitter exploiting spatial, WDM and polarization multiplexing of externally stabilized FP-HPLDs.

unchanged beam quality with respect to that of the stacked beams.

Once again, the choice of the dichroic mirrors and of the VBG is made exploiting the WDM model detailed in Sect. 4.2, allowing for the maximization of the performance with respect to the temperature while achieving a spectral density of power as large as possible in realistic conditions.

4.4.1 Experimental setup

The first step in the realization of this module consists in the simultaneous spectral stabilization of an entire stack of FP-HPLDs. It is evident that for this purpose, not only the chips in the stack must be well collimated, but also the different beams composing the stack must be as parallel as possible. Indeed, if this condition is not verified, then the beams incidence angle on the VBG may differ significantly from one beam to the others, resulting in the spectral stabilization of only a small subset of the stacked beam. This problem has been overcome exploiting the automatic assembly lines that Convergent Photonics uses for its 9xx multiemitter. Thanks to these machines, a set of 10 FP-HPLDs emitting at 973 nm have been assembled in a standard Convergent Photonics $\beta L - 100$ package resulting in a stack of 10 beams exhibiting an individual residual divergence lower than 0.005 rad and a deviation from perfect parallelism lower than 5%, able to deliver up to 85 W in a 135 µm, 0.22 NA optical fibers, as shown in Fig. 4.18.

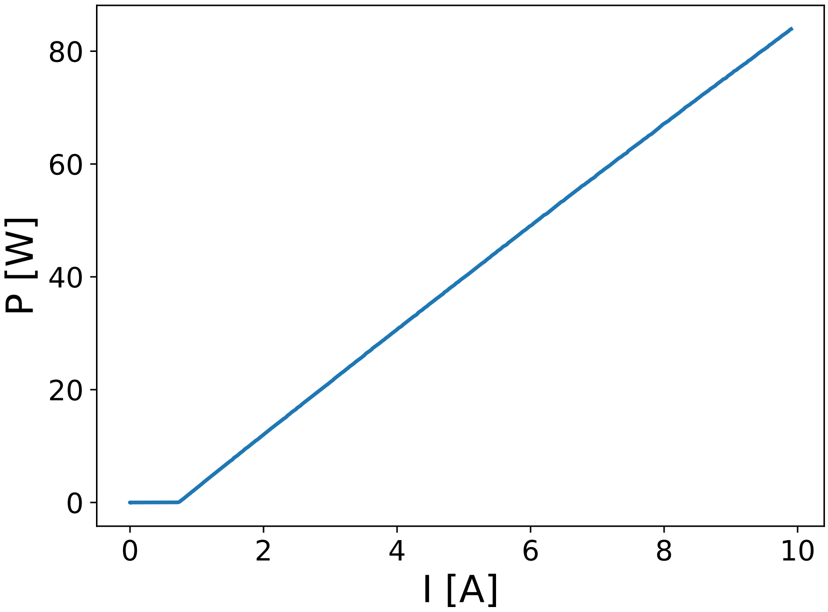

Figure 4.18: PI curve of the unstabilized stacked beam. The PI curve has been acquired by a Thorlabs powermeter characterized by a power resolution of 1 mW.

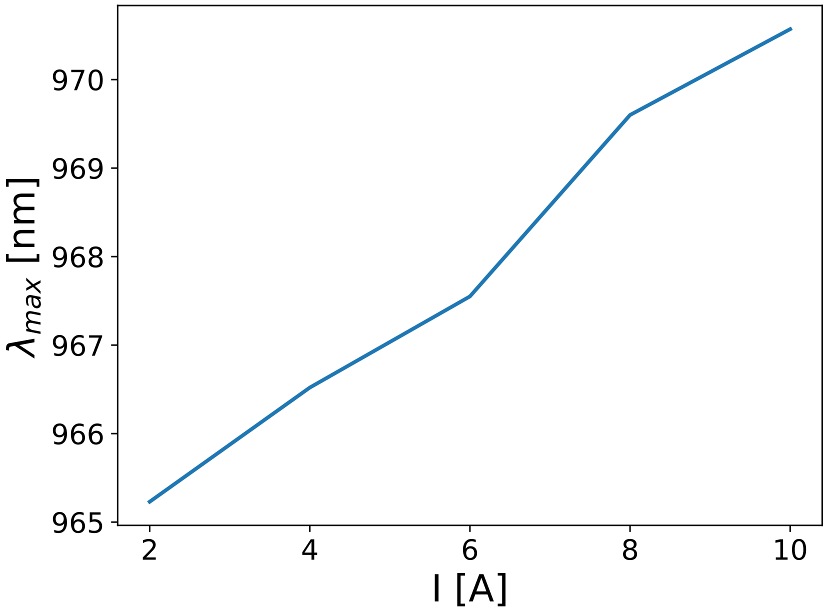

Figure 4.19: Peak wavelength change as function of the driving current. The peak wavelength has been acquired by an OSA characterized by a minimum resolution of 0.06 nm

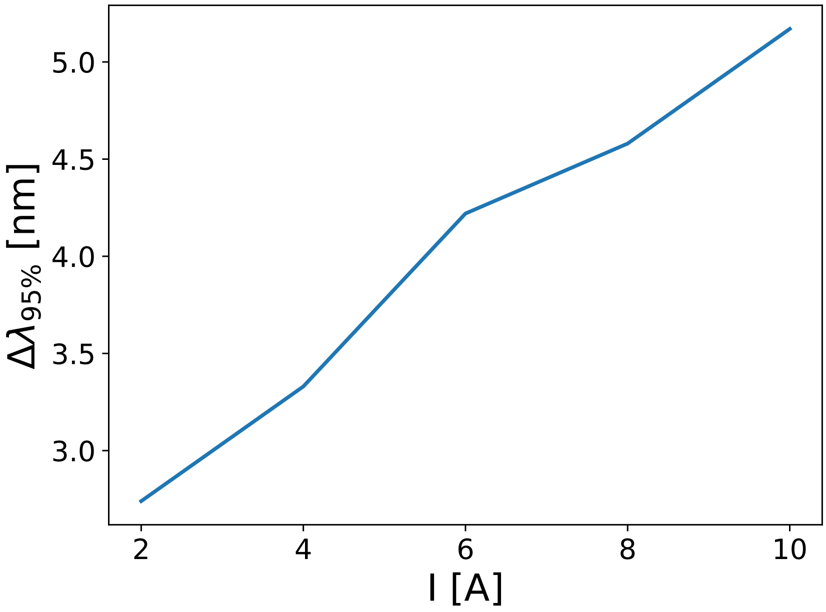

Figure 4.20: Spectral width at 95% of power as function of the driving current.

As expected for FP-HPLDs, the spectral width increases from 2.7 nm to 5.1 nm and the peak wavelength shifts from 964 nm to 970 nm as the driving current increases from 1 A to 10 A, corresponding to a peak wavelength shift due to temperature changes of about 0.3 nm K^{-1}, as shown in Fig. 4.19 and in Fig. 4.20. The spectral stabilization has been achieved using VBGs from Ondax that reflect at 976 nm with a peak reflectivity value ranging from 20% to 30%. The spectral stabilization requires to place and align the VBG in the stacked beam optical path with an angular accuracy of the order of 10^{-4} radiands and a spatial accuracy of the order of 0.1 µm, therefore a gripper mounted on a 6-axis piezoelectric movement system with a linear movement precision of the order of 0.1 µm and an angular precision of 10^{-4} radiant has been exploited, shown in Fig. 4.21. The VBG positioning and alignment has been executed in active loop, namely raster scanning all possible combination of angular and spatial VBG position with respect to the stacked beam until most of its power was enclosed in a wavelength interval centered around the VBG resonant wavelength λ_{VBG}. The evaluation of what is basically a density of power has been performed using an integrating sphere to collect a small fraction of the stacked beam into the Avantes AvaSpec-ULS2048CL-EVO spectrometer and computing the relative amount of power in the wavelength interval

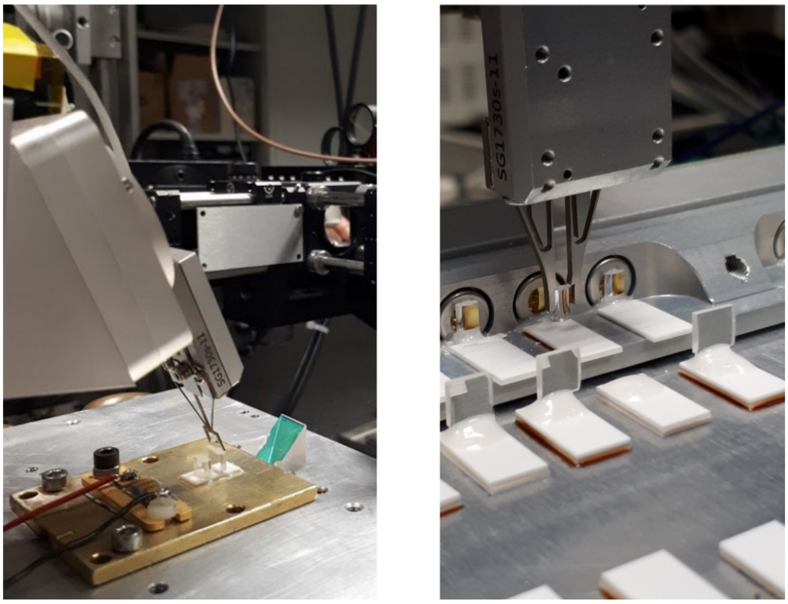

Figure 4.21: On the left, the gripper mounted on the 6-axis movement system while aligning a collimating lens with sub-micrometric precision. On the right, a zoom-in on the gripper itself.

$[\lambda_{\mathrm{VHG}} - \Delta\lambda, \lambda_{\mathrm{VHG}} + \Delta\lambda]$ as:

$$p_{\mathrm{VHG}} = \frac{\int_{\lambda_{\mathrm{VHG}}-\Delta\lambda}^{\lambda_{\mathrm{VHG}}+\Delta\lambda} P(\lambda)\,\mathrm{d}\lambda}{\int P(\lambda)\,\mathrm{d}\lambda} \tag{4.21}$$

with $\Delta\lambda = 1.5\,\mathrm{nm}$. Clearly, as the VBG positioning becomes closer and closer to the ideal one, the amount of power in the wavelength interval around λ_{VBG} increases as well.

Once multiple stacked beams are spectrally stabilized, assuming each one has a large purity of polarization, namely the amount of power associated to a polarization compared to the total power, then they can be combined together using dichroic mirrors and polarization beam splitters, as shown in Fig. 4.17.

4.4.2 Experimental results

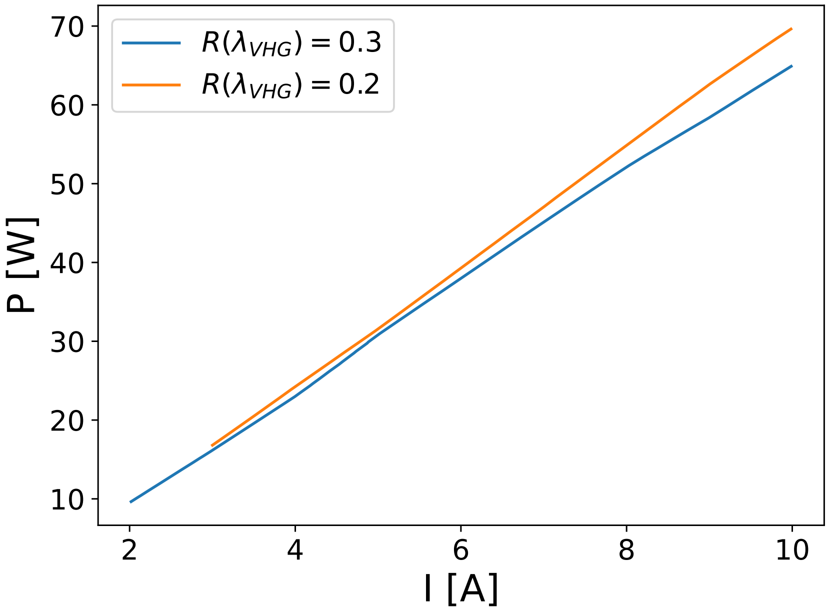

Figure 4.22: PI characteristics of a stacked beam spectrally stabilized by VBGs with 20% and 30% reflectivity peak. The measurement has been performed using a powermeter from Thorlabs characterized by an accuracy of 1 mW

Fig. 4.22 shows the measured PI of the same stacked beam, which are spectrally stabilized using two different VBGs, both characterized by a Bragg wavelength equal to 976 nm ± 0.5 nm, a reflection peak whose FWHM of 0.2 nm and whose intensity is equal to, respectively, 20% and a 30% and a spectral Bragg wavelength

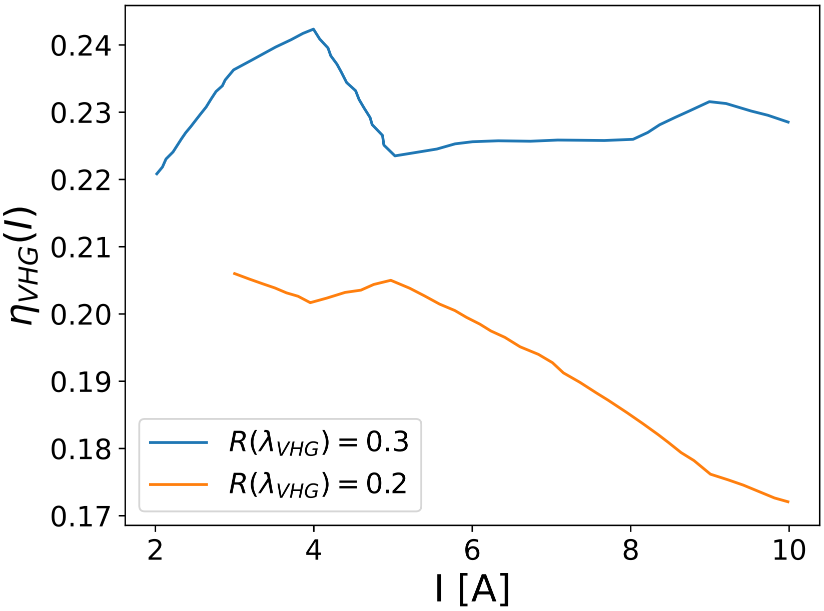

Figure 4.23: Losses induced by spectral stabilization using VBGs with 20% and 30% reflectivity peak.

spectral shift due to a change of temperature equal to 0.01 nm K^{-1}, which is one order of magnitude smaller compared to the FP-HPLDs peak wavelength shift due to temperature changes. As it can be seen from Fig. 4.23, inserting the VBG in the stacked beam optical path introduces some losses, which are obviously smaller in the case of the one characterized by 20% reflectivity, whose induced losses decrease to about 18% at about 10 A. Anyway, it has been possible to verify, by mean of a thermal camera, that the VBG itself heats up to a temperature of about 60 °C, hence a significant part of the losses is due to some power dissipation by the VBG, which justify its temperature increases. Nevertheless, the spectrally stabilized stacked beam shows, not unexpectedly, superior performance in terms of temperature stability and spectral width. As shown in Fig. 4.24 and in Fig. 4.25, the stabilized stacked beam shows a peak wavelength equal to 977 nm±0.4 nm in the current range [2 A, 10 A] with a 90% spectral width equal to about 3 nm. While it is true that the VBG reflectivity peak has a FWHM of 0.2 nm, which would approximately correspond to a 90% spectral width of about 1 nm, the fact that the stacked beam shows a 90% spectral width more or less three times larger can be explained considering the small differences in the incidence angle of the spatially multiplexed beams on the VBG. Indeed, as the incidence angle changes due to experimental non-ideality, also the resonance wavelength of the external cavity changes so, even if ideally all beams should share the same peak wavelength, in reality each will “feel” a slightly different cavity characterized by a slightly different resonance wavelength. Despite

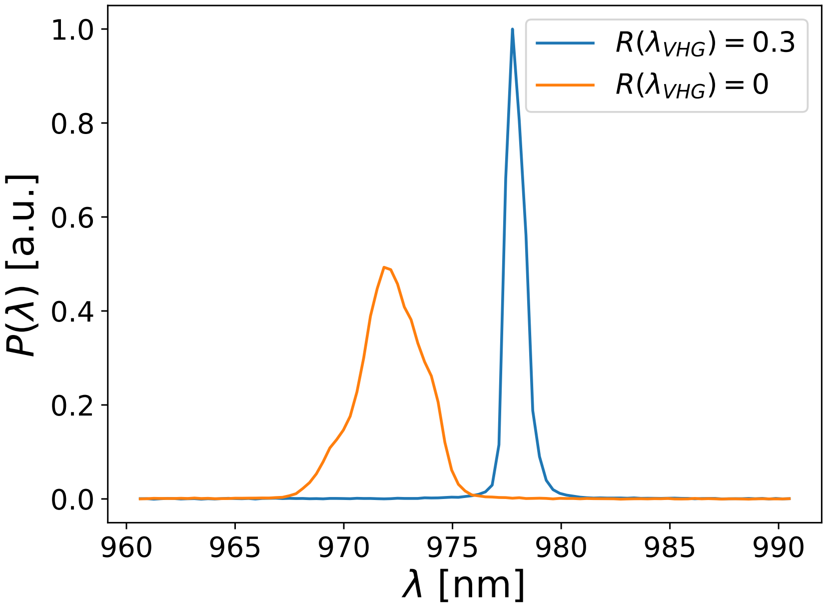

Figure 4.24: A comparison between the spectra of the FP-HPLD stacked beam in absence of VBG and in case of spectral stabilization by mean of a VBG characterized by a 30% reflectivity peak. Both spectra are taken at a driving current of 10 A.

this non-ideality of the setup, the stabilized stacked beam shows a spectrum that is extremely stable with respect to temperature changes of the multiplexed laser diodes, which is typically induced by an increase of the driving current. Finally, few further considerations are in order about the design of a multiemitter module able to deliver up to 400 W. Indeed, even assuming a lossless spectral stabilization, from the data shown so far a stacked beam composed of 10 emitters, spectrally stabilized or not, would not be able to deliver more than 60 W, therefore it would not be possible to reach 400 W combining together four of these “building blocks”. However, in the latest years, new generations of HPLDs able to deliver in a spectrally unstabilized fashion and in operative condition up to 20 W at 20 A has been developed and a multiemitter exploiting these HPLDs has shown 350 W with a driving current equal to 20 A [121]. It is clear that, even considering a spectral stabilization loss equal to 20% at the maximum driving current, a spectrally stabilized stacked beam able to deliver at least 100 W could be obtained by beam stacking 10 of this new generation emitters with a driving current equal to 12.5 A. Said so, even considering some losses induced by spectral multiplexing and polarization multiplexing, a module actually able to deliver 400 W in long time operations with a driving current less or equal to 15 A could be assembled by spectral multiplexing of two couples of 100 W stacked beam and then by polarization multiplexing of the

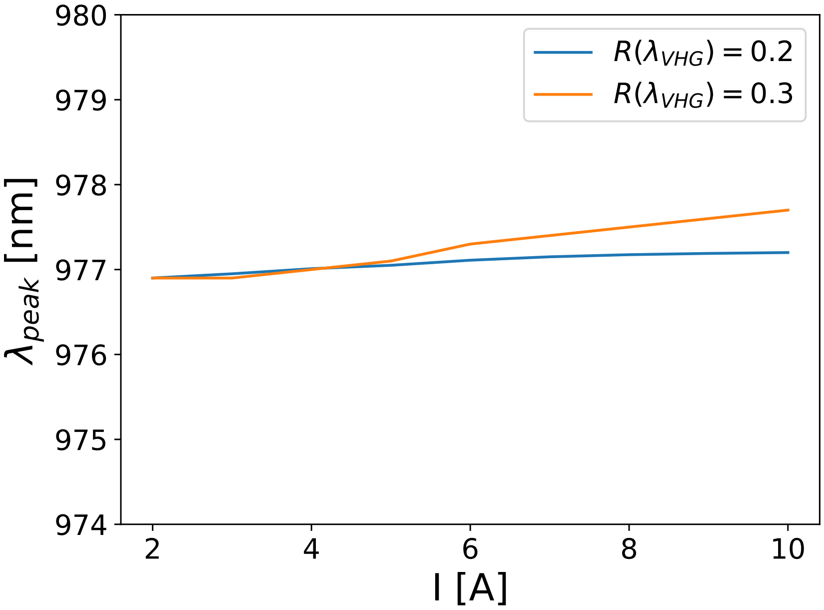

Figure 4.25: A comparison between the spectrally stabilized stacked beam peak wavelength in case of a 20% and 30% reflectivity VBG. The peak wavelenght has been acquired by an OSA characterized by a minimum resolution of 0.06 nm

resulting beams.

Chapter 5

Conclusions

This monograph is intended as the summary of the author's research done in the last three years about the power scaling of high power laser systems, with particular application to the industrial field. Despite being already a hot topic at the beginning of his research, the importance and the attention given to this field has grown considerably over the last three years, from 2019 to 2021. Indeed, beyond the pure academic interest, the lack of raw materials and the climate change are imposing a change of paradigm in manufacturing, demanding for the use of new, innovative and sustainable technologies in order to reduce our impact on the environment. It is not difficult to foresee that laser-based technologies will be more and more relevant thanks to their flexibility, efficiency, and yield, all characteristics that ultimately lead to cost reductions also in the complex scenario of circular economy. Truth is, the laser-based technologies are already bringing innovation in a very large range of applications. For instance, they are profoundly modifying the approach to the materials processing, to assembling of batteries, which will be fundamental in the next future, and to the manufacturing of electronic components. Nevertheless, this trend implies an increasing request – already expressed by the market – for more powerful, more brilliant and high quality laser systems. This request can be satisfied in few ways, which have been analyzed throughout this work.

The scale up of laser systems cannot simply be based on the scale up of the individual laser sources. Instead, it has to rely on the combination of a plurality of laser sources to obtain a more powerful, brighter and higher quality laser beam.

A promising way of doing so is the coherent multiplexing technique, detailed in Ch. 2. In order to theoretically analyze the critical issues of the coherent multiplexing, an innovative simulation method called wave optic framework has been implemented and experimentally validated. It has been shown that the coherent multiplexing allows combining tens to hundreds of powerful fiber lasers while keeping the quality of a single beam. However, its main drawback, which lies in the complexity of the setup, being expensive and extremely sensible to perturbation, will likely avoid the wide deployment of this technique in the near future unless it is the only solution for the problem at hand.

An alternative excellent option to combine a plurality of laser beams is the spectral multiplexing approach, detailed in Ch. 4, which is particularly effective when applied to high power laser diodes. To study the performance of this approach and to design an actual prototype, a stochastic model has been developed. The main advantage of the spectral multiplexing is that it allows maintaining a good beam quality – though not as good as in the case of the coherent multiplexing – while combining together a potentially arbitrary number of laser diodes. Moreover, the spectral multiplexing can be complementary to other multiplexing techniques, making it ideal in the scale up of laser systems where the spectral purity of the resulting beam is not a crucial parameter. To check its potential, a family of HPLD module based on spectral, spatial and polarization multiplexing has been designed and experimentally tested.

Efficient spectral multiplexing, however, requires the use of lasers with stable emission wavelength and pretty narrow spectral width. This would severely limit the applicability of such a technique in the case of high-power diode lasers because, using largely multi-mode Fabry-Perot semiconductor chips, they are characterized by broad emission spectra; moreover, their peak wavelength exhibits large shifts with the operating current and with the temperature. Therefore, prior to their use in spectral multiplexing techniques, these emitters require a spectral stabilization and this can be done by forming an external cavity with an additional reflector that complements the already existing intrinsic cavity. Traditionally, VBGs are used as external reflectors but their use implies a substantial decrease of the emitter power, which can be as large as 20%, as shown by the experimental data reported in this work. A new approach based on the use of custom, femtosecond inscribed FBGs in multimode fibers, detailed in Ch. 3, has been proposed to overcome these limitations. The experimental validations showed a power decrease even smaller than 10%. Given the promising potentiality shown by experiment on single emitters, future work will be devoted to the use of this approach to experimentally stabilize a whole HPLD module.

Ultimately, few additional considerations are worth to be made. It is sure that, to obtain extremely large power, brightness and quality laser beams, the coherent multiplexing represents the only viable approach. Anyway, it is also true that its implementation is way more expensive and complex than that of any other kind of multiplexing technique; hence, at the current state of this technology, the coherent multiplexing approach should be used only if any other approach is not suitable. Nevertheless, in this thesis it has been shown how the tools coming from the field of artificial intelligence and, in particular, neural networks can be used not only to increase the performances of coherent beam combining but also its robustness and possibility to be deployed outside of a laboratory environment. Rather than replacing the traditional feedback mechanism with a neural network, which is the main strategy adopted in the few examples that can be found in literature about the applications of a deep learning mechanism to the coherent beam combining, in the proposed method it is adopted a divide and conquer strategy: the phase perturbation sources are firstly grouped according to their characteristic frequency and then each of them is compensated in parallel by a different feedback loop. In this case, the neural network, which is intrinsically slower than the traditional SPGD updating algorithm due to its computational complexity, can be efficiently used to compensate the slower phase perturbation easing the burden on the SPGD algorithm. However, this should only be considered as an example of what can be achieved by the integration of tools coming from different research area. Further work should be devoted to the development of novel algorithm that can increase the efficiency and the convergence speed of the SPGD algorithm integrating in the algorithm itself an adaptive scheduling of the step sizes inspired by, for instance, the ADAM algorithm developed to speed up the error backpropagation in the neural networks. Such a step could actually be the key for bring the coherent beam combining outside of laboratories walls.

Anyway, it will take some time for this progresses to be made, therefore, if the spectral purity is not an issue, as in the case of materials processing, and a spectral width as large as few tens of nanometers is acceptable, then the spectral multiplexing should be preferred. Indeed, the spectral stabilization method allows keeping an overall good beam quality, while combining an almost arbitrary number of diodes into a single laser engine whose output power, brightness and beam quality could not be reached with the traditional spatial combining methods. This work has clearly shown the viability of this methods through experiment and the realization of prototypes.The main issue about the spectral multiplexing of high power laser diodes is the spectral stability of the emitters themselves. On one hand, DBR-HPLDs are more expensive and require a more complex fabrication process, on the other the stabilization process via VBG requires additional components and increases the assembly time. In both cases, the result is an increase of the overall cost per watt. The key changing technology is the stabilization of stacked beams exploiting FBGs. In this thesis, it has been experimentally demonstrated that this is a viable alternative to DBR-HPLDs and stabilization via VBG. and further work is going to be devoted to achieve a larger spectral stability temperature interval and and lower optical losses. These two parameters, in particular, can be solved by tuning the FBG fabrication procedure in very large mode area fibers. Considering the FBG low fabrication cost, large scalability, possibility of quick and flexible prototyping thanks to femtosecond laser based micro-machining workstation using and the capability of effortlessly connecting the FBG to the diodes delivery fiber by a simple splice, there is no doubt it will become the dominant method to achieve spectrally stabilized high power laser diodes and the key to the wide adoption of the spectral stabilization technique.

Bibliography

[1] *I limiti dello sviluppo. Rapporto del System dynamics group, Massachusetts institute of technology (MIT) per il progetto del Club di Roma sui dilemmi dell'umanità*. Edizioni scientifiche e tecniche Mondadori, 1972.

[2] *Climate Change 2021: The Physical Science Basis. Contribution of Working Group I to the Sixth Assessment Report of the Intergovernmental Panel on Climate Change*. IPCC, 2021.

[3] URL: https://www.photonics21.org/ppp-services/photonics-downloads.php.

[4] URL: https://www.laserfocusworld.com/test-measurement/article/14169059/photonicsbased-technologies-to-reduce-co2-by-3-billion-tons-per-year.

[5] Maija Leino, Joonas Pekkarinen, and Risto Soukka. "The Role of Laser Additive Manufacturing Methods of Metals in Repair, Refurbishment and Remanufacturing – Enabling Circular Economy". In: *Physics Procedia* 83 (2016). Laser Assisted Net Shape Engineering 9 International Conference on Photonic Technologies Proceedings of the LANE 2016 September 19-22, 2016 Fürth, Germany, pp. 752–760. ISSN: 1875-3892. DOI: https://doi.org/10.1016/j.phpro.2016.08.077. URL: https://www.sciencedirect.com/science/article/pii/S1875389216301845.

[6] *Semiconductor Laser Market - Growth, Trends, COVID-19 Impact, and Forecasts (2021 - 2026)*. Mordor Intelligence, 2021.

[7] *Lasers: Global Markets to 2024*. BCC Publishing, 2019.

[8] *Global Markets for Laser Systems, Components and Materials*. BCC Publishing, 2020.

[9] URL: https://world-of-photonics.com/en/newsroom/photonics-industry-portal/markets-trends/strong-growth-laser-market/.

[10] *The Worldwide Market for Lasers: Market Review and Forecast 2020*. Strategies Unlimited, 2019.

[11] Almantas Galvanauskas. "High power fiber lasers". In: *Optics and Photonics News* 15.7 (2004), pp. 42–47. DOI: 10.1364/OPN.15.7.000042.

[12] C. Jauregui, J. Limpert, and A. Tünnermann. "Prospects in power scaling of fiber lasers and amplifiers". In: *CLEO Pacific Rim Conference 2018*. Optical Society of America, 2018, Tu2L.1. DOI: `10.1364/CLEOPR.2018.Tu2L.1`.

[13] M.N. Zervas and C.A. Codemard. "High-power fiber lasers: A review". In: *IEEE Journal on Selected Topics in Quantum Electronics* 20.5 (2014), pp. 219–241. DOI: `10.1109/JSTQE.2014.2321279`.

[14] Yves Jaouën et al. "Power limitation induced by nonlinear effects in pulsed high-power fiber amplifiers". In: *Comptes Rendus Physique* 7.2 (2006). High power fiber lasers and amplifiers, pp. 163 –169. ISSN: 1631-0705. DOI: `https://doi.org/10.1016/j.crhy.2006.01.014`. URL: `http://www.sciencedirect.com/science/article/pii/S1631070506000387`.

[15] Manoj Kanskar et al. "High-temperature diode laser pumps for directed energy fiber lasers (Conference Presentation)". In: *Proc. SPIE*. Vol. 10192. 2017, 101920F. DOI: `10.1117/12.2263699`.

[16] R. Paoletti et al. "Wavelength-stabilized DBR high-power diode laser". In: *Journal of Physics: Photonics* 2.1 (2020), p. 014010. DOI: `10.1088/2515-7647/ab6712`.

[17] Jeff Hecht. "High-power fiber lasers". In: *Optics and Photonics News* 29.10 (2018), pp. 30–37. DOI: `10.1364/OPN.29.10.000030`.

[18] M. Hemenway et al. "Advances in high brightness fiber-coupled laser modules for pumping multi-kW CW fiber lasers". In: *Proc. SPIE*. Vol. 10086. 2017, p. 1008605. DOI: `10.1117/12.2250656`.

[19] Alessandro Mirigaldi et al. "Power scaling of laser diode modules using high-power DBR chips". In: *Proc. SPIE*. Vol. 11262. 2020, 112620W. DOI: `10.1117/12.2544947`.

[20] Yves Jaouën et al. "Power limitation induced by nonlinear effects in pulsed high-power fiber amplifiers". In: *Comptes Rendus Physique* 7.2 (2006), pp. 163 –169. DOI: `10.1016/j.crhy.2006.01.014`.

[21] D. J. Richardson, J. Nilsson, and W. A. Clarkson. "High power fiber lasers: current status and future perspectives". In: *Journal of the Optical Society of America B* 27.11 (2010), B63 –B92. DOI: `10.1364/JOSAB.27.000B63`.

[22] Wei-Wei Ke et al. "Thermally induced mode distortion and its limit to power scaling of fiber lasers". In: *Optics Express* 21.12 (2013), pp. 14272 –14281. DOI: `10.1364/OE.21.014272`.

[23] H. Yu. "Design and Development of Multi-Emitter High Power Laser Diode Modules". PhD thesis. Politecnico di Torino, 2017.

[24] X. Cheng, J. Wang, and C. Liu. “Beam combining of high energy fibre lasers”. In: *Hongwai yu Jiguang Gongcheng/Infrared and Laser Engineering* 47 (Jan. 2018). DOI: 10.3788/IRLA201847.0103011.

[25] X. Cheng, J. Wang, and C. Liu. “Beam combining of high energy fibre lasers”. In: *Hongwai yu Jiguang Gongcheng/Infrared and Laser Engineering* 47 (Jan. 2018). DOI: 10.3788/IRLA201847.0103011.

[26] Pratik Shukla, Jonathan Lawrence, and Yu Zhang. “Understanding laser beam brightness: A review and new prospective in material processing”. eng. In: *Optics and laser technology* 75 (2015), pp. 40–51. ISSN: 0030-3992.

[27] Zhimeng Huang et al. “Coherent beam combination of ten fiber arrays via stochastic parallel gradient descent algorithm”. In: *Journal of Optical Technology* 82 (Jan. 2015). DOI: 10.1364/JOT.82.000016.

[28] Hongxiang Chang et al. “First experimental demonstration of coherent beam combining of more than 100 beams”. In: *Photon. Res.* 8.12 (Dec. 2020), pp. 1943–1948. DOI: 10.1364/PRJ.409788. URL: http://www.osapublishing.org/prj/abstract.cfm?URI=prj-8-12-1943.

[29] W. Minster Kunkel and James R Leger. “Passive Coherent Laser Beam Combining With Spatial Mode Selecting Feedback”. eng. In: *IEEE journal of quantum electronics* 55.4 (2019), pp. 1–8. ISSN: 0018-9197.

[30] O Andrusyak et al. “Spectral Combining and Coherent Coupling of Lasers by Volume Bragg Gratings”. eng. In: *IEEE journal of selected topics in quantum electronics* 15.2 (2009), pp. 344–353. ISSN: 1077-260X.

[31] Chao Zhang et al. “Simultaneous passive coherent beam combining and mode locking of fiber laser arrays”. In: *Opt. Express* 20.15 (July 2012), pp. 16245–16257. DOI: 10.1364/OE.20.016245. URL: http://www.opticsexpress.org/abstract.cfm?URI=oe-20-15-16245.

[32] Yifeng Yang et al. “Passive coherent beam combining of four Yb-doped fiber amplifier chains with injection-locked seed source”. eng. In: *Optics letters* 38.6 (2013), pp. 854–856. ISSN: 0146-9592.

[33] Yu-Jen Wang et al. “Analysis of a 0.1 µm stepping bi-axis piezoelectric stage using a 2-DOF lumped model”. eng. In: *Microsystem technologies : sensors, actuators, systems integration* 26.2 (2020), pp. 425–436. ISSN: 0946-7076.

[34] Mingxiao Li et al. “Lithium niobate photonic-crystal electro-optic modulator”. eng. In: *Nature communications* 11.1 (2020), pp. 4123–4123. ISSN: 2041-1723.

[35] Linslal C. L. et al. "Implementation of stochastic parallel gradient descent algorithm for coherent beam combining". In: *High-Power Lasers and Applications IX*. Ed. by Ruxin Li and Upendra N. Singh. Vol. 10811. International Society for Optics and Photonics. SPIE, 2018, pp. 132 –137. DOI: 10.1117/12.2501014. URL: https://doi.org/10.1117/12.2501014.

[36] Marie Antier et al. "XCAN project : coherent beam combining of large number fibers in femtosecond regime (Conference Presentation)". eng. In: vol. 9992. SPIE, 2016, 99920B–99920B–1. ISBN: 9781510603882.

[37] Hongxiang Chang et al. "First experimental demonstration of coherent beam combining of more than 100 beams". In: *Photon. Res.* 8.12 (Dec. 2020), pp. 1943–1948. DOI: 10.1364/PRJ.409788. URL: http://www.osapublishing.org/prj/abstract.cfm?URI=prj-8-12-1943.

[38] R. Su et al. "Coherent Beam Combining of a Fiber Lasers Array Based on Cascaded Phase Control". In: *IEEE Photonics Technology Letters* 28.22 (2016), pp. 2585–2588. DOI: 10.1109/LPT.2016.2605765.

[39] Sassan Ahmadi. "Chapter 5 - New Radio Access RF and Transceiver Design Considerations". In: *5G NR*. Ed. by Sassan Ahmadi. Academic Press, 2019, pp. 655–745. ISBN: 978-0-08-102267-2. DOI: https://doi.org/10.1016/B978-0-08-102267-2.00005-1. URL: https://www.sciencedirect.com/science/article/pii/B9780081022672000051.

[40] R. Orta. *Lecture notes on electromagnetic field theory.*

[41] Keigo Iizuka. *Elements of photonics.* John Wiley, 2011.

[42] Dmitry S. Kulyabov et al. "Numerical analysis of eikonal equation". In: *Saratov Fall Meeting 2018: Laser Physics, Photonic Technologies, and Molecular Modeling*. Ed. by Vladimir L. Derbov. Vol. 11066. International Society for Optics and Photonics. SPIE, 2019, pp. 188 –195. DOI: 10.1117/12.2525142. URL: https://doi.org/10.1117/12.2525142.

[43] Hao Yu et al. "Application of Gaussian beam ray-equivalent model and back-propagation artificial neural network in laser diode fast axis collimator assembly". In: *Appl. Opt.* 55.23 (Aug. 2016), pp. 6530–6537. DOI: 10.1364/AO.55.006530. URL: http://ao.osa.org/abstract.cfm?URI=ao-55-23-6530.

[44] Robert Herloski, Sidney Marshall, and Ronald Antos. "Gaussian beam ray-equivalent modeling and optical design". In: *Appl. Opt.* 22.8 (Apr. 1983), pp. 1168–1174. DOI: 10.1364/AO.22.001168. URL: http://ao.osa.org/abstract.cfm?URI=ao-22-8-1168.

[45] Joseph Goodman. *Introduction to Fourier optics.* 2nd. 'McGraw-Hill', 1996, pp. 52–126.

[46] Alexander Talatinian and Mieczyslaw Pluta. "Propagation of a fundamental laser mode and its numerical simulation by the angular spectrum technique". In: *Optik* 127 (2016), pp. 3882–3887. DOI: `10.1016/j.ijleo.2016.01.111`.

[47] James W. Cooley and John W. Tukey. "Algorithm for the machine calculation of complex Fourier series". In: *Math. Comput.* 19 (1965), pp. 297–301.

[48] Leslie Greengard and June-Yub Lee. "Accelerating the nonuniform fast Fourier transform". In: *Society for Industrial and Applied Mathematics* 46 (2004), pp. 443–454. DOI: `10.1137/S003614450343200X`.

[49] Kyoji Matsushima and Tomoyoshi Shimobaba. "Band-limited angular spectrum method for numerical simulation of free-space propagation in far and near fields". In: *Optics Express* 17 (2009), pp. 19662–19673. DOI: `10.1364/OE.17.019662`.

[50] Lawrence R. Rabiner, Ronald W. Schafer, and Charles M. Rader. "Chirp Z-transform algorithm". In: *IEEE Transactions on Audio and Electroacoustics* 17 (1969), pp. 86 –92. DOI: `10.1109/TAU.1969.1162034`.

[51] Alessandro Mirigaldi, Maurizio Carbone, and Guido Perrone. "Non-uniform adaptive angular spectrum method and its application to neural network assisted coherent beam combining". In: *Opt. Express* 29.9 (Apr. 2021), pp. 13269–13287. DOI: `10.1364/OE.423057`. URL: `http://www.opticsexpress.org/abstract.cfm?URI=oe-29-9-13269`.

[52] Lawrence R. Rabiner, Ronald W. Schafer, and Charles M. Rader. "The Chirp z-transform algorithm and its application". In: *Bell System Technical Journal* 48 (1969), pp. 1249 –1292. DOI: `10.1002/j.1538-7305.1969.tb04268.x`.

[53] Xiao Yu et al. "Wide-window angular spectrum method for diffraction propagation in far and near field". In: *Optics Letters* 37 (2012), pp. 4943–4945. DOI: `10.1364/OL.37.004943`.

[54] Kyoji Matsushima, Hagen Schimmel, and Frank Wyrowski. "Fast calculation method for optical diffraction on tilted planes by use of the angular spectrum of plane waves". In: *Journal of the Optical Society of America A* 20 (2003), pp. 1755 –1762. DOI: `10.1364/JOSAA.20.001755`.

[55] Chenliang Chang et al. "Scaled diffraction calculation between tilted planes using nonuniform fast Fourier transform". In: *Optics Express* 22 (2014), pp. 17331 –17340. DOI: `10.1364/OE.22.017331`.

[56] Yong-Hae Kim et al. "Exact light propagation between rotated planes using non-uniform sampling and angular spectrum method". In: *Optics Communications* 344 (2015), pp. 1–6. DOI: `10.1016/j.optcom.2015.01.029`.

[57] Biao Cao et al. “Modified ray transfer matrix method for accurate non-sequential ray tracing between arbitrary reflective mirrors”. In: *Opt. Express* 28.12 (June 2020), pp. 17732–17740. DOI: `10.1364/OE.393045`. URL: `http://www.opticsexpress.org/abstract.cfm?URI=oe-28-12-17732`.

[58] R. Pashotta. *Numerical Aperture*. URL: `https://www.rp-photonics.com/numerical_aperture.html`.

[59] Seung-Hune Yang et al. “High-numerical-aperture image simulation using Babinet’s principle”. In: *J. Opt. Soc. Am. A* 27.5 (May 2010), pp. 1012–1023. DOI: `10.1364/JOSAA.27.001012`. URL: `http://josaa.osa.org/abstract.cfm?URI=josaa-27-5-1012`.

[60] B.R. Boruah and M.A.A. Neil. “Focal field computation of an arbitrarily polarized beam using fast Fourier transforms”. In: *Optics Communications* 282.24 (2009), pp. 4660–4667. ISSN: 0030-4018. DOI: `https://doi.org/10.1016/j.optcom.2009.09.019`. URL: `https://www.sciencedirect.com/science/article/pii/S0030401809008773`.

[61] URL: `https://www.altair.com/tracepro`.

[62] URL: `https://www.thorlabs.com/newgrouppage9.cfm?objectgroup_id=13685&pn=LA1540-AB`.

[63] R. Pashotta. *Principal Points and Principal Planes*. URL: `https://www.rp-photonics.com/principal_points_and_principal_planes.html`.

[64] Shawn Redmond et al. “Active coherent beam combining of diode lasers”. In: *Optics letters* 36 (Mar. 2011), pp. 999–1001. DOI: `10.1364/OL.36.000999`.

[65] Rongtao Su et al. “High Power Narrow-Linewidth Nanosecond All-Fiber Lasers and Their Actively Coherent Beam Combination”. In: *Selected Topics in Quantum Electronics, IEEE Journal of* 20 (Sept. 2014), pp. 1–13. DOI: `10.1109/JSTQE.2014.2312927`.

[66] Angel Flores et al. “Coherent Beam Combining of Fiber Amplifiers in a kW Regime”. In: *CLEO:2011 - Laser Applications to Photonic Applications.* Optical Society of America, 2011, CFE3. DOI: `10.1364/CLEO_SI.2011.CFE3`. URL: `http://www.osapublishing.org/abstract.cfm?URI=CLEO_SI-2011-CFE3`.

[67] Jie Li et al. “All-fiber active coherent combining via a fiber combiner”. In: *Optics Communications* 286 (Jan. 2013), 273–276. DOI: `10.1016/j.optcom.2012.08.074`.

[68] Hongxiang Chang et al. “First experimental demonstration of coherent beam combining of more than 100 beams”. In: *Photon. Res.* 8.12 (Dec. 2020), pp. 1943–1948. DOI: `10.1364/PRJ.409788`. URL: `http://www.osapublishing.org/prj/abstract.cfm?URI=prj-8-12-1943`.

[69] Xin-She Yang. "3 - Optimization algorithms". In: *Introduction to Algorithms for Data Mining and Machine Learning*. Ed. by Xin-She Yang. Academic Press, 2019, pp. 45–65. ISBN: 978-0-12-817216-2. DOI: https://doi.org/10.1016/B978-0-12-817216-2.00010-7. URL: https://www.sciencedirect.com/science/article/pii/B9780128172162000107.

[70] Huizhen Yang and Xinyang Li. "Theoretical Analysis of Stochastic Parallel Gradient Descent Control Algorithm in Adaptive Optics". In: *2009 WRI Global Congress on Intelligent Systems*. Vol. 2. 2009, pp. 338–342. DOI: 10.1109/GCIS.2009.383.

[71] Sebastian Ruder. *An overview of gradient descent optimization algorithms*. 2017. arXiv: 1609.04747 [cs.LG].

[72] Qintao Hu et al. "Adaptive stochastic parallel gradient descent approach for efficient fiber coupling". In: *Opt. Express* 28.9 (Apr. 2020), pp. 13141–13154. DOI: 10.1364/OE.390762. URL: http://www.opticsexpress.org/abstract.cfm?URI=oe-28-9-13141.

[73] Jorge Garza-Ulloa. "Chapter 5 - Methods to develop mathematical models: traditional statistical analysis". In: *Applied Biomechatronics using Mathematical Models*. Ed. by Jorge Garza-Ulloa. Academic Press, 2018, pp. 239–371. ISBN: 978-0-12-812594-6. DOI: https://doi.org/10.1016/B978-0-12-812594-6.00005-6. URL: https://www.sciencedirect.com/science/article/pii/B9780128125946000056.

[74] Hao Yu et al. "Artificial neural network assisted laser chip collimator assembly and impact on multi-emitter module beam parameter product". In: *Proc. SPIE*. Vol. 10085. 2017, p. 1008508. DOI: 10.1117/12.2254031.

[75] M.R.G. Meireles, P.E.M. Almeida, and M.G. Simoes. "A comprehensive review for industrial applicability of artificial neural networks". In: *IEEE Transactions on Industrial Electronics* 50 (2003), pp. 585 –601. DOI: 10.1109/TIE.2003.812470.

[76] Liesle Caballero, Mario Jojoa, and Winston S. Percybrooks. "Optimized neural networks in industrial data analysis". In: *SN Appl. Sci.* 2 (2020), p. 300. DOI: 10.1007/s42452-020-2060-5.

[77] Věra Kůrková. "Kolmogorov's theorem and multilayer neural networks". In: *Neural Networks* 5 (1992), pp. 501 –506. DOI: 10.1016/0893-6080(92)90012-8.

[78] A. D. Rasamoelina, F. Adjailia, and P. Sinčák. "A Review of Activation Function for Artificial Neural Network". In: *2020 IEEE 18th World Symposium on Applied Machine Intelligence and Informatics (SAMI)*. 2020, pp. 281–286. DOI: 10.1109/SAMI48414.2020.9108717.

[79] Guifang Lin and Wei Shen. "Research on convolutional neural network based on improved Relu piecewise activation function". eng. In: *Procedia computer science* 131 (2018), pp. 977–984. ISSN: 1877-0509.

[80] Y. Tu et al. "A Power Efficient Neural Network Implementation on Heterogeneous FPGA and GPU Devices". In: *2019 IEEE 20th International Conference on Information Reuse and Integration for Data Science (IRI)*. 2019, pp. 193–199. DOI: `10.1109/IRI.2019.00040`.

[81] T. Tekin. "Review of packaging of optoelectronic, photonic, and MEMS components". In: *IEEE J. Sel. Topics in Quantum Electron.* 17 (2011), pp. 704–719.

[82] A.G. Grobnic. "Challenges in the optical alignment of optoelectronic components". In: *Proc. SPIE*. Vol. 10313. 2017.

[83] Hao Yu et al. "Investigation of collimating and focusing lenses' impact on laser diode stack beam parameter product". In: *Applied Optics* 54 (2015), pp. 10240 –10248. DOI: `10.1364/AO.54.010240`.

[84] Hao Yu et al. "Application of Gaussian beam ray-equivalent model and back-propagation artificial neural network in laser diode fast axis collimator assembly". In: *Applied Optics* 55 (2016), pp. 6530 –6537. DOI: `10.1364/AO.55.006530`.

[85] Hao Yu et al. "Gaussian beam optics model for multi-emitter laser diode module configuration design". In: *Advances in Neural Networks*. Ed. by Simone Bassis et al. Vol. 54. Smart Innovation, Systems and Technologies. Springer, Cham, 2016, pp. 457–464. DOI: `10.1007/978-3-319-33747-0_45`.

[86] L. Coldren and S. Corzine. "Diode Lasers and Photonic Integrated Circuits". In: 1995.

[87] Akira Mugino. "Recent progress of fiber Bragg-grating stabilized laser diode modules for EDFA pumping". In: *Reliability of Optical Fibers and Optical Fiber Systems: A Critical Review*. Ed. by Dilip K. Paul. Vol. 10295. International Society for Optics and Photonics. SPIE, 1999, pp. 184 –211. URL: `https://doi.org/10.1117/12.361083`.

[88] G. Venus et al. "Spectral stabilization of laser diodes by external Bragg resonator". In: 2004.

[89] B. L. Volodin et al. "Wavelength stabilization and spectrum narrowing of high-power multimode laser diodes and arrays by use of volume Bragg gratings". In: *Opt. Lett.* 29.16 (Aug. 2004), pp. 1891–1893. DOI: `10.1364/OL.29.001891`. URL: `http://ol.osa.org/abstract.cfm?URI=ol-29-16-1891`.

[90] Christophe Moser, Lawrence Ho, and Frank Havermeyer. "Self-aligned non-dispersive external cavity tunable laser". In: *Opt. Express* 16.21 (Oct. 2008), pp. 16691–16696. DOI: 10.1364/OE.16.016691. URL: http://www.opticsexpress.org/abstract.cfm?URI=oe-16-21-16691.

[91] Peter Blood et al. "Modelling Quantum Well Laser Diode Structures". In: *Advanced Electronic Technologies and Systems Based on Low-Dimensional Quantum Devices*. Ed. by Minko Balkanski and Nikolai Andreev. Dordrecht: Springer Netherlands, 1997, pp. 77–98. ISBN: 978-94-015-8965-9. DOI: 10.1007/978-94-015-8965-9_2. URL: https://doi.org/10.1007/978-94-015-8965-9_2.

[92] Govind B. Nair and S.J. Dhoble. "The Fundamentals and Applications of Light-Emitting Diodes". In: *The Fundamentals and Applications of Light-Emitting Diodes*. Ed. by Govind B. Nair and S.J. Dhoble. Woodhead Publishing Series in Electronic and Optical Materials. Woodhead Publishing, 2021. ISBN: 978-0-12-819605-2. DOI: https://doi.org/10.1016/B978-0-12-819605-2.00002-1. URL: https://www.sciencedirect.com/science/article/pii/B9780128196052000021.

[93] Shankar Kumar Selvaraja and Purnima Sethi. "Review on Optical Waveguides". In: Aug. 2018. ISBN: 978-1-78923-492-3. DOI: 10.5772/intechopen.77150.

[94] Alberto Main. "Study of optical filamentation in high power laser diodes". PhD thesis. University degli studi di Torino, 2017.

[95] Maina Alberto and Claudio Coriasso. "Near field analysis of broad-area high-power laser diode using nonlinear bidirectional beam propagation method". In: *European Semiconductor Laser Workshop*. 2018, pp. 31 –32.

[96] J. R. Marciante and G. P. Agrawal. "Nonlinear mechanisms of filamentation in broad-area semiconductor lasers". In: *IEEE Journal of Quantum Electronics* 32.4 (1996), pp. 590–596. DOI: 10.1109/3.488831.

[97] Domenico Campi and Claudio Coriasso. "Optical nonlinearities in multiple quantum wells: Generalized Elliott formula". In: *Phys. Rev. B* 51 (16 Apr. 1995), pp. 10719–10728. DOI: 10.1103/PhysRevB.51.10719. URL: https://link.aps.org/doi/10.1103/PhysRevB.51.10719.

[98] Mark Stephen, Molly Fahey, and Ian Miller. "Solid, 3-mirror Fabry–Perot etalon". In: *Appl. Opt.* 56.10 (Apr. 2017), pp. 2636–2640. DOI: 10.1364/AO.56.002636. URL: http://ao.osa.org/abstract.cfm?URI=ao-56-10-2636.

[99] Sake J. Hogeveen and Herman van de Stadt. “Fabry-Perot interferometers with three mirrors”. In: *Appl. Opt.* 25.22 (1986), pp. 4181–4184. DOI: 10.1364/AO.25.004181. URL: http://opg.optica.org/ao/abstract.cfm?URI=ao-25-22-4181.

[100] R. Orta. *Lecture notes on passive optical components.*

[101] D. Marcuse. “Coupled Mode Theory of Round Optical Fibers”. In: *Bell System Technical Journal* 52.6 (1973), pp. 817–842. DOI: https://doi.org/10.1002/j.1538-7305.1973.tb01992.x. eprint: https://onlinelibrary.wiley.com/doi/pdf/10.1002/j.1538-7305.1973.tb01992.x. URL: https://onlinelibrary.wiley.com/doi/abs/10.1002/j.1538-7305.1973.tb01992.x.

[102] Raman Kashyap. “Chapter 4 - Theory of Fiber Bragg Gratings”. In: *Fiber Bragg Gratings (Second Edition)*. Ed. by Raman Kashyap. Second Edition. Boston: Academic Press, 2010, pp. 119–187. ISBN: 978-0-12-372579-0. DOI: https://doi.org/10.1016/B978-0-12-372579-0.00004-1. URL: https://www.sciencedirect.com/science/article/pii/B9780123725790000041.

[103] Markus J. Schmid and Mathias S. Müller. “Measuring Bragg gratings in multimode optical fibers”. In: *Opt. Express* 23.6 (Mar. 2015), pp. 8087–8094. DOI: 10.1364/OE.23.008087. URL: http://www.opticsexpress.org/abstract.cfm?URI=oe-23-6-8087.

[104] N. Sun et al. “Numerical Analysis of Apodized Fiber Bragg Gratings Using Coupled Mode Theory”. In: *Progress in Electromagnetics Research-pier* 99 (2009), pp. 289–306.

[105] Alessandra Beccaria et al. “Temperature monitoring of tumor hyperthermal treatments with optical fibers: comparison of distributed and quasi-distributed techniques”. In: *Optical Fiber Technology* 60 (2020), p. 102340. ISSN: 1068-5200. DOI: https://doi.org/10.1016/j.yofte.2020.102340. URL: https://www.sciencedirect.com/science/article/pii/S1068520020303308.

[106] Graham D. Marshall et al. “Point-by-point written fiber-Bragg gratings and their application in complex grating designs”. In: *Opt. Express* 18.19 (Sept. 2010), pp. 19844–19859. DOI: 10.1364/OE.18.019844. URL: http://www.opticsexpress.org/abstract.cfm?URI=oe-18-19-19844.

[107] Raman Kashyap. “The Fiber Fuse - from a curious effect to a critical issue: A 25th year retrospective”. In: *Opt. Express* 21.5 (2013), pp. 6422–6441. DOI: 10.1364/OE.21.006422. URL: http://opg.optica.org/oe/abstract.cfm?URI=oe-21-5-6422.

[108] A. Fuerbach et al. “Line-by-line Femtosecond FBG Inscription for Innovative Fiber Lasers”. In: *Advanced Photonics 2018 (BGPP, IPR, NP, NOMA, Sensors, Networks, SPPCom, SOF)*. Optical Society of America, 2018, BW3A.6. DOI: 10.1364/BGPPM.2018.BW3A.6. URL: http://www.osapublishing.org/abstract.cfm?URI=BGPPM-2018-BW3A.6.

[109] Jean-Philippe Bérubé, Martin Bernier, and Réal Vallée. “Femtosecond laser-induced refractive index modifications in fluoride glass”. In: *Optics material express* 3 (May 2013), p. 598. DOI: 10.1364/OME.3.000598.

[110] M. Bukharin, D. Khudakov, and S. Vartapetov. “Investigation of Refractive Index Profile Induced with Femtosecond Pulses into Neodymium Doped Phosphate Glass for the Purposes of Hybrid Waveguiding Structures Formation”. In: *Physics Procedia* 71 (2015). 18th Conference on Plasma-Surface Interactions, PSI 2015, 5-6 February 2015, Moscow, Russian Federation and the 1st Conference on Plasma and Laser Research and Technologies, PLRT 2015, 18-20 February 2015, Moscow, Russian Federation", pp. 272–276. ISSN: 1875-3892. DOI: https://doi.org/10.1016/j.phpro.2015.08.300. URL: https://www.sciencedirect.com/science/article/pii/S1875389215010664.

[111] Roberto Paoletti et al. “350 W high-brightness multi-emitter semiconductor laser module emitting at 976 nm”. In: Mar. 2021, p. 2. DOI: 10.1117/12.2583277.

[112] Valentina Serafini et al. “Compact high-brightness and highly manufacturable blue laser modules”. In: Mar. 2021, p. 16. DOI: 10.1117/12.2583229.

[113] URL: https://www.rp-photonics.com/dichroic_mirrors.html.

[114] Palmer Leidner Jordan. “Spatial and Spectral Brightness Enhancement of High Power Semiconductor Lasers”. PhD thesis. University of Rochester, 2015.

[115] Wouter J Westerveld and H Paul Urbach. “Waveguides”. In: *Silicon Photonics*. 2053-2563. IOP Publishing, 2017, 2–1 to 2–36. ISBN: 978-0-7503-1386-5. DOI: 10.1088/978-0-7503-1386-5ch2. URL: http://dx.doi.org/10.1088/978-0-7503-1386-5ch2.

[116] Dominik Scholz et al. “Measurement and simulation of filamentation in (Al,In)GaN laser diodes”. In: *Opt. Express* 16.10 (2008), pp. 6846–6859. DOI: 10.1364/OE.16.006846. URL: http://opg.optica.org/oe/abstract.cfm?URI=oe-16-10-6846.

[117] Sebastian Luhn and Martina Hentschel. “Analytical Fresnel laws for curved dielectric interfaces”. In: *Journal of Optics* 22.1 (Dec. 2019), p. 015605. DOI: 10.1088/2040-8986/ab5c42. URL: https://doi.org/10.1088/2040-8986/ab5c42.

[118] Maryam Ilchi-Ghazaani and Parviz Parvin. “Gain Saturation in Optical Fiber Laser Amplifiers”. In: Mar. 2016, pp. 297–320. ISBN: 978-953-51-4615-5. DOI: 10.5772/62136.

[119] Nathan Butt, Rory Roberts, and Soumya Patnaik. “Laser diode optical output dependence on junction temperature for high-power laser systems”. In: *Optics & Laser Technology* 125 (Dec. 2019), p. 106019. DOI: 10.1016/j.optlastec.2019.106019.

[120] Roberto Paoletti et al. “Wavelength-stabilized DBR high-power diode laser”. In: *Journal of Physics: Photonics* 2 (Jan. 2020). DOI: 10.1088/2515-7647/ab6712.

[121] Roberto Paoletti et al. “350 W high-brightness multi-emitter semiconductor laser module emitting at 976 nm”. In: Mar. 2021, p. 2. DOI: 10.1117/12.2583277.